A Determination of the Effective Weak Mixing Angle from the $Z \rightarrow b\bar{b}$ Forward-Backward Asymmetry

Douglas Mitchell Wright

A DISSERTATION
PRESENTED TO THE FACULTY
OF PRINCETON UNIVERSITY
IN CANDIDACY FOR THE DEGREE OF
DOCTOR OF PHILOSOPHY

RECOMMENDED FOR ACCEPTANCE
BY THE DEPARTMENT OF PHYSICS

November 1993

Abstract

This thesis describes a measurement of the effective weak mixing angle, $\sin^2\bar{\theta}_W$, determined from the forward-backward asymmetry in Z→b$\bar{\text{b}}$ events collected by the L3 experiment at LEP during 1990 and 1991. The data sample corresponds to approximately 410,000 hadronic decays of the Z.

The b quarks were identified by their semileptonic decay to electrons or muons. The transverse momentum of the lepton with respect to the axis of the nearest jet, p_T, was used to distinguish between leptons from b decay and those from background.

Due to the mixing of neutral B mesons, the observed asymmetry is reduced by a factor (1-2$\mathcal{X}$), where $\mathcal{X}$ is the B^0-$\bar{\text{B}}^0$ mixing parameter. A determination of $\mathcal{X}$ from the data sample in which both b quarks in the event were tagged by a lepton is also presented. A fit to the dilepton p_T spectra resulted in $\mathcal{X} = 0.125 \pm 0.021(\text{stat}) \pm 0.012(\text{syst})$.

From a fit to the single lepton p_T spectrum the b$\bar{\text{b}}$ forward-backward asymmetry was determined to be $A_{b\bar{b}} = 0.085 \pm 0.017(\text{stat}) \pm 0.004(\text{syst})$, corrected for B^0-$\bar{\text{B}}^0$ mixing. This value corresponds to a mixing angle $\sin^2\bar{\theta}_W = 0.2336 \pm 0.0032$, which is in excellent agreement with independent measurements of the mixing angle measured from other L3 data.

to Virginia, Julianne, Madeleine and Donald

Acknowledgments

This thesis would never have been completed without the assistance and guidance of many people. First, I would like to thank my advisors Pierre Piroué and David Stickland. From them I learned not only about physics but also how to remain focused, to keep my eye on the big picture and to get things done. I would also like to thank Howard Stone for many useful discussions and most importantly for frequently bringing his friend Sam to lunch.

Much of the work for this thesis was carried out at CERN and I am indebted to my colleagues who worked closely with me there. In particular I want to thank Bob Clare, Patricia McBride, and Tim McMahon. Special thanks are in order for Hans Lubbers, who kept the computers going and fixed countless problems for me.

In my opinion, the greatest resource of the physics department is its graduate student population. My association with the OUTLAWS: Gregg Berman, Dave Clarke, Mark Doyle, Andrew Felce, Erik Jacobsen, and Brek Miller, helped to sustain me through my graduate school career and I am grateful to have known such a diverse and talented group of people. I must also express my gratitude to my next door neighbors and friends, Mehran Ardebili, Mark Convery, and Rob McPherson, for listening to unsolicited expositions of my work and for their thoughtful suggestions. Thanks also are due Josh Klein and Mark Palmer for commiserating with me on our collective thesis writing predicament.

I cannot overestimate the contribution made by my family. My parents, Donald and Virginia Wright, instilled in me a curiosity about the world, a love of truth, and an appreciation for beauty. They also taught me that "nothing worth doing is easy." The completion of this thesis is a testimony to their love and support. My wife Julianne, who has been with me since my third day at Princeton, unselfishly sacrificed her time and energy to allow me to pursue this work. She has helped me directly in innumerable ways and her emotional support throughout was essential for reaching a successful conclusion. This thesis is as much a product of her heart as of my mind. Finally, I want to thank my daughter, Madeleine, for understanding that her daddy had to go to "work" so often in the middle of the night and on weekends.

Contents

List of Figures

List of Tables

Chapter 1

Introduction

In the last twenty years the Standard Model of strong and electroweak interactions has been extremely successful in describing the physics of elementary particles. Nearly all of the fundamental parameters have been precisely measured and calculations with the theory agree well with all current experimental results. However, many aspects of the model are essentially arbitrary; e.g. the number of generations, the fermion masses, the quark mixing matrix. Furthermore, an important part of the theory, the Higgs mechanism for generating boson and fermion masses, has not been experimentally established. In some sense the Standard Model is merely a phenomenological description that falls short of giving a fundamental understanding of nature. Is there a more fundamental theory? Experimental physics can take two approaches to answering this question: precision tests to search for inconsistencies in the model and direct searches for phenomena not accommodated by the theory. The Large Electron Positron collider (LEP) at CERN was constructed to explore both approaches.

This thesis describes a precision test of the Standard Model using the L3 detector at LEP to measure the forward-backward asymmetry in the decay of the Z boson to a pair of bottom (b) quarks. From the b quark asymmetry the effective weak mixing angle $\sin^2\bar{\theta}_W$, which is related to the fundamental parameter $\sin^2\theta_W$ of the Standard Model, can be determined. A determination of $\sin^2\bar{\theta}_W$ that differs from other measurements extracted from LEP data could be a hint of physics beyond the Standard Model.

History of the Z boson

The theory of weak interactions developed by Glashow, Salam and Weinberg (GSW) in the 1960's predicted the existence of a heavy, neutral intermediate vector boson, the Z [1–4]. The first experimental evidence for the Z came from the discovery of weak neutral current interactions by the Gargamelle Collaboration at CERN in 1973 [5]. Using a heavy-liquid bubble chamber, they observed electrons scattered by an antineutrino beam. From 1.4 million photographs, 3 neutral current events were identified.

This discovery led to an intensified effort to directly observe decays of the Z boson. First to report such an observation were the UA1 and UA2 collaborations in 1983 [6,7]. From $p\bar{p}$ collisions at a center-of-mass energy of 540 GeV they were able to identify 20 Z decay events.

To study the Z boson in more detail, two e^+e^- colliders were built: the Stanford Linear Collider (SLC) [8] and LEP [9]. Both colliders are able to produce a large number of Z's by taking advantage of the resonant enhancement of the production cross-section at center-of-mass energies near the Z mass. LEP began operation in 1989 and by the end of 1991 has produced nearly 2 million Z decays. Since the branching ratio for the Z to decay into a pair of b quarks is ~ 15%, these colliders also provide a large sample of b hadrons.

History of b physics

The bound state of b quarks ($b\bar{b}$) was discovered in proton-neutron interactions at Fermilab in 1977 and dubbed the Υ [10–12]. Since the bound state decays strongly it provides no information on the weak decay of b quarks (the b and $\bar{b}$ annihilate before either quark can decay weakly). Three radially excited $b\bar{b}$ S states were initially observed: $\Upsilon(1S)$, $\Upsilon(2S)$, and $\Upsilon(3S)$ which appeared as narrow peaks in the hadronic cross-section as a function of center-of-mass energy. The CLEO and CUSB collaborations at the Cornell Electron Storage Ring (CESR) then discovered a broad peak at 10.578 GeV which was identified as the $\Upsilon(4S)$ [13, 14]. The broadness of the peak and the appearance of high-momentum leptons in its decay indicated that the $\Upsilon(4S)$ was not a bound state [15]. The only energetically allowed decays for this state into a pair of B mesons are $\Upsilon(4S)\rightarrow B^+B^-$, and $\Upsilon(4S)\rightarrow B^0\bar{B}^0$. Studies of these decays at CESR and DORIS provide most of the pre-LEP knowledge of B mesons.

The production and study of b hadrons in the continuum well above the $\Upsilon(4S)$ at around 30 GeV has been conducted by several experiments at PEP [16–19] and PETRA [20–22]. At these energies the b quarks give rise to narrow jets of hadrons.

The b quark jets are distinguished from those of lighter quarks by identifying leptons from the weak decay of the b. The same techniques are used to study b decays at LEP.

The Weak Mixing Angle: $\sin^2\bar{\theta}_W$

In the Standard Model, the neutral component of the purely weak field that couples left-handed fermions mixes with the hypercharge field to produce a massless (photon) and massive (Z) vector boson. The amount of mixing of the 'pure' fields is set by the free parameter $\sin^2\theta_W$.

Currently, the best measurement of $\sin^2\theta_W$ comes from deep-inelastic neutrino-nucleon scattering. Measurements of the ratio of the neutral current to charged current cross-section

$$R \equiv \frac{\sigma(\nu_\mu N \rightarrow \nu_\mu X)}{\sigma(\nu_\mu N \rightarrow \mu^- X)},$$

result in $\sin^2\theta_W = 0.2283 \pm 0.0026(\text{stat}) \pm 0.0045(\text{syst})$[1] [23].

Interference effects between electromagnetic and weak neutral currents can also be exploited to extract $\sin^2\theta_W$ from a variety of experiments. Measurements from atomic parity violation transitions [24], polarized eD [25] and μN scattering [26] are in good agreement with the neutrino results.

The determination of $\sin^2\theta_W$ from LEP data is complicated by theoretical uncertainties stemming from the contributions of the as yet unobserved and presumed

---

[1] The first and second listed errors are respectively the statistical and systematic uncertainties, unless otherwise noted.

heavy particles: the top quark and the Higgs boson. Calculations of differential and total cross-sections at LEP energies require the inclusion of higher order corrections that are significantly affected by couplings to heavy particles. However, much of the dependence on the top and Higgs masses (m_t and m_H respectively) from these corrections can be included in the result from the lowest order calculation by replacing $\sin^2\theta_W$ with an effective weak mixing angle $\sin^2\bar{\theta}_W = \sin^2\bar{\theta}_W(m_t, m_H)$. Comparisons of $\sin^2\bar{\theta}_W$ determined from different experimental observables at LEP provide a test of the Standard Model since the effects of the higher order corrections that depend on m_t and m_H are absorbed into the definition of $\sin^2\bar{\theta}_W$. Also, this dependence can be exploited to make a prediction of the top quark mass within the framework of the Standard Model.

The following chapter discusses the Standard Model in more detail, and describes the aspects of b physics that are used to extract b quark events from the hadronic decays of the Z. The LEP collider and the L3 detector are described in Chapter 3. Chapter 4 presents the cuts used to select the data sample, and the measurement of the b quark asymmetry is treated in Chapter 5. The final chapter describes the determination of $\sin^2\bar{\theta}_W$ from the $b\bar{b}$ asymmetry and compares the result with other L3 data and data from lower energy e^+e^- colliders.

Chapter 2

Theoretical Motivation

2.1 The Standard Model

The Standard Model of particle physics consists of two quantum field theories, the electroweak theory of Glashow, Salam and Weinberg (GSW), which unifies the weak and electromagnetic interactions, and Quantum Chromodynamics (QCD) [27], which explains the strong interaction. Both theories are constructed from a set of fermions that constitute the building blocks of matter and a set of bosons that mediate the interactions between them. These elementary particles and some of their properties are listed in Table 2.1. The fermions can be divided into quarks and leptons based on their participation in the strong interaction. The different varieties of quarks and leptons are often referred to as "flavors."

Only quarks experience the strong interaction, which is mediated by the exchange of gluons. In QCD, the strong force is described in terms of a conserved "color"

Table 2.1: Elementary particles and some of their properties. Particles denoted by an asterisk have not yet been directly observed. The unit of charge is defined such that the electron has charge -1.

Particle	Symbol	Spin ($\hbar$)	Charge	Mass (GeV)
QUARKS				
up	u	1/2	2/3	0.005-0.015
down	d	1/2	−1/3	0.002-0.008
charm	c	1/2	2/3	1.3-1.7
strange	s	1/2	−1/3	0.1-0.3
top*	t	1/2	2/3	140?
bottom	b	1/2	−1/3	4.7-5.3
LEPTONS				
electron neutrino	ν_e	1/2	0	$< 3 \times 10^{-8}$
electron	e	1/2	-1	0.511×10^{-3}
muon neutrino	ν_μ	1/2	0	$< 0.25 \times 10^{-3}$
muon	μ	1/2	-1	0.106
tau neutrino*	ν_τ	1/2	0	< 0.07
tau	τ	1/2	-1	1.78
GAUGE BOSONS				
photon	γ	1	0	0
W boson	$W^\pm$	1	±1	80.22 ± 0.26
Z boson	Z	1	0	91.195 ± 0.009
Higgs Scalar*	H	0	0	?
Gluon	g	1	0	0

charge where each quark flavor can take on one of three color values. There is only one free parameter in the theory, α_s, which determines the strength of the quark-gluon couplings and gluon self interactions.

All fermions participate in the weak interaction, which is mediated by W and Z bosons. The W bosons induce transitions between fermion flavors in which one unit of charge is exchanged. In terms of this interaction the fermions can be grouped into doublets

$$\begin{pmatrix} u \\ d \end{pmatrix}_L \begin{pmatrix} c \\ s \end{pmatrix}_L \begin{pmatrix} t \\ b \end{pmatrix}_L \begin{pmatrix} \nu_e \\ e \end{pmatrix}_L \begin{pmatrix} \nu_\mu \\ \mu \end{pmatrix}_L \begin{pmatrix} \nu_\tau \\ \tau \end{pmatrix}_L,$$

where the W transforms one member of the doublet into the other. The subscript L indicates that only left-handed particles (where the spin of the particle is anti-aligned with its momentum) couple to the W. The right-handed particles are assigned to singlet states that do not couple to the W. This chirality or handedness of the weak interaction was observed in the 1950's in parity violating decays of what is now known as the K^+ meson and in beta decay of polarized nuclei. These observations led to the V-A theory of weak decays introduced independently by Feynman and Gell-Mann, and Sudarshan and Marshak, which was eventually supplanted by the GSW theory involving intermediate vector bosons.

The doublet-singlet grouping of fermions with respect to the weak interaction can be represented in terms of weak "isospin" quantum numbers, which are listed in Table 2.2. The left-handed fermions are assigned total weak isospin $I = \frac{1}{2}$, where upper and lower members of the doublet are distinguished by the third component of

Table 2.2: Total weak isospin, I, and third component of the isospin, I^3, quantum numbers for quarks and leptons.

fermions	I	I^3	fermions	I	I^3
u_L, c_L, t_L	$\frac{1}{2}$	$\frac{1}{2}$	u_R, c_R, t_R	0	0
d_L, s_L, b_L	$\frac{1}{2}$	$-\frac{1}{2}$	d_R, s_R, b_R	0	0
ν_{eL}, $\nu_{\mu L}$, $\nu_{\tau L}$	$\frac{1}{2}$	$\frac{1}{2}$	ν_{eR}, $\nu_{\mu R}$, $\nu_{\tau R}$	-	-
e_L, μ_L, τ_L	$\frac{1}{2}$	$-\frac{1}{2}$	e_R, μ_R, τ_L	0	0

weak isospin I^3. Right-handed fermions are assigned a weak isospin of zero.

The experimental observation of weak decays in hadrons indicates that the mass eigenstates of the quarks are a mixture of the eigenstates of the weak interaction. This permits any charge-changing transition among the left-handed quarks

$$(\mathrm{u\ or\ c\ or\ t})_L \leftrightarrow (\mathrm{d\ or\ s\ or\ b})_L.$$

Whether this is true for the lepton doublets has not been established. If the neutrino is massless then any mixture of weak eigenstates is still an eigenstate of mass, and lepton mixing is therefore unobservable.

The Z boson and the photon transform singlets and the upper and lower members of doublets into themselves, thus preserving quark and lepton flavors. However, the photon only couples to charged fermions.

The different couplings of the neutral bosons to the fermions pose a potential problem. Triangle diagrams as in Fig. 2.1 in which a fermion circulates in a loop that couples to three (nonidentical) neutral bosons are divergent for any particular

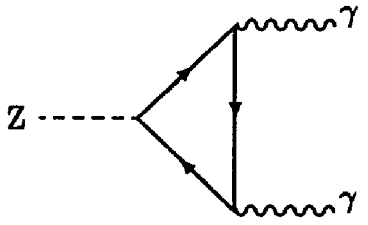

FIG. 2.1: Example of a divergent triangle diagram.

fermion. However, if the sum of these diagrams over all fermion contributions exactly cancels then the theory remains finite. Arranging the fermions into generations or families in which the sum of the charges is zero, i.e. (u, d, ν_e, e), (c, s, ν_μ, μ), and (t, b, ν_τ, τ) results in the desired cancellation for each generation. Three quark colors and the existence of the top quark are required for cancellation to occur.

Neutral Currents

One of the great triumphs of the GSW model of electroweak interactions was its prediction of weak neutral currents. In an attempt to form a compact theory to explain flavor changing weak interactions, an isospin triplet of fields ${W_\mu}^1$, ${W_\mu}^2$, ${W_\mu}^3$ was introduced that couples left-handed fermions with coupling strength g. Two components of the field could be combined to form bosons that mediate the isospin step up/down interactions:

$${W_\mu}^\pm = \frac{1}{\sqrt{2}}\left({W_\mu}^1 \mp i{W_\mu}^2\right).$$

The third component was needed to form a symmetry group so that a renormalizable quantum field theory could be constructed. This left-over component represented a neutral coupling of left-handed fermions. The electromagnetic interaction was included in this formalism by introducing an additional isospin singlet field B_μ whose conserved quantum number is called hypercharge with coupling strength g'. This singlet field, which couples to both left- and right-handed fermions, mixes with the neutral component of the weak field

$$\begin{aligned} A_\mu &= B_\mu \cos\theta_W + {W_\mu}^3 \sin\theta_W \\ Z_\mu &= -B_\mu \sin\theta_W + {W_\mu}^3 \cos\theta_W . \end{aligned}$$

The amount of mixing is set by the free parameter θ_{W} and the resultant fields A_μ and Z_μ are identified with the photon and the Z boson. This fixes the relationship between the weak couplings g and g' in terms of the charge of the electron e and the weak mixing angle θ_W: $e = g \sin\theta_W = g' \cos\theta_W$.

Experiments indicate that the weak interaction is short ranged and thus the bosons that mediate it must be massive. However, the vector bosons introduced in the GSW formalism are by necessity massless. Explicitly introducing a mass term would violate the symmetries exploited in the construction of the theory. The solution is to invoke "spontaneous symmetry breaking" via the Higgs mechanism to provide masses for the W and Z bosons while leaving the photon massless and preserving the renormalizability of the theory.

The Higgs Mechanism

In the Standard Model spontaneous symmetry breaking is achieved by introducing a weak-isospin doublet of complex scalar fields ϕ (the Higgs field)

$$\phi = \sqrt{\tfrac{1}{2}} \begin{pmatrix} \phi_1 + i\phi_2 \\ \phi_3 + i\phi_4 \end{pmatrix}.$$

The self interactions of this field give rise to a scalar potential which is defined to be

$$V = \mu^2 \phi^\dagger \phi + \lambda(\phi^\dagger \phi)^2,$$

where the parameters μ and λ are arbitrary. The Lagrangian of the electroweak interaction is modified by adding contributions from the Higgs field, where the extra pieces have been carefully constructed to preserve the gauge symmetry of the Lagrangian.

In the case were $\mu^2 < 0$ and $\lambda > 0$ the potential V has a set of minima at nonzero values of $|\phi|$. Choosing one of these minima $\phi_1 = \phi_2 = \phi_4 = 0, \quad \phi_3 = -\mu^2/\lambda = v^2$ as the vacuum expectation value

$$\phi_0 \equiv \tfrac{1}{2} \begin{pmatrix} 0 \\ v \end{pmatrix},$$

and expanding the Higgs field about this point, the Lagrangian takes on a very suggestive form. Pieces of the expanded Lagrangian can be identified as describing a new neutral scalar boson (the Higgs) and as mass terms for the W and Z bosons.

The masses are

$$m_W = \tfrac{1}{2}vg$$

$$m_Z = \tfrac{1}{2}v\sqrt{g^2 + g'^2}$$

$$m_H = \sqrt{2v^2\lambda}.$$

The vector boson masses are related by

$$\frac{m_W}{m_Z} = \cos\theta_W.$$

Interactions between the fermions and the Higgs field also generate mass terms for the fermions; however, the coupling strength of this interaction is not fixed. While the Higgs mechanism generates masses for the fermions it does not predict what they are.

The physical interpretation of the Higgs mechanism is that the vacuum can emit or absorb a neutral, colorless quantum of the Higgs field that interacts with fermions and gauge bosons to give them masses. Photons and gluons do not interact with this quantum and thus remain massless.

Electroweak Parameters

The three free parameters g, g', v in conjunction with the quark mass mixing matrix completely define the electroweak interaction in the GSW theory. The first three parameters can be replaced by three related and more precisely measured quantities: the fine structure constant α, the fermi constant G_F, and the weak mixing angle $\sin^2\theta_W$.

The fine structure constant is related to the electroweak couplings through the electron charge ($4\pi\alpha = e^2$, $e = g\sin\theta_W$) and has been calculated from measurements of the electron magnetic moment [28]. The value is known with an uncertainty of less than 50 parts per billion and is $\alpha = 1/137.0359895(61)$, where the value in parenthesis is the uncertainty in the last digits.

The only allowed decay channel for a muon is the purely weak decay $\mu^- \rightarrow \nu_\mu e^- \nu_e$. The muon lifetime is calculable in terms of an effective coupling constant G_F

$$\frac{1}{\tau} = (1+\delta)\frac{{G_F}^2 m_\mu^5}{192\pi^3},$$

where δ is a small electromagnetic radiative correction. Precise measurements of the muon lifetime [29] lead to $G_F = 1.16639(2) \times 10^{-5}$ GeV^{-2}.

Using only the lowest order diagrams in the Standard Model, which are often referred to as "tree level" diagrams, the fermi constant is related to the fundamental weak parameters by

$$G_F = \frac{1}{\sqrt{2}v^2} = \frac{\sqrt{2}g^2}{8{m_W}^2} = \frac{\pi\alpha}{\sqrt{2}\sin^2\theta_W\cos^2\theta_W{m_Z}^2}. \tag{2.1}$$

Note that the small value of the effective coupling G_F is due to the heaviness of the W boson which reduces the apparent strength of the purely weak coupling g.

As mentioned in the introduction, measurements from neutrino nucleon scattering provide the best determination of $\sin^2\theta_W = 0.2283 \pm 0.0026 \pm 0.0045$. However, now that the mass of the Z boson can be measured from LEP data to a precision of about

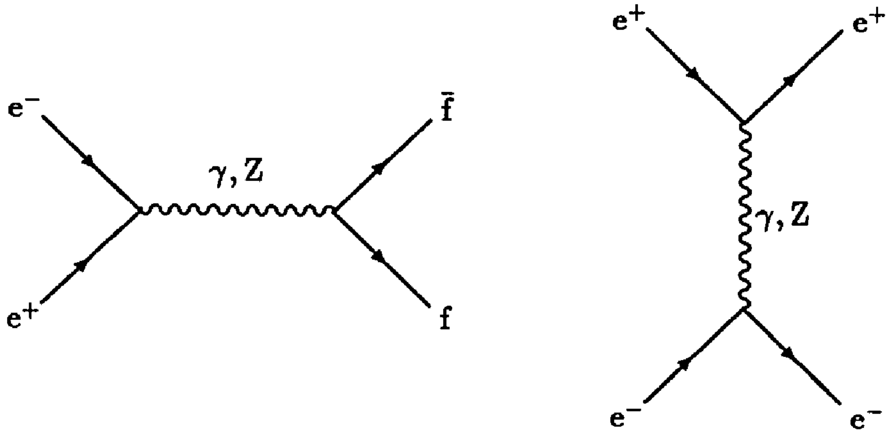

FIG. 2.2: Lowest order diagrams for e^+e^- collisions.

100 parts per million, m_Z can replace $\sin^2\theta_W$ as one of the fundamental parameters. The L3 measurement of the Z mass is $m_Z = 91.195 \pm 0.006 \pm 0.007$ [30].

2.2 The Forward-Backward Asymmetry

The lowest order diagrams for e^+e^- interactions are given in Fig. 2.2, where $\mathrm{f\bar{f}}$ represents any fermion-antifermion pair (excluding neutrinos in the case of the photon coupling). At this level all of the final states are the result of the annihilation of the e^+e^- pair except for the elastic scattering diagrams for the electron.

The forward-backward asymmetry for a pair of final state fermions is defined as the difference between the forward and backward cross-sections divided by their sum

$$A_{\mathrm{FB}} = \frac{\sigma_F - \sigma_B}{\sigma_F + \sigma_B},$$

where the forward and backward cross-sections are the differential cross-sections in-

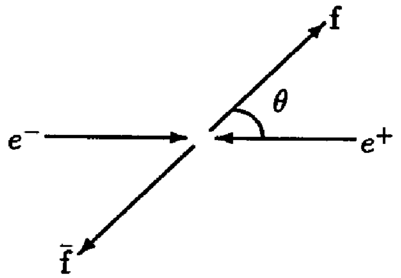

FIG. 2.3: Schematic view of e^+e^- collision in the laboratory frame of reference.

tegrated over one hemisphere

$$\sigma_F = \int_0^1 \frac{d\sigma}{d\cos\theta} d\cos\theta, \qquad \sigma_B = \int_{-1}^0 \frac{d\sigma}{d\cos\theta} d\cos\theta,$$

and θ is the angle between the incoming electron and the outgoing fermion (see Fig. 2.3).

The differential cross-section for the process $e^+e^- \rightarrow \mathrm{f\bar{f}}$ that proceeds through the annihilation of the e^+e^- pair consists of terms originating from Z exchange, γ exchange, and their interference. In the limit that the fermion mass is much less than the Z mass (which is true for all known fermions) the differential cross-section is

$$\begin{aligned}
\frac{4s}{\alpha^2 N_c^{\mathrm{f}}} \frac{d\sigma}{d\cos\theta} = \; & (1+\cos^2\theta) Q_{\mathrm{f}}{}^2 && (\gamma \text{ exchange}) \\
& -2Q_{\mathrm{f}} Re(\chi) \left[v_e v_{\mathrm{f}} (1+\cos^2\theta) + a_e a_{\mathrm{f}} 2\cos\theta \right] && (\gamma\text{-Z interference}) \\
& +|\chi|^2 \left[(v_e^2 + a_e^2)(v_{\mathrm{f}}{}^2 + a_{\mathrm{f}}{}^2)(1+\cos^2\theta) \right. && (\text{Z exchange}) \\
& \left. +4a_e a_{\mathrm{f}} v_e v_{\mathrm{f}} 2\cos\theta \right],
\end{aligned}$$

where

$$\chi = \frac{s}{s - m_Z^2 + i m_Z \Gamma_Z}, \qquad (\text{Z propagator})$$

$$a_{\mathrm{f}} = \frac{I_{\mathrm{f}}^3}{2\sin\theta_W\cos\theta_W}, \qquad v_{\mathrm{f}} = \frac{I_{\mathrm{f}}^3 - 2Q_{\mathrm{f}}\sin^2\theta_W}{2\sin\theta_W\cos\theta_W},$$

and a_e (v_e) is a_{f} (v_{f}) with the fermion being the electron, f $= e$. Q_{f} is the fermion charge, I_{f}^3 is the third component of weak isospin, $N_{\mathrm{c}}^{\mathrm{f}}$ is the number of possible color charges for the fermion, $\sqrt{s}$ is the center-of-mass energy, α is the fine structure constant, θ_W is the weak mixing angle, and m_Z, Γ_{Z} are the mass and decay width of the Z boson. Making use of the tree level Standard Model relation for G_F from Eq. (2.1), the vector (v_{f}) and axial-vector (a_{f}) couplings of the Z to any fermion f, can be written in the alternate form

$$a_{\mathrm{f}} = \left(\frac{\sqrt{2}G_F {m_Z}^2}{4\pi\alpha}\right)^{\frac{1}{2}} g_{\mathrm{A}}^{\mathrm{f}}, \qquad v_{\mathrm{f}} = \left(\frac{\sqrt{2}G_F {m_Z}^2}{4\pi\alpha}\right)^{\frac{1}{2}} g_{\mathrm{V}}^{\mathrm{f}},$$

where

$$g_{\mathrm{A}}^{\mathrm{f}} = I_{\mathrm{f}}^3, \qquad g_{\mathrm{V}}^{\mathrm{f}} = I_{\mathrm{f}}^3 - 2Q_{\mathrm{f}}\sin^2\theta_W.$$

Rewriting the differential cross-section to consolidate the angular dependence yields

$$\frac{d\sigma}{d\cos\theta} = C(s)\left[\frac{3}{8}(1+\cos^2\theta) + A_{\mathrm{FB}}(s)\cos\theta\right],$$

where

$$A_{\mathrm{FB}}(s) = \frac{3}{4}\left[\frac{-2a_e a_{\mathrm{f}} Q_{\mathrm{f}} Re(\chi) + 4a_e a_{\mathrm{f}} v_e v_{\mathrm{f}}|\chi|^2}{{Q_{\mathrm{f}}}^2 + (v_e^2 + a_e^2)({v_{\mathrm{f}}}^2 + {a_{\mathrm{f}}}^2)|\chi|^2 - 2v_e v_{\mathrm{f}} Q_{\mathrm{f}} Re(\chi)}\right]$$

$$C(s) = \frac{\alpha^2 N_c^f}{4s}\left[{Q_{\mathrm{f}}}^2 + (v_e^2 + a_e^2)({v_{\mathrm{f}}}^2 + {a_{\mathrm{f}}}^2)|\chi|^2 - 2v_e v_{\mathrm{f}} Q_{\mathrm{f}} Re(\chi)\right].$$

The pure γ exchange term affects only the normalization of A_{FB}, while the contri-

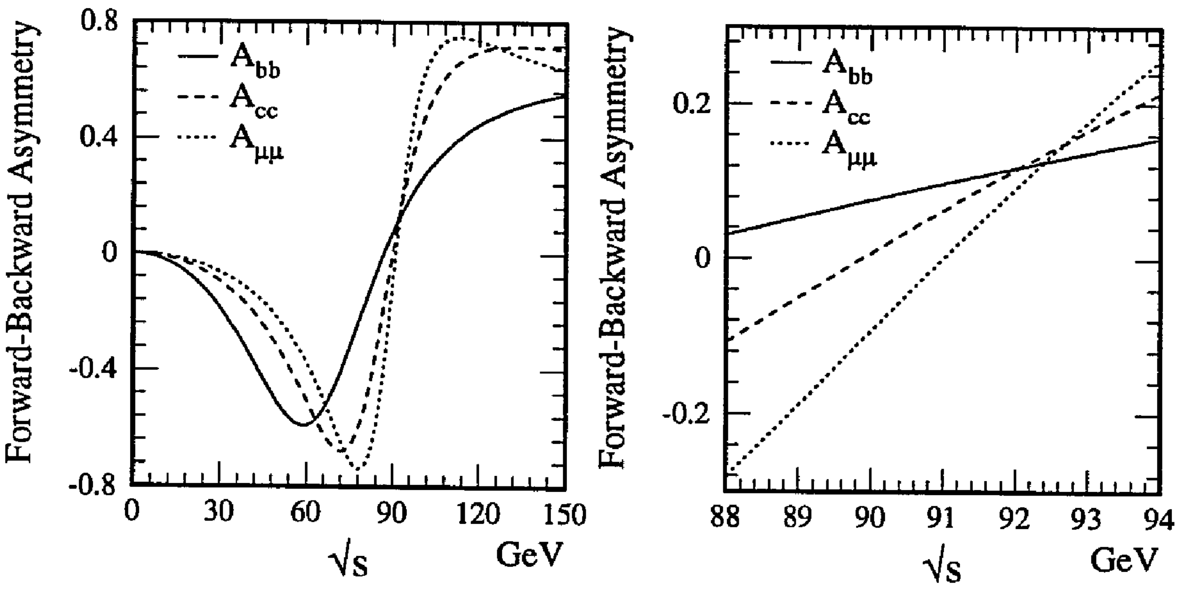

FIG. 2.4: First order calculation of the forward-backward asymmetry for $b\bar{b}$, $c\bar{c}$, and $\mu^+\mu^-$ final states as a function of center-of-mass energy for m_Z= 91.16 GeV, Γ_Z= 2.487 GeV, and $\sin\theta_W$= 0.232. Higher order corrections have not been included.

bution from the interference term and the pure Z term are opposite in sign. The asymmetry is strongly dependent on the center-of-mass energy but the only difference in the asymmetry between fermions comes from Q_f, I_f^3, and N_c^f. At this level, all up type quarks (u,c) have the same asymmetry as do all the down type quarks (d,s,b) and all the leptons (e, μ, τ). The energy dependence of the asymmetry for $\mu^+\mu^-$, $c\bar{c}$, and $b\bar{b}$ pairs is displayed in Fig. 2.4. Below the Z peak the interference term dominates, but near or above the peak the asymmetry is dominated by pure Z exchange. At a center-of-mass energy equal to m_Z, the contribution from the interference term is exactly zero and the asymmetry takes on the simple form

$$A_{\mathrm{FB}}(m_Z{}^2) = \frac{3}{4} A_e A_f, \tag{2.2}$$

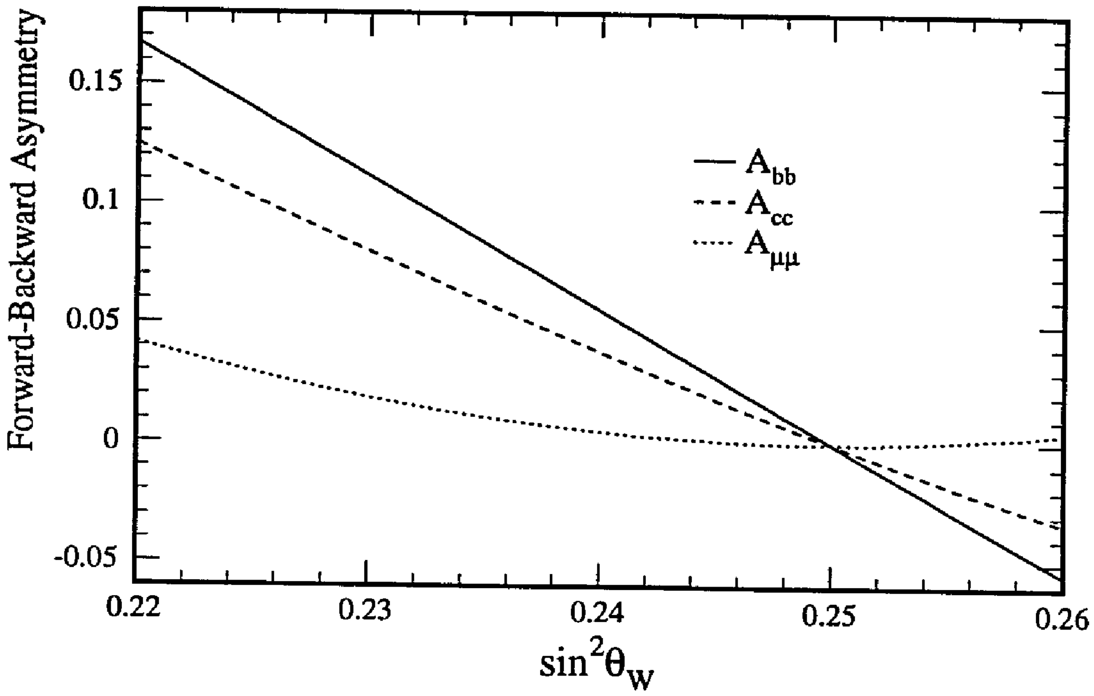

FIG. 2.5: Asymmetry for b$\bar{\rm b}$, c$\bar{\rm c}$, and $\mu^+\mu^-$ events from the first order calculation at $\sqrt{s} = m_Z$ as a function of $\sin^2\theta_W$. Note that higher order corrections have not been included.

where

$$A_f = \frac{2v_f a_f}{{v_f}^2 + {a_f}^2}, \qquad A_e = \frac{2v_e a_e}{v_e^2 + a_e^2}.$$

The relationship between the peak asymmetry $A_{\rm FB}({m_Z}^2)$ and $\sin^2\theta_W$ is shown in Fig. 2.5. Note that the b asymmetry has the greatest sensitivity to $\sin^2\theta_W$.

In principle the forward-backward asymmetry of each quark flavor can be used independently to determine $\sin^2\theta_W$. However, in practice it is extremely difficult to distinguish the flavor of the primary quarks in a given hadronic Z decay. As will be discussed in Section 2.4, because of the large mass of the b quark it is experimentally feasible to select a relatively pure sample of b$\bar{\rm b}$ pairs.

2.2.1 Higher Order Corrections

So far only the lowest order diagrams (often called the Born Approximation) have been considered. To establish the connection between the theory and experiment a number of higher order corrections must be added. These corrections can be grouped into three main categories:

1. QCD corrections, which are mostly due to radiated gluons in the final state.
2. QED radiative corrections, which include diagrams that have one or more additional photons.
3. Electroweak corrections, which encompass vacuum polarization effects, and vertex and box diagrams involving the gauge bosons.

QCD Corrections

For quark pair final states there is a correction to $A_{\rm FB}$ due to gluon bremsstrahlung. The correction is small and has a slight dependence on the mass of the final state quark (m_f). The Born level asymmetry is then modified according to

$$A_{\rm FB} \rightarrow A_{\rm FB}\left[1 - \frac{\alpha_s}{\pi}(1 - \frac{4\pi}{3}\frac{m_f}{\sqrt{s}})\right].$$

QED Corrections

The correction due to final state single photon emission is derived in an analogous fashion to the QCD correction presented above. The correction is

$$A_{\rm FB} \rightarrow A_{\rm FB}(1 - \frac{3\alpha}{4\pi}Q_{\rm f}^2)$$

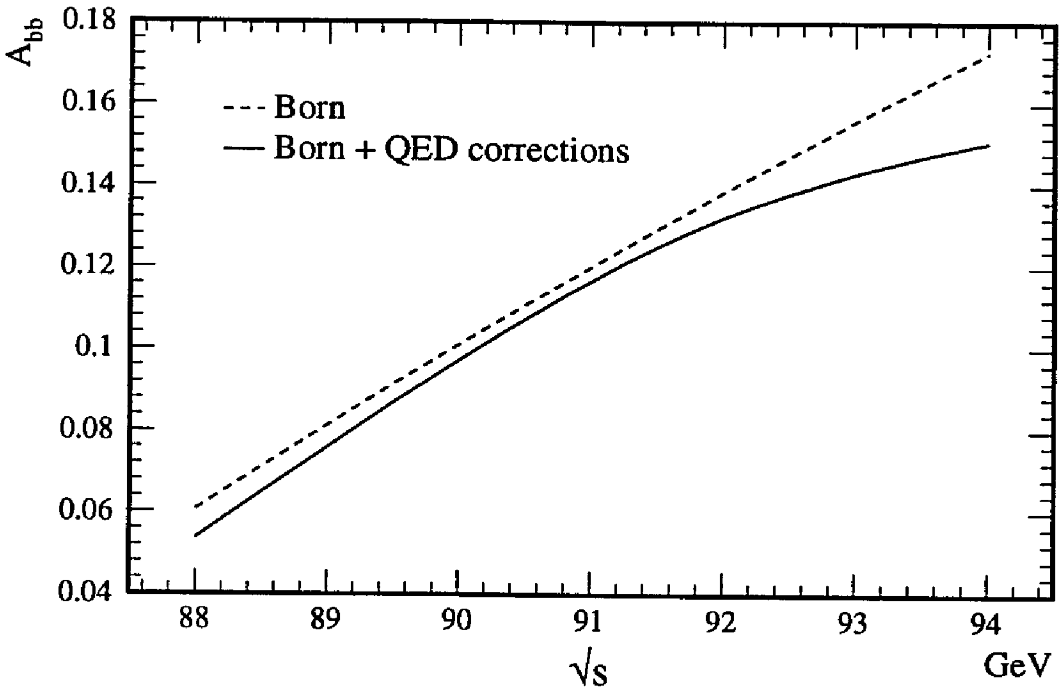

FIG. 2.6: The $b\bar{b}$ asymmetry with and without initial state photon corrections.

which is extremely small, reducing the asymmetry by a factor $< 0.17\%$.

In contrast, the effect of initial state radiation is much larger. The initial state radiated photon alters the effective center-of-mass energy of the interaction, and since the asymmetry has a strong $\sqrt{s}$ dependence this has a significant impact. The correction cannot be simply parameterized but the exact analytic $\mathcal{O}(\alpha)$ calculation can be performed and convoluted with the Born level formula for the differential cross-section. Figure 2.6 compares the energy dependence of the $b\bar{b}$ asymmetry with and without the initial state radiative corrections. The effect is larger above the mass of the Z, where the probability of radiating a real photon is greater.

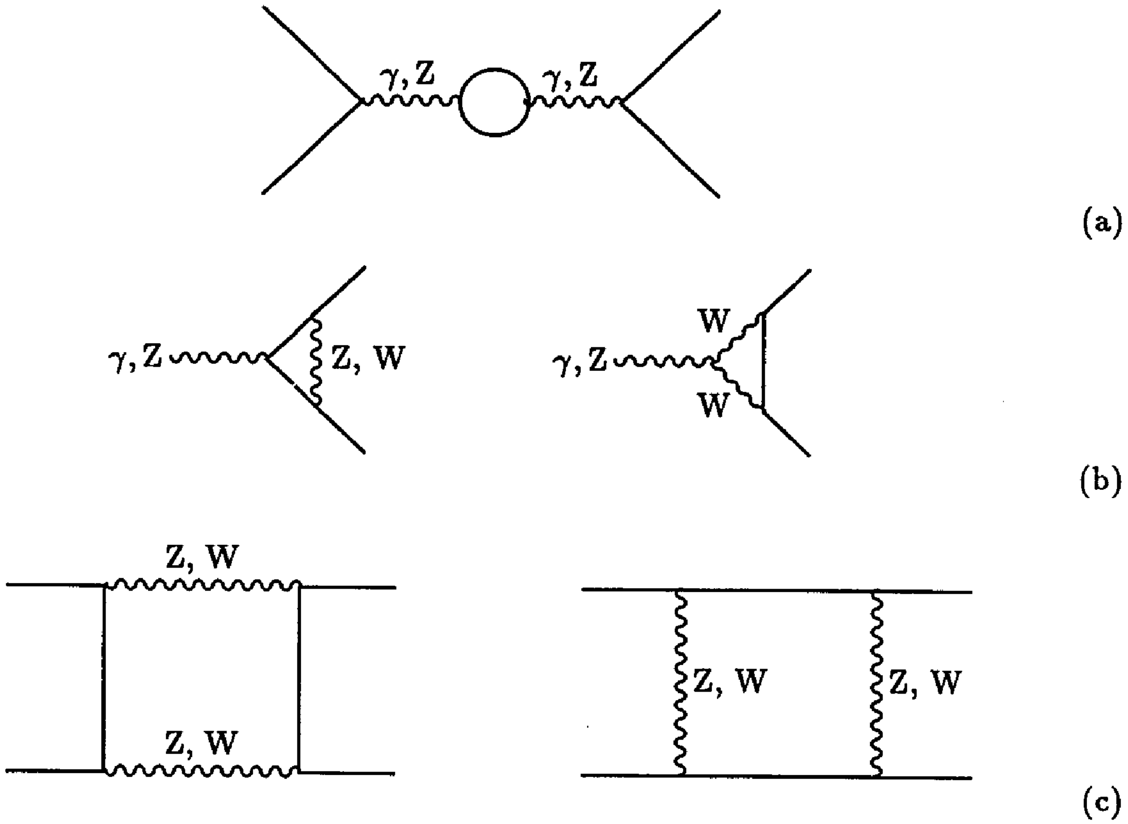

FIG. 2.7: Examples of electroweak corrections to $e^+e^-\rightarrow f\bar{f}$. The three categories are: (a) propagator corrections, (b) vertex corrections, and (c) box diagrams.

Electroweak Corrections

The major components of the electroweak corrections stem from the introduction of fermion loops into the boson propagators and the addition of heavy bosons at the fermion vertices and in box diagrams. Examples of such diagrams are given in Fig. 2.7. These modify the Born level description in the following way.

Vacuum polarization effects on the photon propagator, represented by $\Delta\alpha$, can be included by replacing α with its renormalized value at the Z mass

$$\alpha\rightarrow\alpha(m_Z^2) = \frac{\alpha}{1-\Delta\alpha} \simeq 1.064\alpha.$$

Corrections to the Z exchange diagram result in a modification to the imaginary part of the propagator

$$\chi \longrightarrow \frac{s}{(s-m_Z^2)+is\Gamma_Z/m_Z}.$$

The remaining part of the weak corrections can be accommodated by introducing form factors (ρ_{f}, κ_{f}) into the weak coupling constants

$$g_{\mathrm{A}}^{\mathrm{f}} = \sqrt{\rho_{\mathrm{f}}} I_{\mathrm{f}}^3, \quad g_{\mathrm{V}}^{\mathrm{f}} = \sqrt{\rho_{\mathrm{f}}}(I_{\mathrm{f}}^3 - 2Q_{\mathrm{f}}\kappa_{\mathrm{f}}\sin^2\theta_W).$$

The variation of the form factors for different light fermions (f $\neq$ b) is small so $\rho = \rho_{\mathrm{f}}$ and the effective weak mixing angle $\sin^2\bar{\theta}_W$ is defined to be

$$\sin^2\bar{\theta}_W = \kappa_{\mathrm{f}}\sin^2\theta_W.$$

In general, the weak form factors depend on the masses of the fermions and gauge bosons, including the unknown top quark and Higgs masses. The leading dependence of $\sin^2\bar{\theta}_W$ on the top mass can be approximated

$$\sin^2\bar{\theta}_W \simeq \sin^2\theta_W + \cos^2\theta_W\Delta\rho,$$

where

$$\Delta\rho = \frac{3G_F m_t^2}{8\sqrt{2}\pi^2}.$$

For $\mathrm{b\bar{b}}$ final states, vertex diagrams involving t quarks become important (see

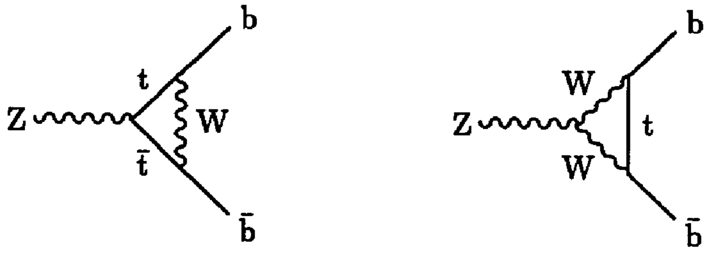

FIG. 2.8: Vertex corrections to $e^+e^-\rightarrow$b$\bar{\text{b}}$ involving the top quark.

Fig. 2.8), which introduces an additional top mass dependence that is suppressed in the corrections for the lighter quarks. Accounting for this extra dependence on m_t, the weak form factors for b quarks can be related to ρ and $\sin^2\theta_W$ by

$$\rho_{\rm b} \simeq \rho(1 - \tfrac{4}{3}\Delta\rho)$$

$$\kappa_{\rm b}\sin^2\theta_W \simeq \sin^2\bar{\theta}_W(1 + \tfrac{2}{3}\Delta\rho).$$

The effect on the asymmetry from these diagrams is negligible; however, the top mass dependence of the Z$\rightarrow$b$\bar{\text{b}}$ quark partial width is significantly changed.

2.2.2 Definitions of $\sin^2\theta_W$

In the literature there are a number of definitions of $\sin^2\theta_W$ that take different approaches to categorizing the weak radiative corrections. Complicating matters further, different authors use the same expression to represent different quantities. Presented here is an inventory of $\sin^2\theta_W$ definitions relevant for discussions of electroweak data at $\sqrt{s} \sim m_Z$.

The effective weak mixing angle $\sin^2\bar{\theta}_W$ introduced in this thesis is the standard definition used by the L3 experiment at LEP. It is often used by the other LEP experiments and appears in many review articles written in a variety of ways, for example

$$\sin^2\bar{\theta}_W \equiv \sin^2\bar{\theta}_{\text{eff}} \equiv \sin^2\theta_{\text{eff}} \equiv \sin^2\theta_W^{\text{eff}},$$

and is approximately equal to the mixing angle in the $\overline{\text{MS}}$ renormalization scheme [31]

$$\sin^2\theta_W^{\overline{\text{MS}}} \equiv \sin^2\hat{\theta}_W(m_Z) \simeq \sin^2\bar{\theta}_W - 0.0001.$$

The label $\sin^2\bar{\theta}_W$ has also been used to express a different quantity, the "universal" mixing angle introduced by Hollik [32], which does not include the corrections to the fermion vertex ($\Delta\kappa_{\text{f, vertex}}$) and is truly flavor independent. This definition is related to the effective mixing angle by

$$\sin^2\bar{\theta}_W(\text{Hollik}) = (1 - \Delta\kappa_{\text{f, vertex}})\sin^2\bar{\theta}_W \simeq \sin^2\bar{\theta}_W - 0.0007$$

and is equivalent to both the "star" mixing angle of Kennedy and Lynn [33], $\sin^2\theta_W^*$, and the renormalized mixing angle $\sin^2\theta_W(\text{Z})$ or $\sin^2\theta_W(m_Z{}^2)$ sometimes reported by the LEP experiments,

$$\sin^2\bar{\theta}_W(\text{Hollik}) \equiv \sin^2\theta_W^* \equiv \sin^2\theta_W(\text{Z}) \equiv \sin^2\theta_W(m_Z{}^2).$$

Finally, the mass shell definition advocated by Sirlin [34],

$$(\sin^2\theta_W)_S \equiv 1 - \frac{{m_W}^2}{{m_Z}^2},$$

which is equivalent to the tree level definition of $\sin^2\theta_W$, is technically independent of radiative corrections and has a complicated connection to $\sin^2\bar{\theta}_W$. Since the W mass has not been measured as precisely as the Z mass at LEP, it is treated as a derived quantity determined from the precisely measured fermi constant G_F. The relation between the W mass and G_F in the Standard Model involves electroweak corrections and therefore depends on the top quark mass. Defined in this way (by using G_F instead of m_W), $(\sin^2\theta_W)_S$ acquires a strong top mass dependence, which can be seen in Fig. 2.9. Since the electroweak corrections have been absorbed into its definition, $\sin^2\bar{\theta}_W$ is much less sensitive to the top mass. For the sake of comparison the figure also includes the value of $\sin^2\theta_W$ derived from the direct measurement of the W mass by the CDF and UA1 collaborations, $m_W = 80.22 \pm 0.26$ [35], and the Z mass from L3.

2.3 Fragmentation

Electron-positron annihilation at LEP produces a quark-antiquark pair that has sufficient kinetic energy to overcome the attractive electromagnetic potential between the quarks. However, isolated quarks have never been observed in nature. All the hadronic matter that has been detected is made of color neutral combinations of

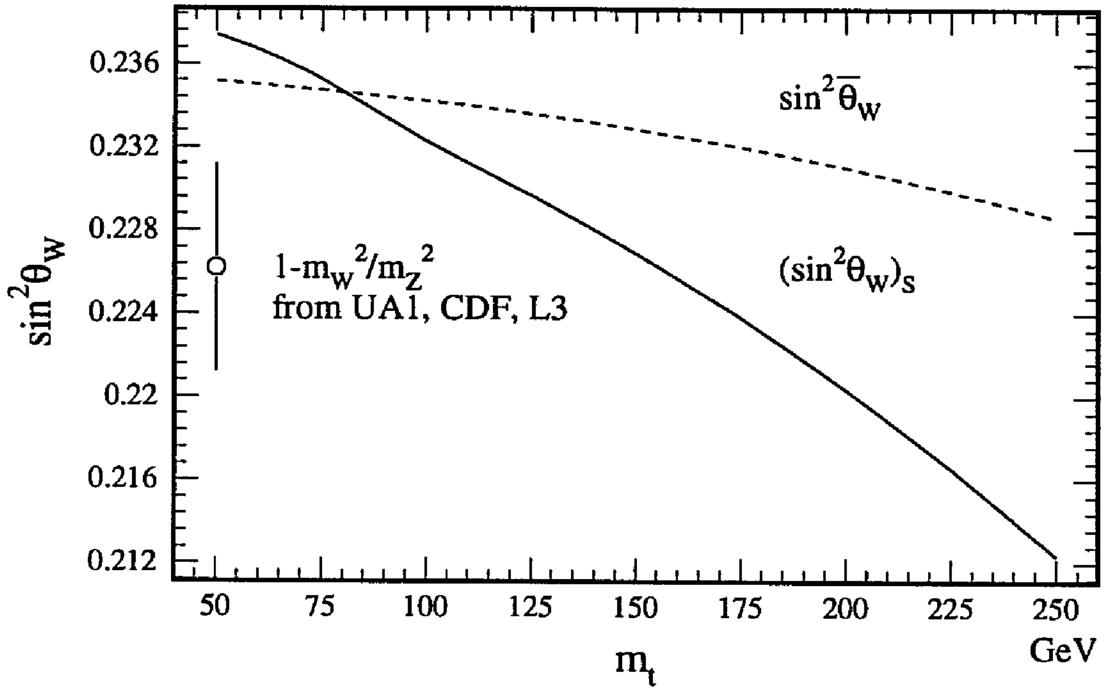

FIG. 2.9: Top mass dependence of the effective weak mixing angle $\sin^2\bar{\theta}_W$ and the mass shell definition of $(\sin^2\theta_W)_S$ in the framework of the Standard Model. For comparison $(\sin^2\theta_W)_S$ from the direct measurements of the W and Z mass is 0.2262 ± 0.0050.

quarks.

Attempts to separate a quark from a hadron result in the production of additional hadronic particles. In QCD this is explained by producing $q\bar{q}$ pairs from the vacuum to form new hadrons. In a similar manner, as the quarks produced in an e^+e^- collision move apart, $q\bar{q}$ pairs are drawn out of the vacuum to form clusters of hadrons that on average travel in the same direction as the original quarks. The cluster of hadrons that is associated with the original quark is called a "jet," and the process of producing the hadronic configuration is referred to as fragmentation or hadronization.

The details of quark fragmentation are in principle completely determined by QCD. However, due to the increase in coupling strength of the strong interaction at long distance scales (i.e. quark confinement) perturbative calculation techniques are not applicable and alternative techniques have not proved soluble. Instead, various phenomenological models have been proposed that encapsulate the concepts of QCD but allow a calculable description of the fragmentation process.

The models currently in use can be grouped into two categories: string fragmentation and QCD cascades. String fragmentation models [36, 37] are based on the idea that the hadronic color field forms a flux tube between the primary partons (quarks and gluons). As the partons move apart, the flux tube, which has a constant energy density per unit length, stretches between them. When the potential energy in the string (flux tube) is sufficient to produce a $q\bar{q}$ pair, the string can break into two separate strings. This process occurs repeatedly until the energy in the color field is insufficient to produce any further quark pairs.

In QCD cascade models [38–41] a quark-gluon shower is generated (much like an electromagnetic shower of electrons and photons) using a perturbative QCD expansion. This is achieved by producing the initial partons off their mass shell and allowing them to radiate gluons, and then terminating the shower when the parton four-momentum is small enough to prohibit the use of perturbation theory. The remaining gluons are split into $q\bar{q}$ pairs and the quarks are combined into multiquark color singlet clusters which decay into the final hadrons.

Currently, the most popular model used for e^+e^- collisions (and the model preferred by L3) is a combined approach implemented by the Lund Group [42, 43] in the Lund Monte Carlo program [44]. A perturbative QCD parton shower model is used to generate the effects of hard gluon bremsstrahlung and to produce partons which are then fragmented with the string model.

In all of the models a fragmentation function must be specified which describes how much of the initial quark momentum is carried by the hadron formed with the initial and vacuum quarks. Fragmentation functions are typically parameterized by a partially Lorentz invariant quantity that compares the hadron momentum four-vector to the initial quark four-momentum:

$$z = \frac{(E + p_{||})_{\mathbf{hadron}}}{(E + p_{||})_{\mathbf{quark}}},$$

where $p_{||}$ is the component of momentum parallel to the initial quark direction. Note that the parameter z is invariant under a boost in the direction of the initial quark.

For light quarks (u, d, s), the properties of the string model lead to a symmetric fragmentation function [45] of the form

$$f(z) \propto z^{-1}(1-z)^{a} \exp(-bm_T^2/z),$$

where $m_T^2 = m^2 + p_T^2$ is the transverse mass of the hadron. The transverse momentum of the hadron is chosen at random from a Gaussian probability distribution with zero mean and variance σ_T^2. The free parameters can be chosen such that the fragmentation scheme reproduces experimentally observed particle and jet distributions; the values typically fall in the range $a = 0.5 - 1.0$, $b = 0.7 - 0.9$ GeV^{-2} and $\sigma_T \sim 0.3$ GeV.

Heavy quark (c, b) fragmentation is treated differently. Hadrons are more likely to form when the constituent quarks have the same velocity. This implies that heavy quarks can combine with light quarks without giving up much of their energy and thus the heavy meson will carry a higher fraction of the momentum of the original heavy quark [46–48]. Thus, the fragmentation of heavy quarks is described as being "hard." An explicit model of heavy quark fragmentation introduced by Peterson *et al.* [49] displays this general feature. The Peterson fragmentation function is parameterized by a single flavor dependent quantity ϵ_Q:

$$f(z) \propto z^{-1}\left(1 - \frac{1}{z} - \frac{\epsilon_Q}{1-z}\right)^{-2}.$$

That heavy quark fragmentation is hard has been unambiguously determined from studies of heavy meson decays at PEP and PETRA [50, 51]. The Peterson fragmentation function fits the data quite well; however, measurements have not been sufficiently precise to distinguish between different fragmentation models.

In the L3 simulation, the Peterson function is used for heavy quark fragmentation with $\epsilon_c = 0.07$ and $\epsilon_b = 0.008$ and the Lund symmetric function is used for the lighter quarks with $a = 0.5$, $b = 0.9$ GeV^{-2}, and $\sigma_T = 0.35$ GeV. Figure 2.10 illustrates the degree to which the fragmentation of light and heavy quarks differ given this choice of parameters.

For comparisons with real data, the Peterson function was used with x_E as the parameterization variable instead of z, where $x_E = 2E_{\text{hadron}}/\sqrt{s}$. This leads to fragmentation parameters $\epsilon_b(x_E)$ and $\epsilon_c(x_E)$ which differ from the corresponding parameters ϵ_b and ϵ_c. Measurements from L3 data indicate that the b fragmentation parameter

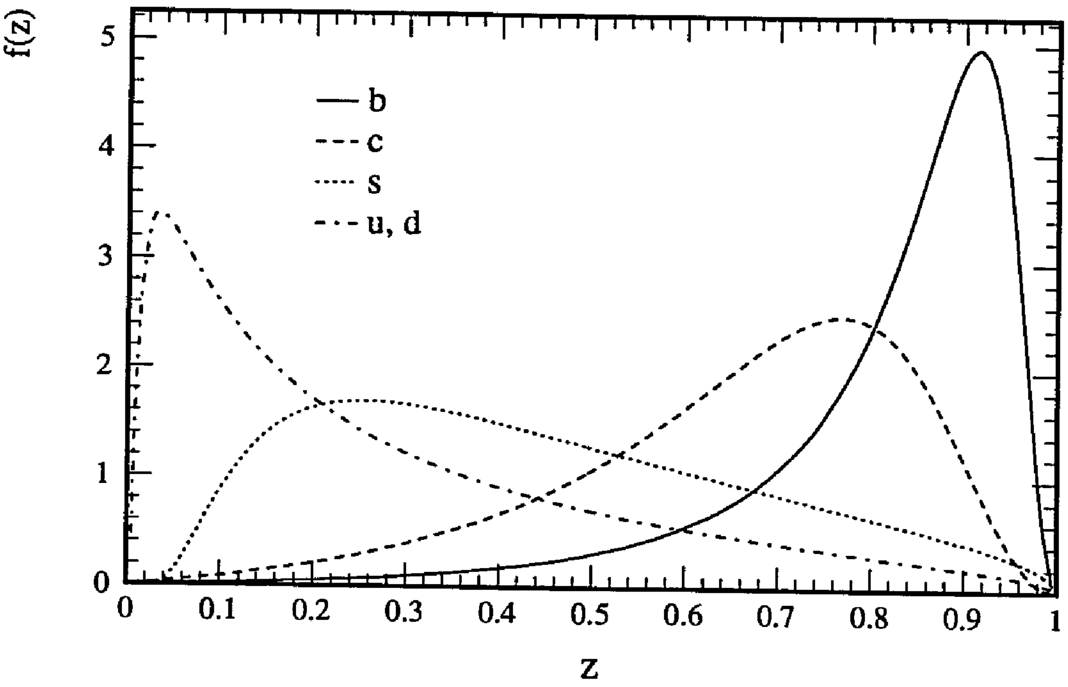

FIG. 2.10: Peterson fragmentation function for b and c quarks and Lund symmetric fragmentation function for u, d, and s quarks (parameters as given in the text). The functions are normalized such that $\int f(z)dz = 1$.

is $\epsilon_b(x_E) = 0.050 \pm 0.004 \pm 0.010$ [30, 52]. Extrapolations from PEP and PETRA measurements result in $\epsilon_c(x_E) = 0.5 \pm 0.1$ [50]. These values are consistent with the values of ϵ_b and ϵ_c used in the L3 simulation.

2.4 Semileptonic Decay of b Hadrons

The semileptonic decay of b hadrons provides a method for tagging the b charge and separating b events from background. Since the b quark is heavy, the decay of b hadrons can be treated with the spectator approximation in which the b quark decays weakly via the emission of a virtual W boson and is unaffected by the presence of the light *spectator* quark (or quarks, in the case of a baryon). The virtual W will decay

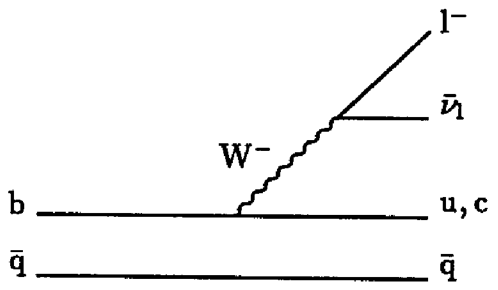

FIG. 2.11: Spectator diagram for the semileptonic decay of a b meson. For the decay of a b baryon substitute a quark pair for q̄.

into a lepton-neutrino pair or a quark-antiquark pair that has the same total charge as the original W. The semileptonic decay b→q $\ell^-\bar{\nu}_\ell$ in the spectator approximation is depicted in Fig. 2.11. Note that the charge conjugate of this process is b̄→q $\ell^+\nu_\ell$ and therefore the lepton charge distinguishes the decay of a b from a b̄ quark.

These decays, abbreviated by b→ℓ, are sometimes referred to as "prompt" indicating that the lepton comes directly from the original quark. The term differentiates this kind of decay from "cascade" decays such as b→c→ℓ, where the lepton comes from a secondary weak decay.

The shape of the lepton momentum spectrum depends on the details of the specific process, but the maximum allowable momentum (end-point) is fixed by the initial and final state masses. Since the b quark is much heavier than the other quarks, this opens the possibility of distinguishing leptons from the decay of different quark flavors. For a general three body semileptonic decay of a hadron A to a hadron X (A→X l $\bar{\nu}_l$), the maximum lepton momentum is (neglecting the lepton mass):

$$p_{\max} = \frac{m_A^2 - m_X^2}{2m_A}.$$

Using typical masses for each type of flavored hadron, the end-point momentum is given in Table 2.3. Leptons with more than 1 GeV of momentum come almost exclusively from the weak decay of a b quark. This information cannot be used directly in the analysis of real data because the laboratory frame does not correspond to the hadron rest frame. In the process of fragmentation, the initial state hadron acquires appreciable kinetic energy and therefore the hadron and its decay products are boosted in the laboratory frame. Since the boost in a particular event is not known, the momentum of the lepton in the hadron rest frame cannot be determined. However, the momentum component of the lepton perpendicular to the direction of the hadron is not affected by the boost. This direction is correlated with the experimentally determined jet axis. The lepton momentum component perpendicular to the nearest jet axis (p_T) is a well defined experimental quantity that can be used to distinguish b decays from background. Figure 2.12 compares the p_T of leptons from

Table 2.3: Maximum momentum of lepton from semileptonic decay in the rest frame of the original hadron.

quark	hadron	(GeV) mass	(GeV) $p_{\max}$
b	B	5.3	2.3
c	D	2.0	0.94
s	K	0.5	0.23
u,d	π	0.14	0.07

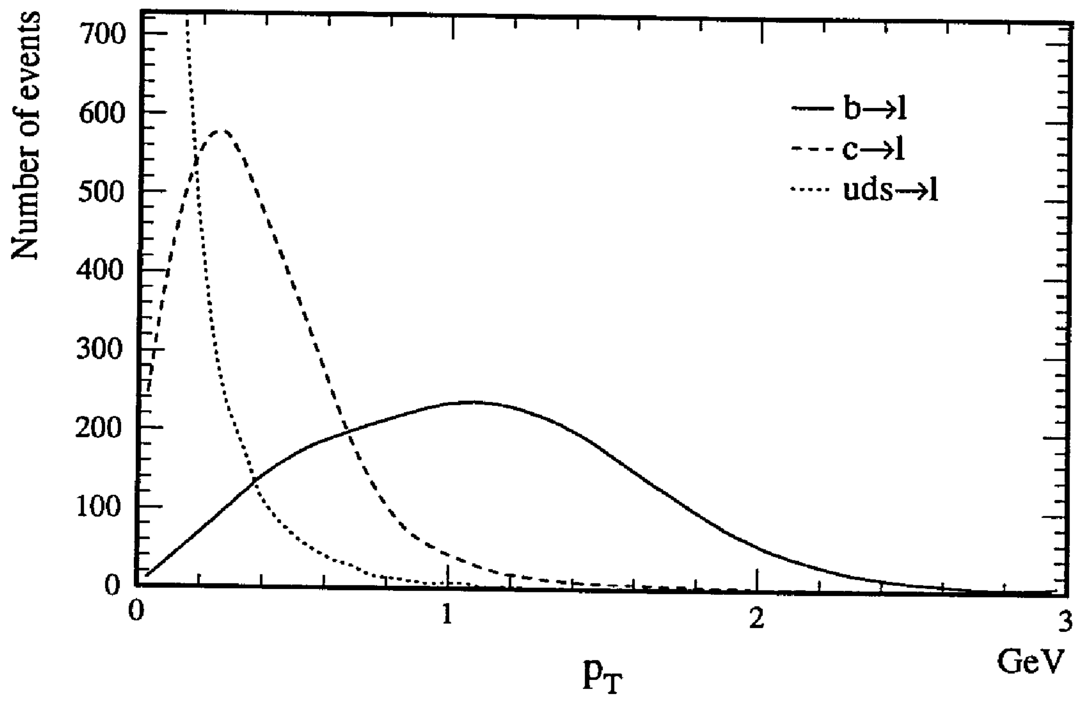

FIG. 2.12: Lepton transverse momentum with respect to the jet axis (p_T) from simulated e^+e^- events. The plots are normalized to equal area. Note that the light quark (uds) distribution extends beyond the plot limits.

simulated e^+e^- annihilation events. As expected, each decay type cuts off at $p_T = p_{\text{max}}$. The few events found above the cutoff are due to the fact that the jet axis does not exactly correspond to the hadron direction.

In semileptonic weak decays, every lepton has an associated neutrino. The neutrino energy is not deposited in the detector and thus the energy of the observed jet will be less than the available energy of the original hadron. The same arguments about the maximum momentum of the lepton also apply to the neutrino. The neutrinos in b decay will on average have more momentum than neutrinos from the weak decay of lighter quarks. This can be exploited to gain extra sensitivity to semileptonic b decays; however, the neutrino and lepton momenta are correlated due to momentum conservation. This correlation can be clearly seen in Fig. 2.13. Thus the missing

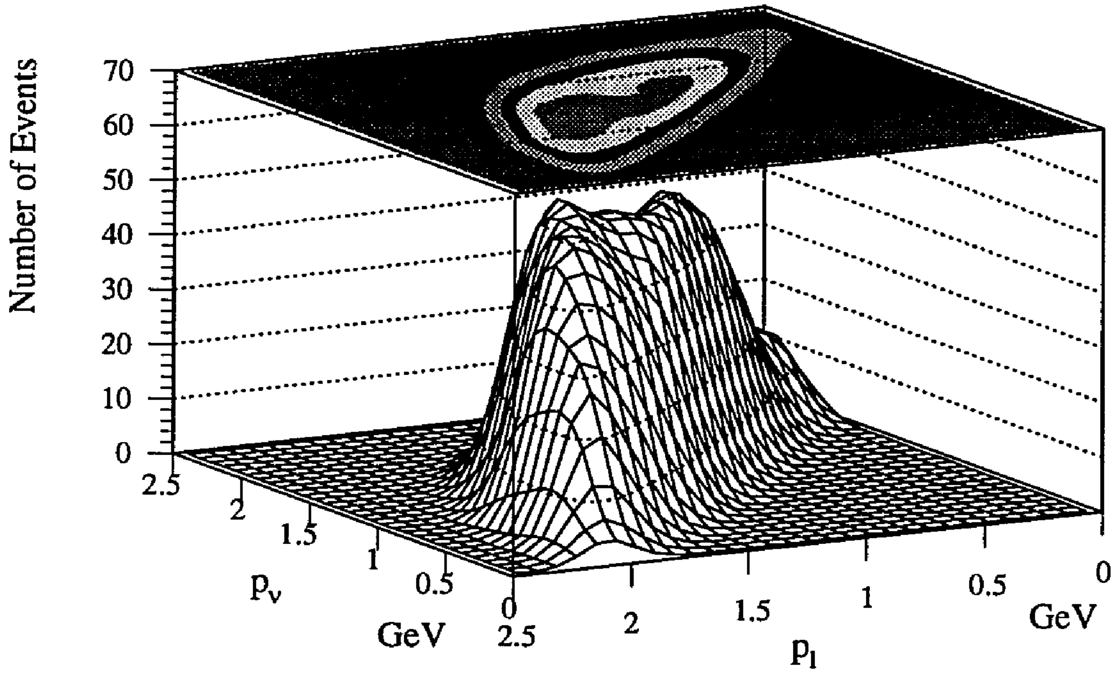

FIG. 2.13: Correlation between lepton and neutrino momentum in the rest frame of the b hadron. The contour plot is displayed above the smoothed two dimensional histogram.

neutrino energy is greatest when the lepton momentum (and therefore p_T) is small.

The b semileptonic branching ratio to electrons and muons has been measured at a number of center-of-mass energies. Table 2.4 lists results from CESR, PEP, PETRA and L3 [30, 53]. The measurements at the $\Upsilon(4S)$ have a model dependence that contributes an error which is not included in the listed value and is roughly the same size as the statistical error. Also, measurements at the $\Upsilon(4S)$ do not include contributions from B_s^0 mesons and B baryons since there is insufficient energy to produce them. It is therefore appropriate to average the higher energy measurements which results in $Br(b\rightarrow\ell) = 0.117 \pm 0.006$. This implies that one can expect approximately 41% of the $b\bar{b}$ events produced at LEP to contain at least one electron or muon from the semileptonic decay of a b quark.

Table 2.4: Measurements of the b semileptonic branching ratio.

Br(b→ℓ)	$\sqrt{s}$ (GeV)	
0.118 ± 0.005	10.58	Υ(4S)
0.118 ± 0.007	29-38.5	
0.113 ± 0.012	88-94	L3

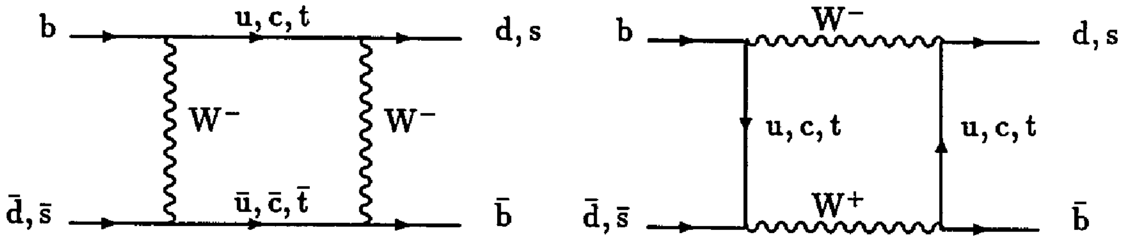

FIG. 2.14: Standard Model diagrams for B^0-$\bar{B}^0$ mixing. The charge conjugate processes can also occur.

2.5 B^0-$\bar{B}^0$ Mixing

The measurement of the $b\bar{b}$ asymmetry requires that the charge of the initial b (or $\bar{b}$) quark be determined by detecting the lepton from the weak decay of the heavy quark. In the neutral B meson system the lepton tagging method can give the wrong sign for the initial quark. Within the framework of the Standard Model, the $\bar{B}^0$ meson can oscillate into a B^0 meson via box diagrams as in Fig. 2.14. The weak decay of the meson after the oscillation result in a lepton with a charge opposite in sign to that of the original quark. The joint probability that a primary b quark hadronizes into a neutral B meson which undergoes an oscillation before the semileptonic decay of the b quark is defined to be

$$\chi \equiv \frac{BR(b \to \bar{B}^0 \to B^0 \to \ell^+ X)}{BR(b \to b - \text{hadron} \to \ell^\pm X)}.$$

The observed asymmetry is then related to the true $b\bar{b}$ asymmetry by

$$A_{b\bar{b}}^{obs} = A_{b\bar{b}}(1 - 2\chi).$$

Mixing can be experimentally observed in $b\bar{b}$ events in which both mesons are tagged via their semileptonic decay. Without mixing, the two leptons will have opposite charge. If one of the mesons has oscillated into its antiparticle then the two leptons will have the same sign.

The first evidence for B^0-$\bar{B}^0$ mixing came in 1987 from an excess of like-sign dimuon events collected by the UA1 experiment at CERN [54,55]. Subsequently, mixing has been observed at the $\Upsilon(4S)$ by ARGUS [56,57] and CLEO [58] and by the CDF collaboration at the Fermilab proton collider [59]. Unlike the proton colliders and LEP, the e^+e^- colliders operating at the $\Upsilon(4S)$ resonance do not have sufficient energy to produce B_s^0 mesons. Therefore ARGUS and CLEO directly measure the mixing of B_d^0 mesons.

The mixing parameter χ that is needed for the determination of $A_{b\bar{b}}$ is a combination of B_s^0 and B_d^0 oscillations and can be measured from L3 dilepton data without invoking measurements at other energies.

Chapter 3

Apparatus

3.1 LEP

The Large Electron Positron (LEP) collider at CERN was conceived in 1976 as a high luminosity electron-positron storage ring capable of attaining center-of-mass energies of 200 GeV. The final design approved in December of 1981 (the same year as the discovery of the Z boson) called for two phases of the project [60]. In Phase 1 LEP would operate at center-of-mass energies near the Z mass with a luminosity of $10^{31}\mathrm{cm}^{-2}\mathrm{s}^{-1}$. In the second phase of operation, the accelerating capacity of the machine would be increased to boost the center-of-mass energy to 200 GeV. Thus the Phase 1 magnet system was designed to be compatible with the higher center-of-mass energy in the second phase.

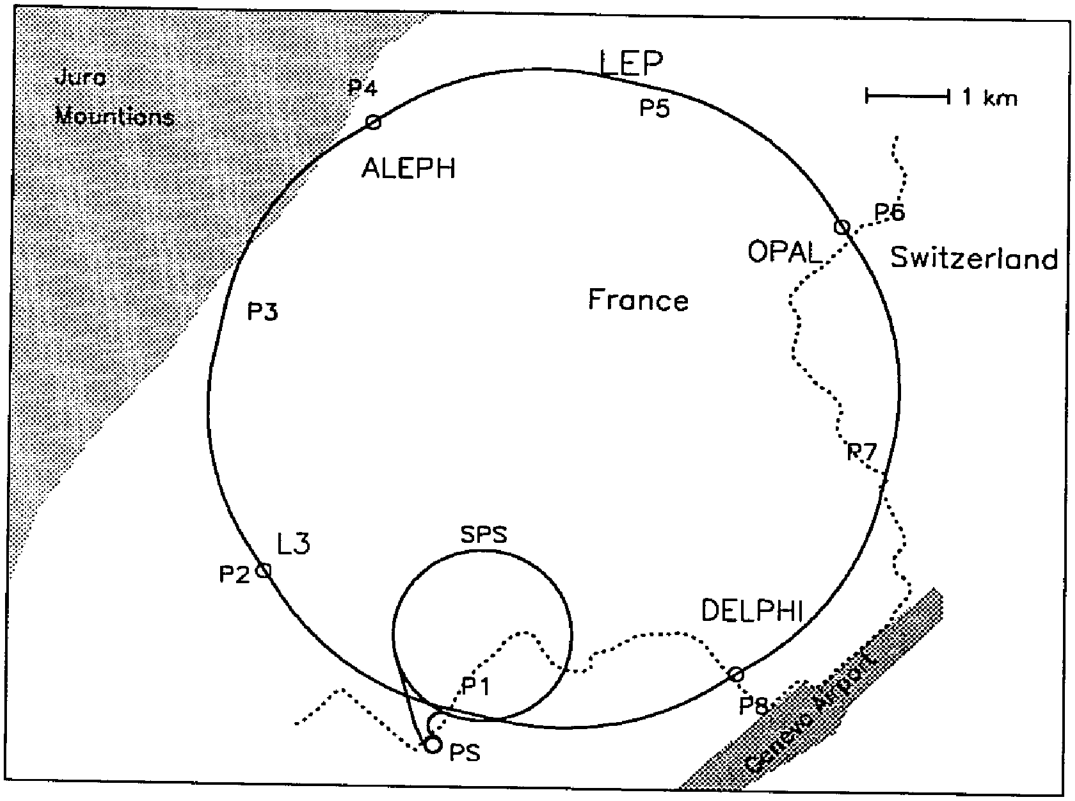

FIG. 3.1: Large Electron Positron Collider (LEP) at CERN.

3.1.1 LEP Main Ring

The main ring of the collider straddles the border between France and Switzerland on the outskirts of Geneva (Fig. 3.1). The ring has the shape of an octagon with rounded corners and has a total circumference of 26658.883 m. The circulating beams are brought into collision at eight interaction regions which are located at the middle of each straight section of the ring. Four of these interaction regions (P2, P4, P6, and P8) have large underground experimental halls and superconducting low-β quadrupole magnets. These superconducting quadrupoles compress the beam at the interaction point and thereby increase the luminosity. The other four regions (P1, P3, P5 and P7) have a simpler arrangement of standard magnets and no experimental halls.

The radio frequency (RF) accelerating system for Phase 1 is installed in the

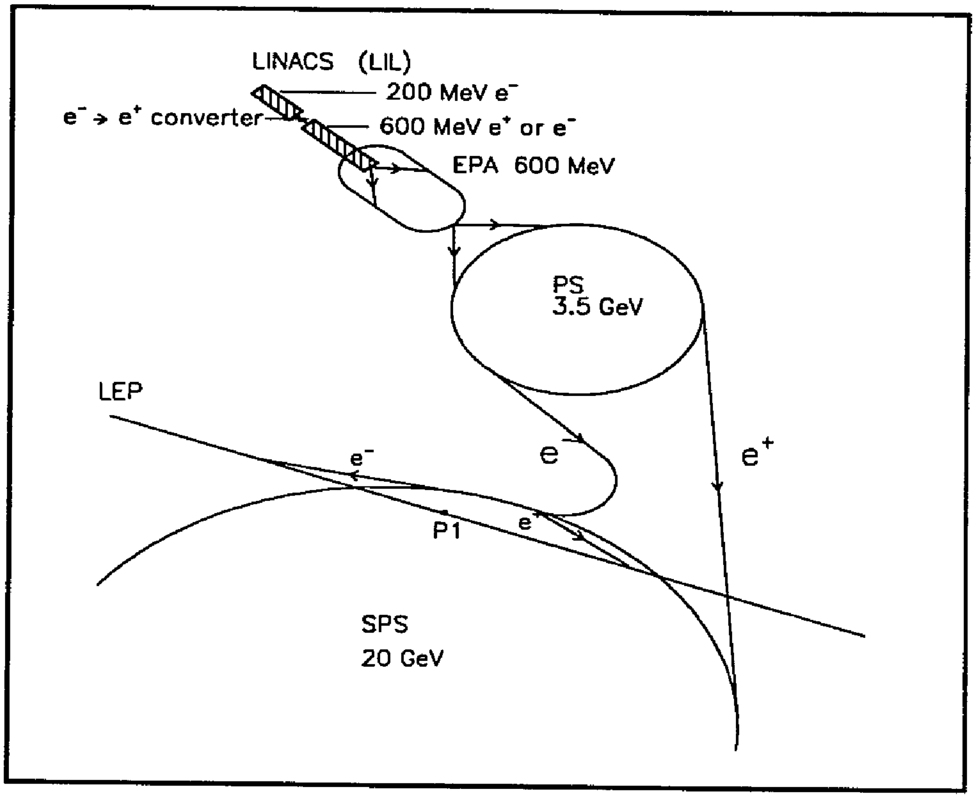

FIG. 3.2: The LEP injection system.

straight sections on either side of P2 and P4. It consists of 128 copper cavities driven by a total of 16 klystrons. The total power consumed by the klystrons is 16 Megawatts under normal operating conditions.

3.1.2 LEP Injector

The injection system for LEP utilizes the Super Proton Synchrotron (SPS), the Proton Synchrotron (PS), a specially built pair of linacs (LIL) and an e^+e^- storage ring (EPA), see Fig. 3.2 [61]. The LEP Injector Linacs (LIL) provide 600MeV electrons and positrons that are then stored in the Electron-Positron Accumulation Ring (EPA). LIL consists of a high-intensity linac that produces a 200 MeV beam of electrons which is focused onto a tungsten target to produce positrons. The positrons are accelerated by a second linac to 600 MeV and stored in EPA. A low intensity electron gun that is located near the converter provides the electrons used for filling LEP. Thus the high intensity 200 MeV linac is only used for positron filling.

Once the required current is reached, eight bunches are injected into the PS, accelerated to 3.5 GeV, and then transferred to the SPS, where the beams are accelerated to 20 GeV and then sent to LEP. The accelerating cycles of the electrons and positrons in the SPS are inserted during the dead-time of the 450 GeV proton cycle. Therefore, the filling of LEP does not interfere with the fixed target proton program of the SPS. However, filling LEP is incompatible with use of the SPS as a proton-antiproton collider.

3.1.3 LEP Operation

The data used for this thesis was collected from April 1990 to November 1991. During that time, LEP was operated with 4 electron and 4 positron bunches with a current of about 0.5 mA in each bunch and a typical beam lifetime of 20 hours. The time between beam crossings in 4×4 bunch mode is approximately 22 μs.

By the end of 1991, peak luminosities of around $5 \times 10^{30}\mathrm{cm}^{-2}\mathrm{s}^{-1}$ were attained. The history of the integrated luminosity delivered to the L3 detector is given in Fig. 3.3. The combined integrated luminosity is 19.25 pb^{-1}. The collider was run at a number of different energies scanning the Z resonance to determine the mass and decay width of the Z boson. A large amount of integrated luminosity was devoted to a center-of-mass energy close to the peak of the Z resonance. In this way the

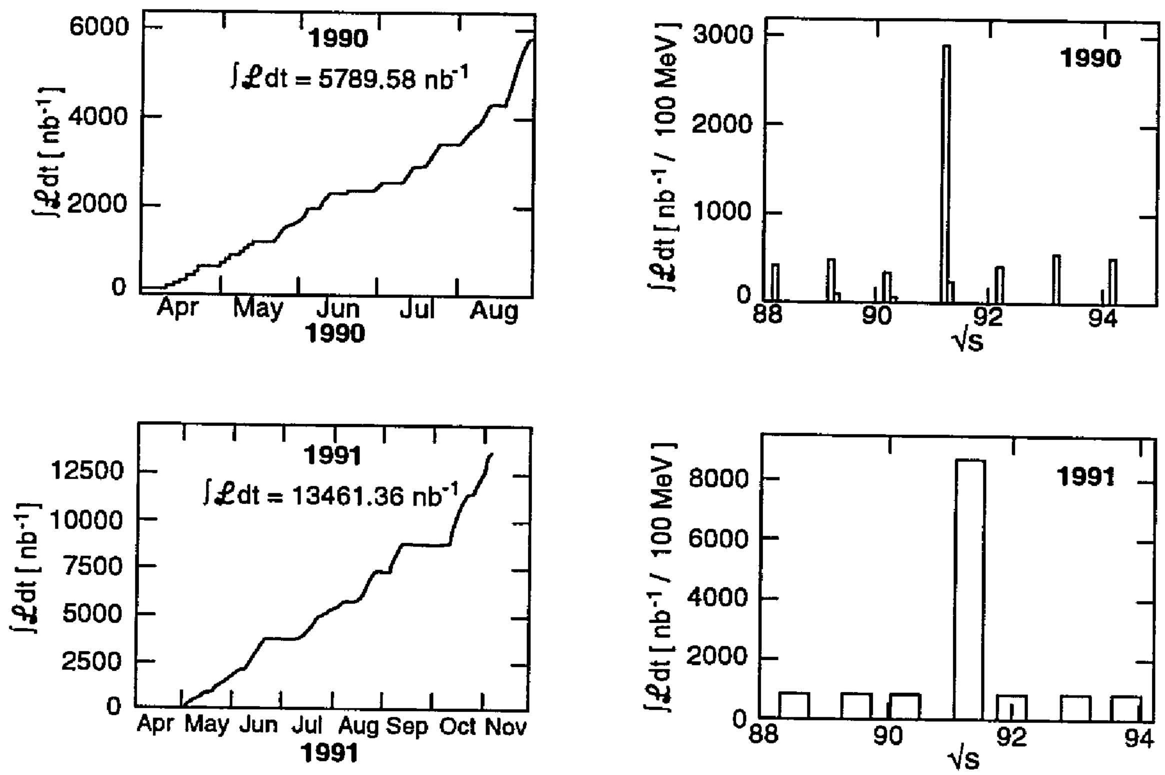

FIG. 3.3: Integrated luminosity delivered to L3 in 1990 and 1991.

enhancement of the e^+e^- cross-section was exploited to obtain the largest possible sample of Z decays, enabling the LEP experiments to make precision electroweak measurements such as the $b\bar{b}$ asymmetry.

3.2 The L3 Detector

The L3 experiment[1] [62], which is located at the P2 interaction region, is one of the four major detectors at the LEP collider. The detector was designed to identify and measure electrons, photons and muons with high precision. Although the main emphasis is on leptons and photons, the L3 detector is also capable of reconstruct-

---

[1] The experiment became known as "L3" because the Letter of Intent in which it was proposed was the third letter submitted to the LEP experiments committee.

ing hadronic jets. The combination of jet reconstruction and lepton identification make the L3 detector extremely well suited for studying heavy flavor physics through semileptonic decays.

The detector, shown in Fig. 3.4, is situated in an underground hall 50m from the surface. From the interaction region outward, the detector consists of a central tracking chamber, an electromagnetic calorimeter, a hadronic calorimeter, three sets of muon chambers and a conventional magnet coil. Unlike most high energy collider experiments, the entire detector fits inside the coil. The field provided by the magnet causes charged particle trajectories to bend so that the momentum of each particle can be determined by measuring the bending curvature. Since they are inside the coil, the central tracking chamber and muon chambers both measure the momentum of charged tracks.

The calorimeters and central tracking chamber are contained within a 32m long, 4.45m diameter steel support tube. Both ends of the muon chamber are also anchored to the tube. The tube carries the weight of the detectors to adjustable jacks on concrete pillars placed at either end of the detector. Servomechanisms in the adjustable jacks allow the detector to be aligned with the LEP beam axis.

In addition to the main detector, the beam luminosity is measured by detecting low angle e^+e^- (Bhabha) scattering events with a dedicated luminosity monitor on each side of the interaction region.

The detailed description of the detector that follows pertains to the experimental configuration used from November 1990 through November 1991.

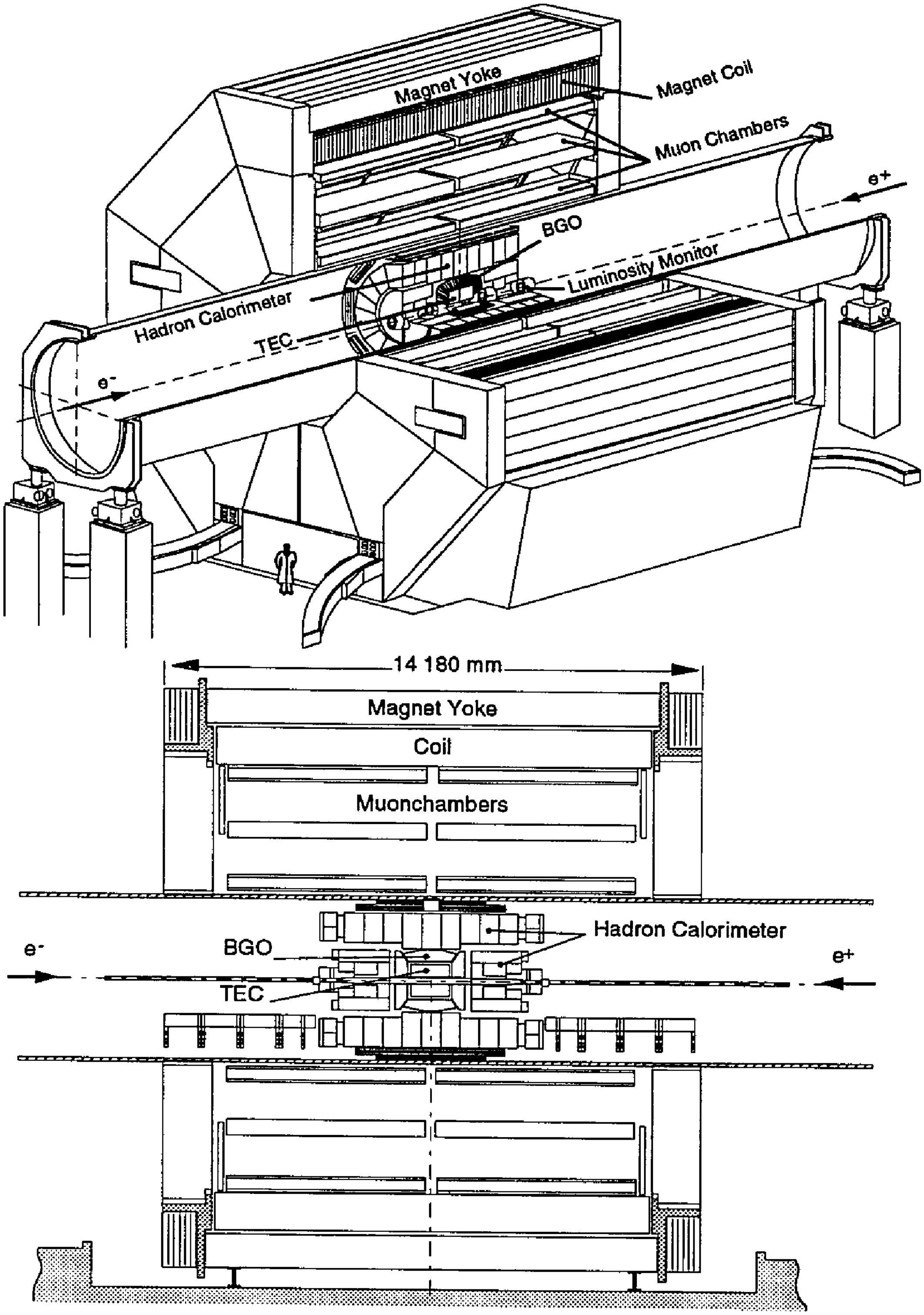

FIG. 3.4: The L3 detector.

3.2.1 Magnet

Surrounding the entire detector is a conventional solenoidal magnet which provides a 0.5 Tesla magnetic field parallel to the axis of the beam. The magnet is constructed of aluminum plates welded together to form a 168 turn octagonal coil. The inside diameter of the coil is 11.86 meters and the total length is 11.9 meters. The magnetic field is returned through an iron yoke and two poles equipped with hinged doors that permit access to the muon chambers during shutdowns.[1] A current of about 30,000 amps is required to achieve the 0.5 Tesla field.

With the hadron calorimeter removed, the magnetic field inside the support tube has been mapped with a remote controlled device equipped with 60 Hall plates. The remaining region of the detector was mapped with 1000 magnetoresistors that are permanently attached to the muon chamber support structure and the absolute value of the field is monitored with five NMR probes.

3.2.2 Muon Tracking Chambers

The muon detector (MUCH) resembles a pair of side-by-side ferris wheels concentric with the beam pipe. Each wheel consists of eight triangular units or octants. Each octant (see Fig. 3.5) contains an inner module (MI), two middle modules (MM), and two outer modules (MO). The inner and outer modules measure track coordinates in

---

[1] It has been erroneously stated that the L3 magnet system contains more iron than the Eiffel Tower in Paris. The total amount of iron in the magnet support structure and return yoke is 6700 tons, while the Eiffel tower contains 7300 of iron and steel [63]. Including the 1100 tons of aluminum that make up the magnet coil then it can be said that the L3 magnet system *outweighs* the Eiffel Tower.

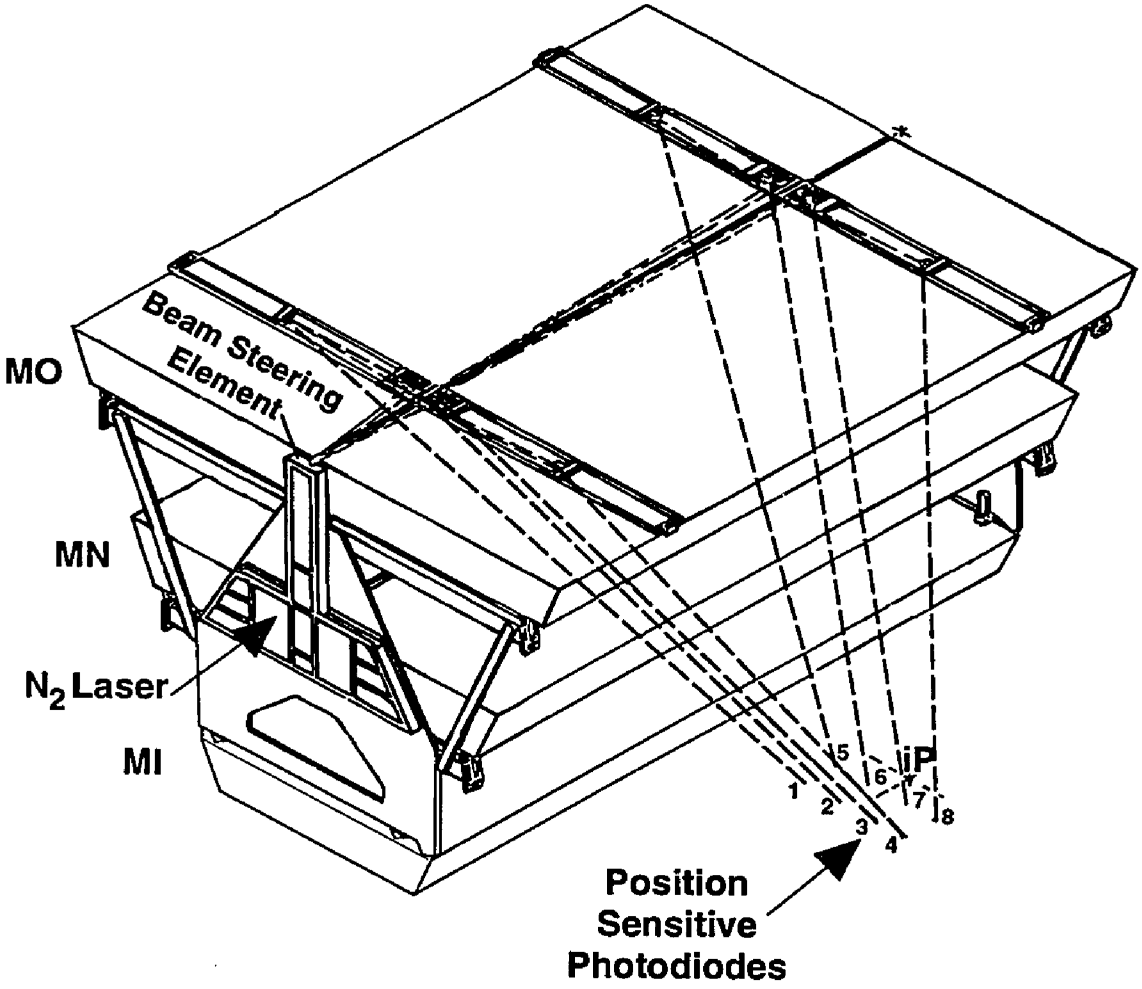

FIG. 3.5: One octant of one wheel of the muon chambers.

the bending plane of the magnetic field with 16 signal wires each (p-chambers). They are also equipped with additional chambers that measure track coordinates along the beam axis (z-chambers). The middle modules do not have z-chambers and devote 24 wires to the bending plane measurement. The chambers cover the polar region between 36° and 144° with respect to the beam pipe.

Muon Chamber Alignment

The curvature of a muon track with momentum greater than 3 GeV is small enough that the track can be contained within a single octant. Alignment of modules within an octant is therefore more critical than the octant to octant alignment. Separate systems are used to position the wires within a module, to position the modules within an octant and to check the overall alignment.

Precision Pyrex glass and carbon fiber bridges hold the signal and field shaping wires within a chamber. The position of the bridges is adjusted with three alignment systems integrated into the structure. Each alignment system is composed of a light emitting diode (LED) focused onto a quadrant photodiode. The bridges are aligned when an equal amount of light is received by each quadrant of the photodiode. In this way, the wires are positioned to an accuracy of 10 μm in the bending direction and 40 μm in the non-bending direction.

The ends of each module are aligned with a similar system of LEDs and photodiodes. Two LEDs which are referenced to a signal wire are attached to each end of the inner module. The light from the LEDs is focused through a lens mounted on the middle module and falls onto a pair of quadrant photodiodes on the outer chamber. The position of the middle chamber is then adjusted until the three chambers are in a straight line. To ensure that the axis of each chamber is parallel to the beam line, a He-Ne laser is used to generate a reference plane between the halves of the middle and outer chambers. The MO and MM chambers are adjusted so that the deviation of their center lines with the reference plane is zero.

The overall alignment of an octant is verified by using a nitrogen ultraviolet laser to simulate infinite momentum tracks. Each octant contains a laser and directional beam elements that generate eight laser beam trajectories(see Fig. 3.5). The beam passes through all layers of the octant through quartz windows in selected drift cells and is monitored by photodiodes mounted below the MI chambers. This system verified that the sagitta error of straight tracks in each octant is less than 30 μm.

Muon Chamber Resolution

From test beam and cosmic ray data, the single wire resolution for the p-chambers (z-chambers) was determined to be about 150 μm (500 μm). The accuracy of the muon system has been measured from an analysis of $Z \rightarrow \mu^+ \mu^-$ data by comparing the muon momentum with the beam energy. Accounting for radiative corrections, the observed resolution of 45 GeV muons is $\sigma(E_{beam}/p_\mu) = 2.5 \pm 0.4\%$.

3.2.3 Hadron Calorimeter

The energy of hadronic particles is measured by the total-absorption technique with a homogeneous bismuth germanate oxide (BGO) crystal calorimeter and a uranium, gas proportional tube sampling hadron calorimeter (HCAL). The HCAL is constructed of depleted uranium absorber plates interspersed with proportional wire chambers. Uranium was chosen for a number of reason:

- It has a very short nuclear absorption length so the calorimeter can be compact.
- Gamma rays from the spontaneous decay of the uranium can be used to calibrate the wire chambers.
- A free supply was readily available from what was the Soviet Union.

The barrel portion of the calorimeter consists of 9 rings with 16 modules per ring covering the polar angles from 35° to 145° (see Fig. 3.6). Each module has either 53 or 60 planes of wire chambers in the radial direction. The orientation of the wires changes by 90° in alternating planes for better determination of particle trajectories. The wires are grouped together to form 11,664 readout towers. The towers point to the beam axis in the ϕ projection and have constant width in the z direction. The solid angle covered by a single tower is small, typically $\Delta\phi = 2^\circ$ and $\Delta\theta = 2^\circ$. The total thickness of the HCAL is greater than 3 nuclear absorption lengths.

The hadron calorimeter endcaps extend the polar angle coverage down to 5.5°, which represents 99.5% of 4π of solid angle. Each endcap consists of three rings: one outer (HC1) and two inner rings (HC2, HC3). The rings are split vertically in half, and

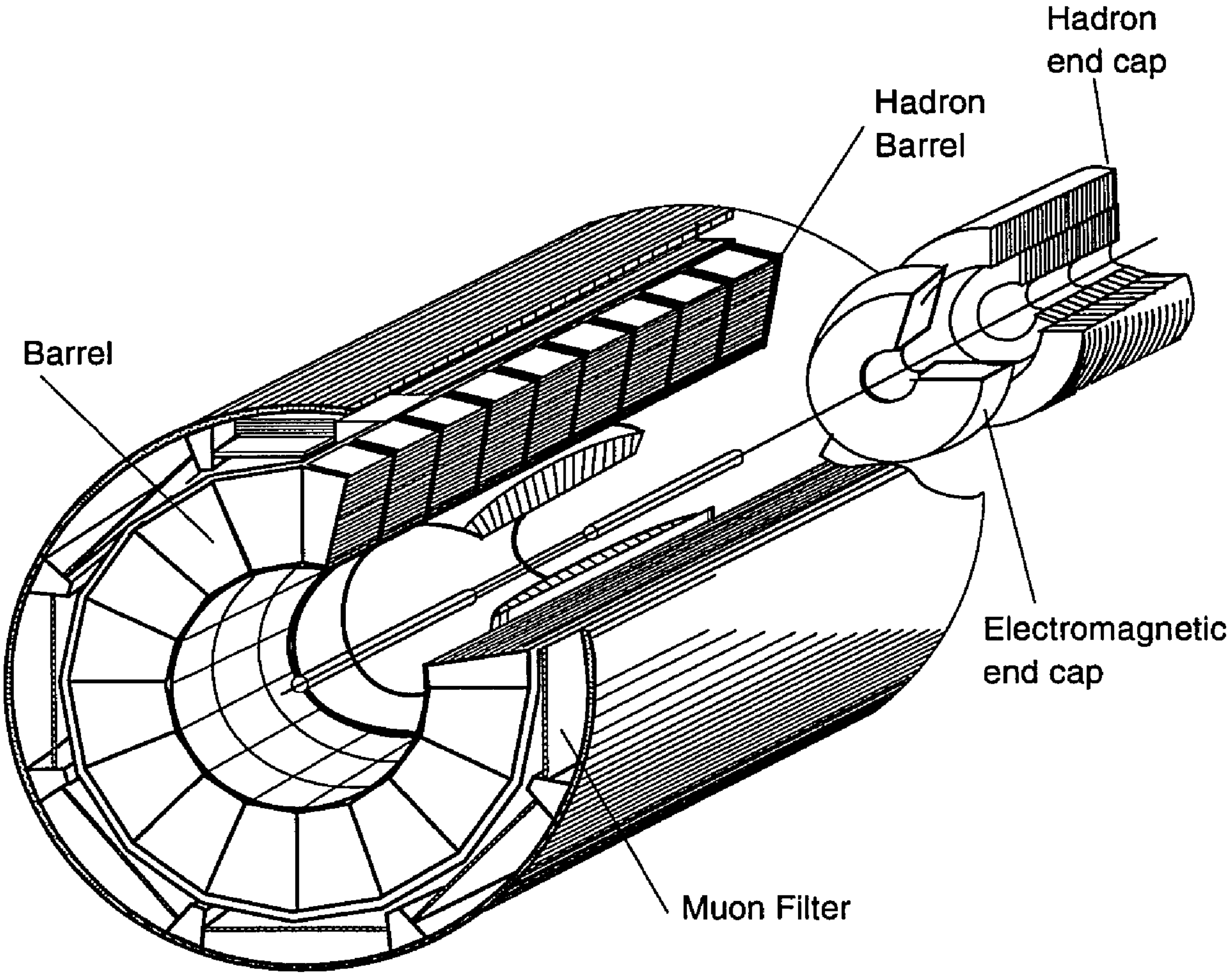

FIG. 3.6: Hadron barrel and endcap calorimeter. Only one endcap is depicted.

once installed, they can be quickly removed to permit access to the remaining central detectors. The wire chamber planes in the endcaps are oriented perpendicularly to the beam line and have a stereo angle of 22.5° between alternating planes. The wires are grouped into 3,960 towers that point toward the interaction region in the R-Z projection. The solid angle segmentation is equivalent to the barrel segmentation. The thickness of the material a particle originating from the center of the detector traverses varies from 6 to 7 nuclear absorption lengths.

The energy resolution of the calorimeter modules was measured in test beams at CERN and the Institute of Theoretical and Experimental Physics (ITEP) in Moscow. The resolution of a completed module is $(55/\sqrt{E}(\mathrm{GeV}) + 5)\%$. The resolution of the total energy of hadronic decays of the Z is better than 10%. The fine segmentation results in the determination of jet axes with an angular resolution of 2.5°.

The HCAL acts as a filter as well as a calorimeter. Most particles deposit all of their energy and stop within the calorimeter. Only muons and neutrinos have a high probability of reaching the muon chambers. A muon filter mounted on the inside wall of the steel support tube adds an additional nuclear absorption length to the interaction length of the inner detector. The filter is composed of brass absorber plates interleaved with gas proportional tubes.

3.2.4 Scintillation Counters

Between the electromagnetic and hadronic calorimeters are 30 plastic scintillator counters that cover the polar angle region between 44° and 146°. The counters are

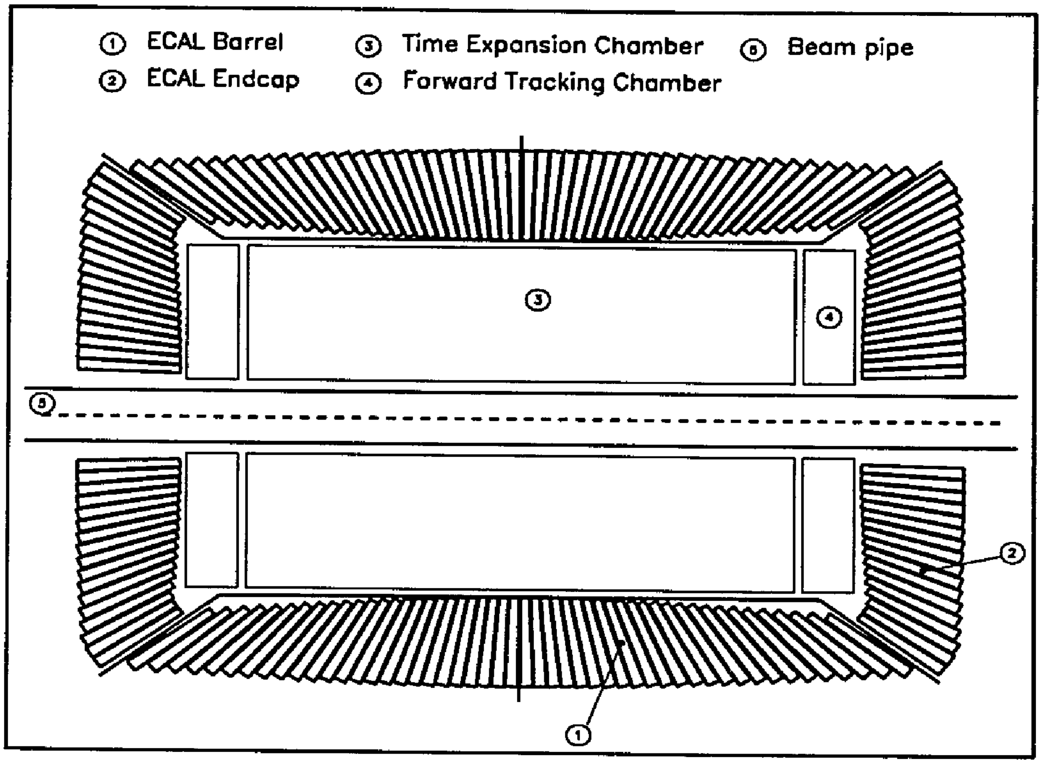

FIG. 3.7: The BGO electromagnetic calorimeter.

used to trigger hadronic events and to reject cosmic ray background. Cosmic rejection is achieved through time-of-flight measurements. The time difference between opposite counters is 6 ns for a cosmic muon which passes through the detector and is zero for a pair of muons that originate from the interaction region. The timing resolution of the counters is 460 ps.

3.2.5 Electromagnetic Calorimeter

Surrounding the central tracking chamber is an electromagnetic calorimeter composed of bismuth germanate crystals (BGO). The calorimeter consists of two half barrels and two endcaps (see Fig. 3.7). The endcaps were split horizontally and then bolted together around the beam pipe. The entire barrel portion of the calorimeter is constructed from 7,680 BGO crystals and covers the polar angles $42° < \theta < 138°$. Each endcap is made of 1,527 BGO crystals that extend the angular coverage down to $\theta = 11.6°$ with respect to the beam line. In front of the endcaps are forward tracking chambers (FTC) that augment the tracking of charged particles in the forward region.

The FTC and BGO endcaps were installed at the beginning of 1991. Prior to that, 8 wedges of scintillator were placed in front of the hadron calorimeter endcaps at each end. Because the cabling for the central tracking chamber and the FTC occupied more space than was planned, it was not possible to fit the endcaps into their designed location. For this reason, a ten centimeter gap exists between the BGO barrel and endcap (the gap is not shown in Fig. 3.7).

BGO Characteristics

The BGO crystals act as both the shower and scintillating material. Each crystal is cut and polished in the shape of a truncated pyramid 24 cm long, about 2×2 cm^2 at the inner face and about 3×3 cm^2 at the outer face. The crystals are arranged to point to the interaction region with a 10 mrad offset to suppress photon leakage along radial lines between crystals. Table 3.1 compares the properties of BGO with another commonly used scintillating crystal, NaI(Tl). The chief advantage of BGO is its high density, comparable to that of steel. The high density and corresponding short radiation length allow the calorimeter to be compact. In addition the lateral spread of electromagnetic showers is small, which results in improved angular resolution.

Table 3.1: Properties of BGO and NaI scintillating crystal.

	BGO	NaI(Tl)
Density (g/cm^3)	7.13	3.67
Radiation Length (cm)	1.12	2.59
Moliere Radius (cm)	2.3	4.4
dE/dx MIP (MeV/cm)	9.0	4.8
Peak Emission (nm)	480	410
Decay Constant (ns)	300	250
Average Light Yield (photons/MeV)	2800	4000
Light Yield Temperature Coefficient (%/°C)	-1.55	0.22

Readout electronics

Two photodiodes that detect the scintillation light are glued to the back of each crystal. The photodiodes are insensitive to magnetic fields, have a quantum efficiency of approximately 70% and do not provide any signal amplification. Preamplifiers are mounted directly behind each crystal and the amplified signal is brought out to analog-to-digital converters (ADC) mounted 3m away, behind the hadron calorimeter endcaps. The ADCs measure the signals from each crystal over a range from 0.1 MeV to 200 GeV with a resolution of at least 1000:1 above 100 MeV.

There are four levels to the ECAL readout system. Except for the first level, the readout system is housed in the counting rooms, which are more than 100 meters away from the detector. The first level, level-1, consists of an ADC controlled by a microcomputer for each crystal. Level-1 digitizes and stores the signals from every crystal within 250 μs of the trigger. Not all of the 10,914 crystals are read out in every event. Since the majority of crystals in a given event do not receive any deposited energy, the crystal is read out only if the signal is greater than a preset threshold in the level-1 microcomputer. The thresholds are set independently for every level-1 channel and can be reprogrammed through the level-2 computers. The level-2 readout consists of a single VME board for every 60 crystals. The data is read out of level-1 with a token passing scheme, whereby each microcomputer transfers its data in turn, on a common data bus, to the level-2 board. The VME crate master, which comprises level-3, directly accesses the memory in the level-2 boards in its crate (there are 16 level-2 boards in a crate) and passes the data, without buffering, to level-4. Level-4 combines all of the data for an event in a First-In-First-Out buffer and sends it to a FASTBUS memory module in the main data acquisition system. The maximum average data transfer rate for the entire ECAL readout is greater than 6 Mbytes/s,

Energy calibration and resolution

The entire barrel portion of the calorimeter and one half endcap were calibrated in the CERN SPS X3 beam to an accuracy of 1%. Over 1000 electrons per crystal were recorded at three energy settings: 2, 10 and 50 GeV. The energy resolution is $\simeq$ 5% at 100 MeV and $\simeq$ 1.4% for energies greater than 2 GeV(see Fig. 3.8). The hadron/electron rejection ratio is about 1000:1 for charged tracks with momentum greater than 2 GeV, and the spatial resolution is better than 2 mm.

The light collection efficiency of the crystals and readout electronics is monitored by a xenon lamp system. Two optical fibers distribute light from calibrated xenon flash lamps to the back face of every crystal. One fiber simulates a high energy signal ($\sim$ 35 GeV) and the other a low energy signal ($\sim$ 1.5 GeV). Combining the xenon

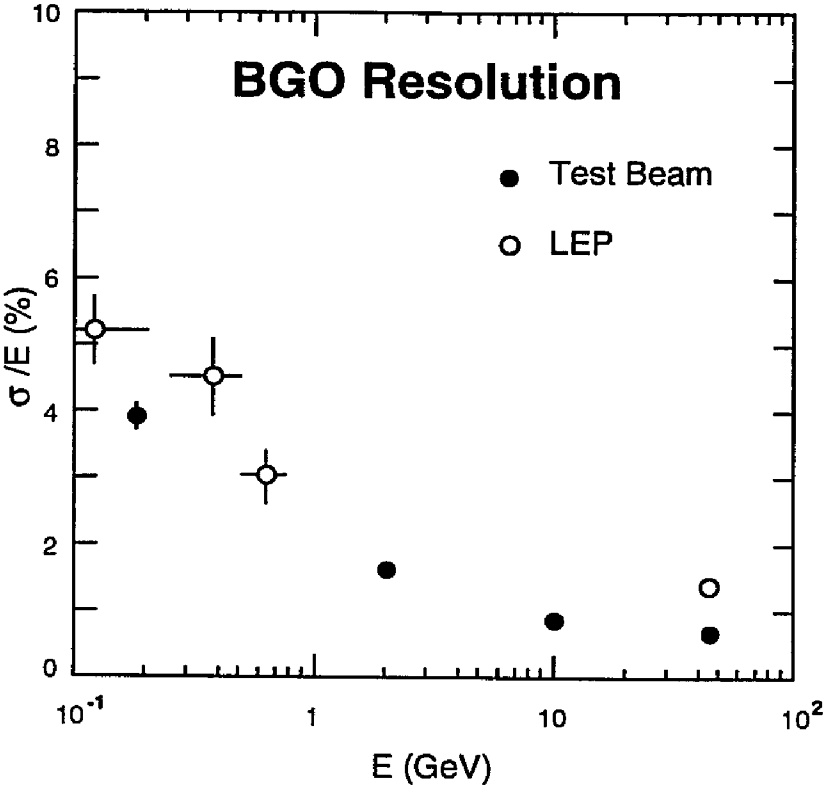

FIG. 3.8: Energy resolution for the barrel BGO calorimeter.

monitor system with Bhabha scattering information, the absolute calibration can be maintained to within 1%.

Since the light output variation of BGO with temperature is $-1.55\%/°C$, the crystal temperature must be held constant to within a few tenths of a degree to maintain the desired energy resolution. To dissipate the heat generated by the preamplifiers, a brass screen with copper pipes was positioned 1 mm behind the electronics. A silicon-based cooling fluid is circulated through the pipes. The cooling fluid is held below atmospheric pressure to prevent leaks. Approximately 1/12 of the crystals have temperature sensors, accurate to 0.1°C, mounted on their front and back face. The sensors readings were periodically stored in a database and were used offline to correct the energy calibration of the calorimeter.

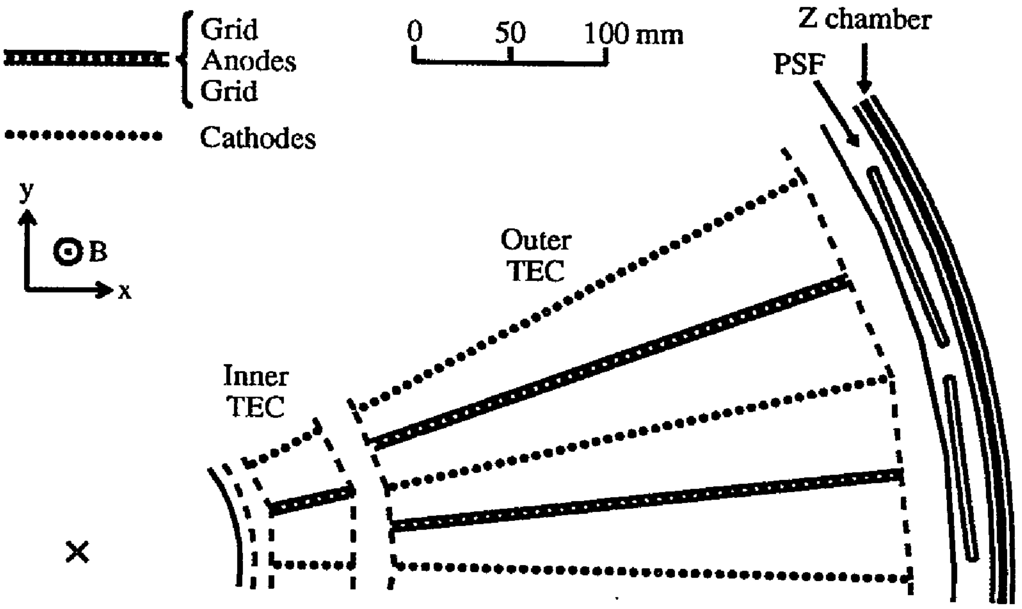

FIG. 3.9: Partial cross-section of the Time Expansion Chamber (TEC).

3.2.6 The Central Tracking Chamber

At the center of the L3 detector is a multi-wire, gas ionization drift chamber (TEC)[1]. The chamber is approximately 1 m in length, 0.5 m in radius and consists of about 10,000 wires strung parallel to the beam axis (see Fig. 3.9). The wires create regions of constant electric field and detect the ionization left by the passage of a charged particle. The field shaping wires are arranged to create an inner and outer region. The outer region is divided into 24 sectors in the R-ϕ plane while the inner region is divided into 12 sectors. Figure 3.10 displays a sample field map for the region around a sector. The voltages on the field wires are set such that the electric field is constant in the drift region of the sector. A grid wire plane separates the low field

---

[1] The acronym TEC stands for Time Expansion Chamber.

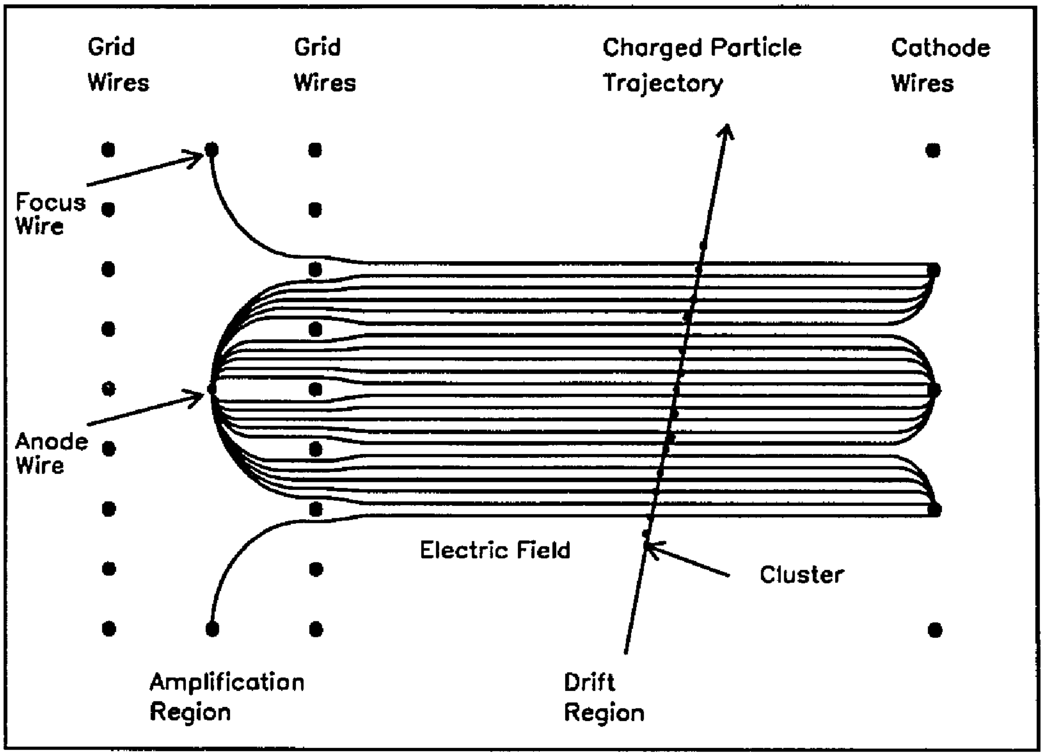

FIG. 3.10: Electric field map of a TEC sector.

drift region from the high field amplification region. A charged particle that passes through the chamber leaves an ionization trail. Electrons from the ionization of the gas drift with constant velocity along the electric field lines. Near the anode wire the increased electric field causes the incoming electrons to accelerate which produces an avalanche of secondary ionization. The ionization gas is a mixture of 80% CO_2 and 20% iC_4H_{10}, and has a low drift velocity of 6 μm/ns. The drift time is proportional to the distance the ionization charge traveled and thus indicates the position of the track relative to the sense wire. After the pulses are shaped, Flash Analog to Digital Converters (FADC) sample the signals from the anode wires.

Tracks are sampled by 62 layers of anode wires with a total lever arm of 0.317 m. The single wire resolution is 50 μm, and the transverse momentum ($p_\perp$) resolution is approximately $\Delta(1/p_\perp)/(1/p_\perp) = (3 + 2p_\perp)\%$, where p_T is measured in GeV.

Each sector has a plastic scintillating fiber ribbon that runs the length of the detector on its outer surface. The fibers monitor the drift velocity to an accuracy of 0.1%. For every anode wire the average drift time is plotted versus the fiber position. The slope of this plot gives the inverse of the drift velocity.

Two cylindrical proportional wire chambers cover the scintillating fiber ribbons. The wire chambers are read out with cathode strips that are inclined by 69° and 90° with respect to the beam direction for the inner chamber and by $-69°$ and 90° for the outer chamber. These chambers give a z-coordinate measurement for tracks that penetrate the outer TEC cylinder.

3.2.7 Luminosity Monitor

A luminosity monitor was placed at 2.65 m from the interaction point on either side of the detector. Each monitor consists of a BGO crystal calorimeter and proportional wire tracking chamber, which cover the polar region between 24.93 mrad and 69.94 mrad. The BGO calorimeters are cylindrical, finely segmented, and composed of 304 crystals each. The readout and calibration of the luminosity monitor is similar to the main electromagnetic calorimeter system. Since the Bhabha cross-section rises steeply as the polar angle approaches the beam pipe, the fiducial volume determination is crucial to the calculation of the luminosity. Tracking chamber information in conjunction with energy profiles of the electron shower in the BGO are used to precisely define the geometrical acceptance. The systematic uncertainty on the luminosity from the geometry measurement is 0.4% and is the largest single contribution to the total systematic error on the luminosity.

Chapter 4

Data

4.1 Introduction

Every attempt was made to record all the e^+e^- annihilation events that occurred at the L3 interaction point. This was possible because the interaction rate was low ($\sim$ 0.5 Hertz at a luminosity of $10^{31}\mathrm{cm}^{-2}\mathrm{s}^{-1}$) and the background was minimal. A fast trigger decided if an e^+e^- interaction had occurred and initiated the digitization of the state of the detector. The raw digitized data were recorded on tape and sent to an offline computer system for reconstruction. The reconstructed data contained information about the tracks of charged particles and clusters of energy deposited in the calorimeters. The tracks and clusters were used to identify constituents of the event, such as jets and individual particles, and to classify the event as a whole. A sample of events which were the result of the decay of a pair of primary quarks was selected and separated for this analysis. From this sample, events that contained leptons were used to determine the B^0-$\bar{B}^0$ mixing parameter and the $b\bar{b}$ forward-backward asymmetry.

4.2 Simulated Data

Computer simulated events played an important part in determining the response of the detector and extracting the physics results. For example, the calculation of the background composition of the data sample as a function of the lepton momentum spectrum relied completely on simulated data.

The simulation process can be divided into two logical steps. In the first step, the initial configuration of particles based on a particular physical model is generated. The output of this initial step is a list of particles (which are not necessarily stable) with their associated energy-momentum four vectors. In the second step, the original particles are propagated through a detailed representation of the detector. Their interaction with each element of the detector is simulated and digitized output representing the detector response is produced.

The format of the output of the simulation is compatible with that of the raw data and the same computer programs were used to analyze both real and simulated events. Information about the original configuration generated by the simulation was also stored with each event, making it possible to investigate the detector response to a given particle in each event.

The quantum mechanical effects in the production of the initial configuration and the subsequent interaction of the particles with the detector requires a probabilistic approach to the simulation. This approach is readily implemented by Monte Carlo computer programs. The Monte Carlo method is defined as any technique that uses a sequence of random numbers to construct a sample population to solve a problem. In addition to reproducing the average behavior of the data, the Monte Carlo method will produce results that have the same degree of fluctuations on an event-by-event basis as the data.

4.2.1 The Event Generators

To simulate the various possible processes involved in e^+e^- annihilation, a number of different Monte Carlo generator programs were used. For quark-pair final states JETSET 7.3 [44] was used. Many results were cross checked with HERWIG 5.3 [64], which implements a different fragmentation scheme. KORALZ [65] was used to simulate $\mu^+\mu^-$ and $\tau^+\tau^-$ final states. Bhabha scattering was simulated with BABAMC [66, 67] for wide angle scattering and BHLUMI v2.01 [68, 69] for calculating the acceptance of the luminosity monitor.

4.2.2 The L3 Detector Simulation

The simulation of the L3 detector is based on GEANT3 [70], which is a general purpose program that simulates the response of a user-defined detector for a given input particle configuration. A complete representation of the geometry of the L3 detector of both active (chamber and calorimeter) and passive (support structure and beam pipe) materials has been defined within the program. Typically, the level of accuracy of this description is 10-100 μm, and it incorporates survey information of the actual detector.

Particles are tracked through the detector in small discrete steps, simulating the possible interactions at each step such as energy loss, multiple scattering, decay, bremsstrahlung, pair production, and nuclear interactions. Electromagnetic and hadronic showers are simulated in this way and particles are tracked down to the sensitivity limits of the detector ($\sim$ 10 KeV in the ECAL and $\sim$ 1 MeV in the HCAL).

Hits in the muon and central tracking chambers were simulated using the drift distance to time relation measured from test beam data. The simulation also includes the effects of cross talk, multiple hits and δ-rays.

4.2.3 The Monte Carlo Data Sample

The approximate number of Monte Carlo events used in this analysis for the different type of events are listed in Table 4.1. The one million $q\bar{q}$ events generated by JETSET include all five quark pairs (u, d, s, c, b), whereas the $b\bar{b}$ data contains events in which one of the b quarks was forced to decay semileptonically to a muon or an electron.

Table 4.1: Approximate number of Monte Carlo events for the different final state fermion pairs used in this analysis. The final state $q\bar{q}$ includes all five quark pairs (u, d, s, c, b). In the pure $b\bar{b}$ sample, at least one of the b quarks in the event was forced to decay to an electron or muon.

program	final state	Number of Events
JETSET 7.3	$q\bar{q}$	1,000,000
JETSET 7.3	$b\bar{b}$	200,000
KORALZ	$\tau^+\tau^-$	80,000
BABAMC	e^+e^-	60,000
KORALZ	$\mu^+\mu^-$	40,000

4.3 Trigger

The on-line trigger uses coarse-grained information from the detector to make a fast decision about whether an e^+e^-annihilation event has occurred. A decision is made before the arrival of the next beam crossing (22 μs) so that negative decisions do not contribute to the dead time. For a positive decision, the complete event is digitized and stored in about 500 μs. Under normal running conditions data are collected with a dead time of 5% [62].

An event is recorded if it satisfies at least one of the following triggers [71]:

1. Energy Trigger. Any of:
    a. 10 GeV in the barrel and endcap ECAL.
    b. 15 GeV in the barrel calorimeters (ECAL and HCAL).
    c. 20 GeV in the barrel and endcap calorimeters (ECAL and HCAL).
2. Dimuon Trigger. At least two tracks in non-adjacent octants in the muon chamber and at least one scintillator counter hit.
3. Single Muon Trigger. At least one track with transverse momentum ($p_\perp$) greater than 1.5 GeVand one scintillator hit.
4. Charge Track Trigger. At least two tracks in the TEC with $p_\perp$ greater than 150 MeV and angular separation greater than 120° in the transverse plane.
5. Scintillation Counter Trigger. At least five out of 30 barrel scintillator counters fire within 13 ns of beam gate and at least one pair of counters hit is separated by more than 45° in azimuth.

The combined trigger efficiency for hadronic events is greater than 99.9% [72]. Since the triggers listed above are largely independent, they have been used to cross-check the single trigger efficiency of each other.

4.4 Hadronic Event Selection

The data sample selected by the trigger consisted of hadronic and leptonic e^+e^- events as well as background that did not originate in e^+e^- interactions. In order to eliminate the non-hadronic events, additional selection criteria were applied to the fully reconstructed data. The additional cuts are summarized in Table 4.2.

Since the electron and positron beams have equal energy and opposite momenta, the detector frame of reference corresponds to the center-of-momentum frame of the e^+e^- interaction. The net momentum of the final state particles is therefore zero and the total energy is equal to twice the beam energy. Events that do not originate from e^+e^- annihilation, for example cosmic ray events and beam interactions with the wall of the vacuum vessel or with residual gas in the beam pipe, in general do not meet these energy-momentum requirements. Background events are thus eliminated by cutting on the total energy deposited in the detector (E_{vis}) and the transverse and longitudinal energy imbalance ($E_\perp, E_\parallel$). The cuts cannot be made too restrictive since neutrinos produced in the weak decay of the final state particles and energy radiated along the beam pipe will not be detected. Furthermore, the finite detector resolution limits the precision with which the energy can be measured.

Table 4.2: Hadronic event selection cuts.

$0.5 < E_{vis}/\sqrt{s} < 1.5$
$E_\parallel/E_{vis} < 0.5$ $E_\perp/E_{vis} < 0.5$
$N_{\text{cluster}} \geq 14 \quad (\lvert\cos\theta\rvert < 0.74)$ $N_{\text{cluster}} \geq 18 \quad (\lvert\cos\theta\rvert > 0.74)$

Leptonic events ($e^+e^- \rightarrow e^+e^-$, $\mu^+\mu^-$, $\tau^+\tau^-$) and cosmic ray showers result in low particle multiplicities compared to hadronic events. The cut on the number of energy clusters in the calorimeters (N_{cluster}) eliminates nearly all such events. The value of the cut is different in the endcap region ($|\cos\theta| < 0.74$) because the segmentation of the calorimeters is different in the barrel and endcap regions.

Monte Carlo-simulated events were used to determine the efficiency of these cuts and the amount of background present in the selected sample. From studies of events generated with JETSET and HERWIG, the acceptance for $e^+e^- \rightarrow$hadrons was determined to be 99.04 ±0.03 (stat) ±0.20 (syst)%. Simulations of $e^+e^- \rightarrow \tau^+\tau^-$ events with KORALZ indicated a contaminating background of 0.10 ± 0.02% from these events [71].

4.5 Electron Identification

The identification of electrons proceeds in two steps. High quality charged tracks reconstructed in the TEC are extrapolated to the front face of the ECAL and matched with energy clusters in the R-ϕ projection. The angle $\Delta\phi$ between the point at which the track enters the ECAL and the energy-weighted center-of-gravity of the ECAL cluster in the R-ϕ plane is calculated for all track cluster pairs. Matched pairs with a $\Delta\phi$ of less than 15 mrad are selected as electron candidates. In the second step, additional cuts that select electromagnetic showers are applied to these candidates. To make a precise match, the relative position of the various subdetectors and the geometry of the ECAL must be taken into account.

4.5.1 TEC Alignment

Each subdetector uses a local coordinate system. Tracks are parameterized with respect to the TEC and cluster positions are defined with respect to the ECAL. The relative position and orientation of the TEC to the ECAL is required to calculate a precise match. Engineering surveys of the detector elements can achieve a precision of no better than 0.3 mm and are susceptible to large systematic errors, so an independent method must be used. [1]

A precise determination of the relative alignment between the ECAL and TEC is possible by analyzing large angle Bhabha events. Bhabha events have a very clear signature: a pair of stiff tracks and a pair of ECAL clusters. Since the tracks can be unambiguously matched with the corresponding cluster, the $\Delta\phi$ distribution as a function of ϕ, the azimuthal angle of the TEC track, can be used to determine the relative positions of the two coordinate systems. The details of the $\Delta\phi$ distribution are derived below.

Let us assume that the TEC and ECAL coordinate systems are offset by (x, y) and rotated by α with respect to each other in the R-ϕ plane (see Fig. 4.1). In the figure, the solid axis depicts the coordinates of the ECAL barrel, and the dotted axis represents the TEC coordinate system which is arbitrarily displaced and rotated. Straight tracks coming from the TEC origin can be parameterized by a single angle ϕ. Making the mistaken assumption that the ECAL and TEC coordinate systems

---

[1] A survey of the beam elements at the L3 interaction region failed to indicate an error of 5 cm in the position of one of the magnets. The magnet had moved inside its case and since the survey was based on the case the error went undetected for over a year.

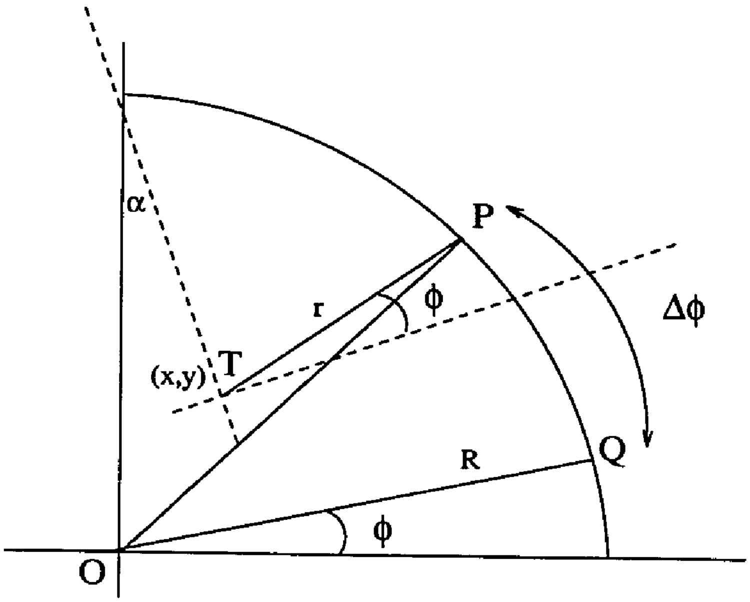

FIG. 4.1: TEC coordinate system (dotted axis) displaced and rotated with respect to the ECAL coordinate system (solid axis).

are the same, the track would intersect with the ECAL barrel at point Q. In the true TEC coordinate system, the track intersects the barrel at point P. The opening angle between points P and Q defines $\Delta\phi$. At point P, the following trigonometric relations hold

$$R\cos(\phi + \Delta\phi) = x + r\cos(\alpha + \phi)$$

$$R\sin(\phi + \Delta\phi) = y + r\sin(\alpha + \phi).$$

The triangle defined by points P,O,T gives:

$$R^2 = r^2 + x^2 + y^2 + 2r(x\cos(\alpha + \phi) + y\sin(\alpha + \phi).$$

Combining these equations and keeping terms up to first order in $\frac{x}{R}$, $\frac{y}{R}$, and α yields:

$$\sin \Delta\phi = -\frac{x}{R} \sin \phi + \frac{y}{R} \cos \phi + \sin \alpha.$$

For small displacements and rotations, $\frac{x}{R}$, $\frac{y}{R} << 1$ and $\alpha << 1$, this reduces to:

$$\Delta\phi = -\frac{x}{R} \sin \phi + \frac{y}{R} \cos \phi + \alpha. \tag{4.1}$$

This simple relation between $\Delta\phi$ and ϕ can be used to extract x, y and α from the data.

The mean $\Delta\phi$ calculated from Bhabha tracks in the half barrel $\cos\theta < 0$ as a function of ϕ is compared to the Monte Carlo prediction in Fig. 4.2. The data are fit to Eq. (4.1) with $\frac{x}{R}$, $\frac{y}{R}$, and α as free parameters. Note that in the Monte Carlo, the mean $\Delta\phi$ is ~ -2 mrad. This is due to the tilt of the BGO crystals with respect to the radial unit vector. The next section will elaborate on this effect and how it can be corrected.

The offsets x and y are extracted from the fit by multiplying the fit parameters $\frac{x}{R}$ and $\frac{y}{R}$ by the mean radius R. The expected $\Delta\phi$ offset from the Monte Carlo is subtracted from the α determined from the fit. This parameter is defined to be

$$\alpha' = \alpha_{\text{DATA}} - \alpha_{\text{MC}},$$

which represents the rotation needed to bring the real data into agreement with the

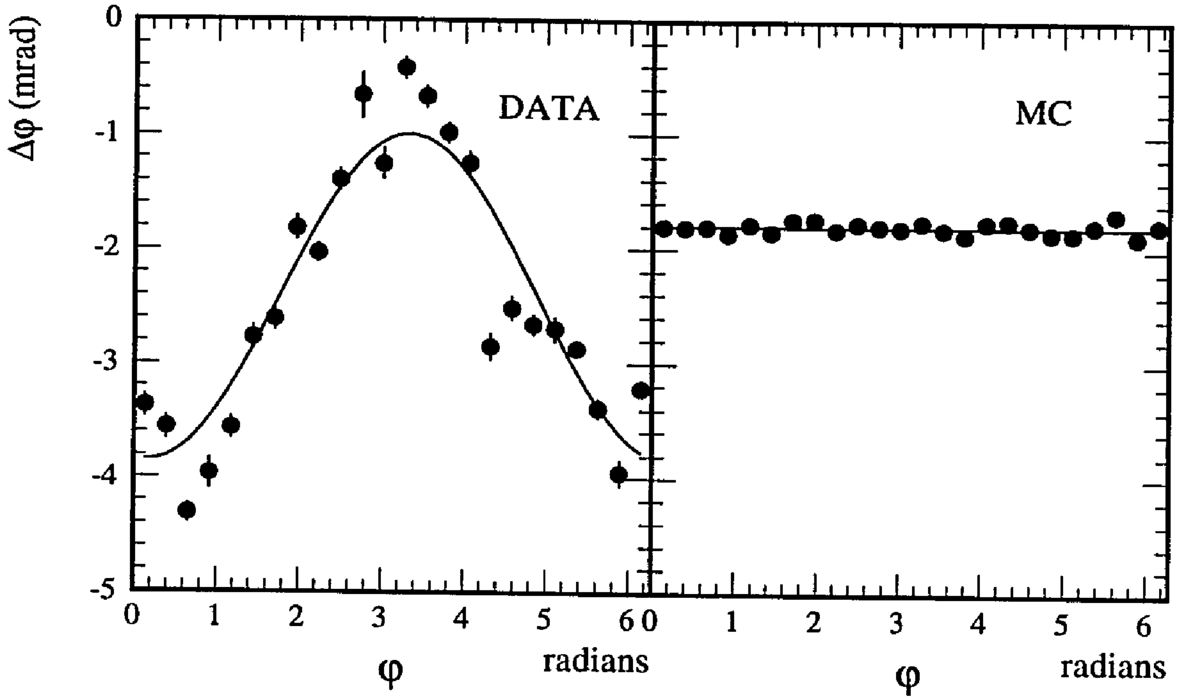

FIG. 4.2: Mean $\Delta\phi$ from Bhabha events in the half barrel ($\cos\theta < 0$).

Monte Carlo.

Figure 4.3 displays the $\Delta\phi$ distribution from Bhabha data collected in 1991 for all six segments of the BGO calorimeter (the barrel is constructed from two half barrels and each endcap is split horizontally into two pieces). The offsets for each ECAL segment are listed in Table 4.3. The offsets determined for 1990 and 1991 data differ for two reasons:

1. The BGO endcaps were not installed for the 1990 run.
2. The TEC was removed and reinstalled after the 1990 run.

In the analysis of inclusive electrons in hadronic events, these offsets are added to the parameterization of the tracks measured with the TEC, so that the calculated $\Delta\phi$ is the true angle in the local frame of the ECAL segment.

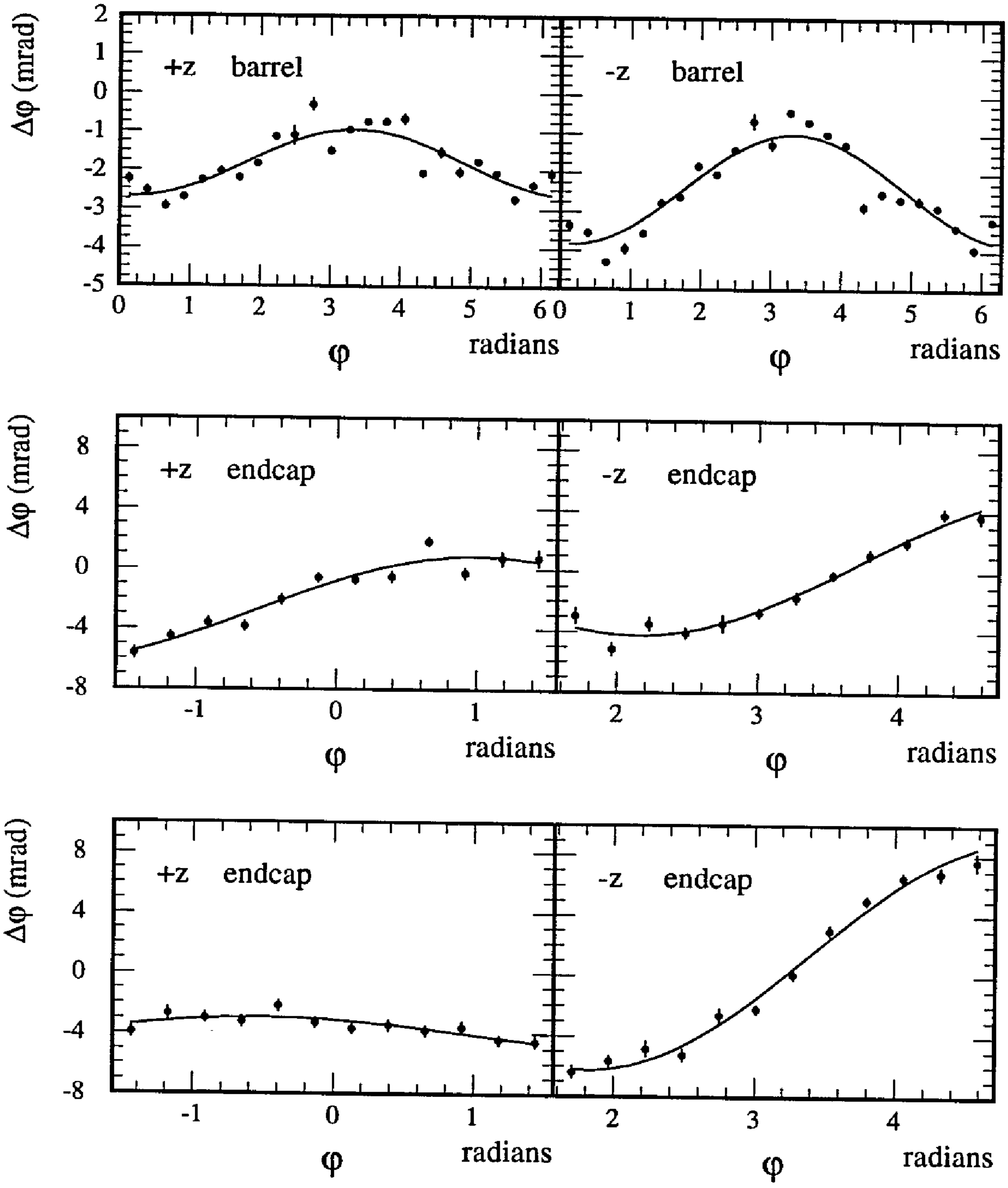

FIG. 4.3: The $\Delta\phi$ distribution calculated from 1991 Bhabha data for each ECAL segment.

Table 4.3: Offset of TEC with respect to ECAL segments. Plus and minus z refers to polar angles $\cos\theta > 0$ and $\cos\theta < 0$ respectively. Top and bottom refer to the separate halves of each endcap.

year	ECAL segment	x (mm)	y (mm)	α' (mrad)
1990	barrel $+z$	2.26	-0.21	0.85
	barrel $-z$	2.10	-0.24	0.23
1991	barrel $+z$	0.10	-0.45	-0.04
	barrel $-z$	0.14	-0.74	-0.63
	endcap $+z$ top	-1.03	0.69	-1.03
	endcap $+z$ bottom	1.41	0.93	2.55
	endcap $-z$ top	0.21	0.37	-2.27
	endcap $-z$ bottom	2.62	0.67	3.40

4.5.2 BGO Crystal Tilt

As was observed in the previous section, the center-of-gravity of the ECAL cluster does not exactly coincide with the point at which the electron enters the calorimeter. In general, the trajectory of the electron is not parallel to the axis of the crystals but instead crosses at an angle resulting in a shift of the center-of-gravity. In order to devise a correction for this effect, it is necessary to look in more detail at the geometry of the BGO and the electromagnetic shower process.

The coordinates of an ECAL cluster are determined from an energy-weighted average of the crystal positions, in spherical coordinates, of a 5×5 array centered on the highest energy crystal in the cluster. Interpreting the ϕ coordinate of a cluster is complicated by the fact that the BGO crystals do not point directly at the interaction vertex but are tilted by 10 mrad (see Fig. 4.4). The purpose of the tilt is to suppress photon leakage between the crystals. Since the beam spot is extremely small in the transverse plane ($\sigma_x = 200\ \mu\text{m}, \sigma_y = 25\ \mu\text{m}$), photons from the primary vertex will

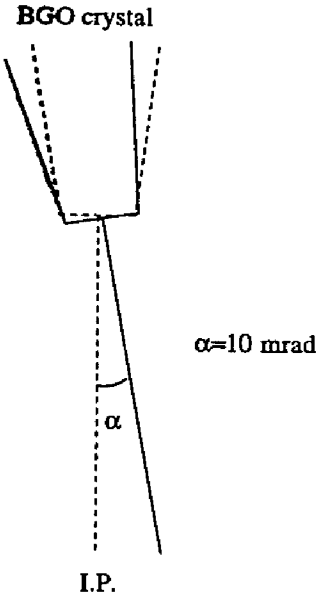

FIG. 4.4: BGO crystal orientation in the R-ϕ plane.

travel along radial lines from the center of the detector. The crystals are rotated so that these photons cannot escape through gaps between the crystals. The effect of this tilt on the reconstructed position of an observed energy cluster depends on the shape of the electromagnetic shower.

When a high energy electron enters the BGO, it initiates an electromagnetic shower of bremsstrahlung photons and electron-positron pairs. The behavior of such showers has been extensively studied and can be accurately simulated [73]. For example, the energy deposited per unit radiation length is shown in Fig. 4.5 from a simulation, using the EGS4 [74] Monte Carlo program, of a 30 GeV electron incident on an iron block. The longitudinal profile of the shower can be approximated by:

$$\frac{dE}{dt} = E_0 b \frac{(bt)^{a-1} \exp -bt}{\Gamma(a)}, \quad t = x/X_0,$$

where E_0 is the initial energy, x is the penetration depth, X_0 is the characteristic

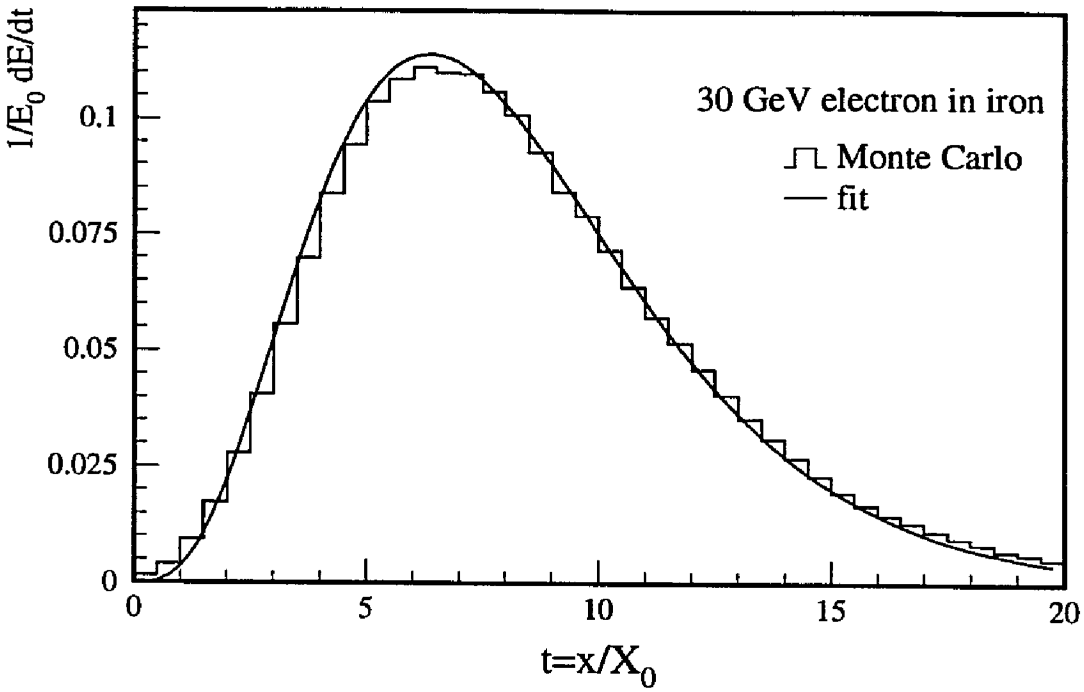

FIG. 4.5: Simulation, using EGS4, of the energy deposited by a 30 GeV electron incident on iron. The fit uses the parameterization of the shower given in the text.

radiation length of the material, $\Gamma(a)$ is the gamma function $= \int_0^\infty u^{a-1}e^{-u}du$, and a and b are free parameters. The peak of this distribution occurs at a depth $t_{\max}$ which is related to E_c, the critical energy of the showering material, by

$$t_{\max} = \frac{a-1}{b} = \ln\left(E_0/E_c\right) - 0.5.$$

The energy-weighted mean penetration depth, $\langle x\rangle$, is the center-of-gravity of the shower in the direction of the particle trajectory

$$\langle x\rangle = X_0(t_{\max} + 1/b) = X_0 \ln E_0 + B, \tag{4.2}$$

where $B = X_0(1/b - 0.5 - \ln E_c)$ and the units for E_c and E_0 must be the same.

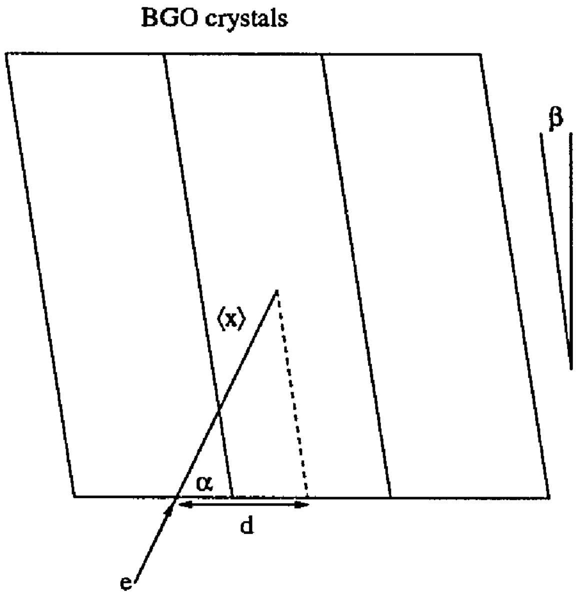

FIG. 4.6: Straight track penetrating tilted BGO crystal array.

The center-of-gravity of the shower calculated from the crystal positions determines the projection of $\langle x \rangle$ onto the front face of the crystals. The relationship between the mean penetration depth and the center-of-gravity is depicted schematically in Fig. 4.6. The distance from the point at which the track enters the BGO and the center-of-gravity measurement is

$$d = \langle x \rangle \cos(\alpha - \beta). \tag{4.3}$$

This connection between $\langle x \rangle$ and d can be clearly illustrated with Monte Carlo events in the L3 simulation. From a sample of electrons in the Monte Carlo, d and α were measured from the known track trajectory and the reconstructed cluster position. Assuming a value for β, $\langle x \rangle$ was calculated from the measured d and α and is plotted in Fig. 4.7 as a function of the log of the electron energy. For $\beta = 10$ mrad, $\langle x \rangle$ is linearly related to $\ln(E)$ as expected from Eq. (4.2). Neglecting to include the crystal

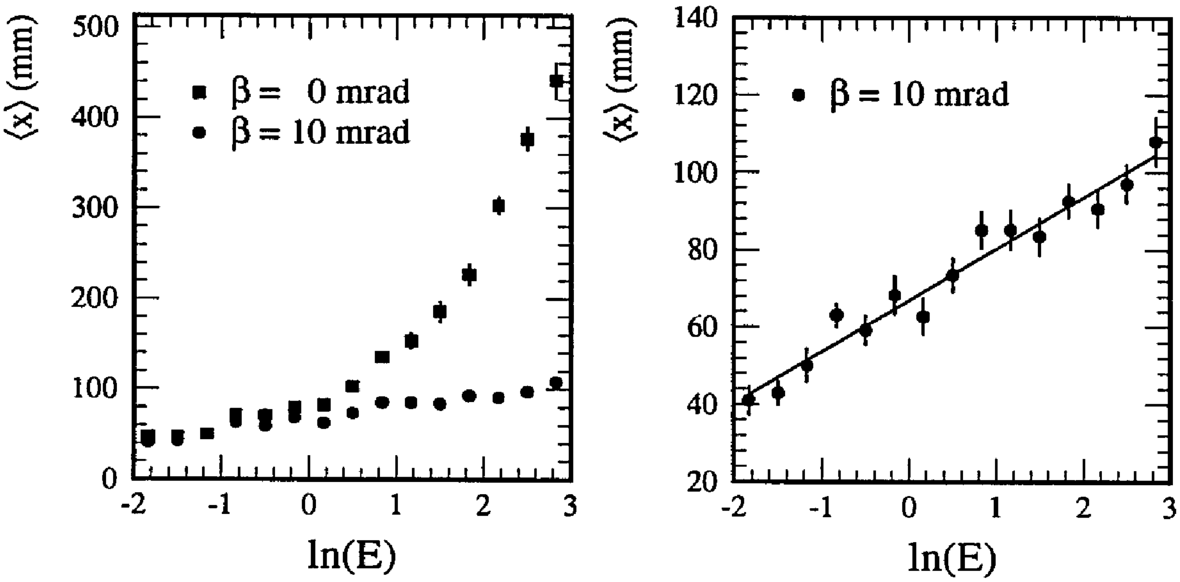

FIG. 4.7: Calculated penetration depth for electrons in Monte Carlo events. The energy, E, is given in units of GeV.

tilt, i.e. assuming $\beta = 0$ mrad, results in a large discrepancy at high energy.

Test beam data would be ideal for observing this effect, but the point at which the track enters the BGO was not precisely measured in the test beam. The wire chambers placed in front of the BGO crystals in the test beam had a resolution of only about 1 mm, which is comparable to the size of the displacement d that must be measured. Furthermore, the mechanical table used to position the BGO array did not have an absolute position calibration.

The parameters X_0 and B determined from a straight line fit to the measured distribution in Fig. 4.7 with $\beta = 10$ mrad are compared to the parameter values determined from the characteristics of BGO in Table 4.4. For BGO, $X_0 = 11.2$ mm, $E_c = 22$ MeV, and $b \sim 0.5$, where the critical energy E_c was determined from a weighted average of the critical energies of bismuth, germanium and oxygen. The agreement between the fit and predicted BGO parameters is really just a check on

Table 4.4: Parameters of shower depth.

	X_0 (mm)	B (mm)
from fit	12.8 ±.8	66 ±1
from BGO	11.2	58

the shower simulation in the Monte Carlo. In the analysis of electrons in hadronic events, the angle between the cluster and extrapolated TEC track ($\Delta\phi$) is corrected using Eqs. (4.2) and (4.3) and the fit parameters from Table 4.4.

4.5.3 Selection

Electron identification begins with the matching of TEC tracks with ECAL clusters. To reach the barrel portion of the calorimeter, charged particles must pass through the outer cylindrical surface of the TEC chamber. Likewise, charged particles must pass through the TEC end flange to reach the calorimeter endcaps. The outermost wire with a hit attached to a TEC track indicates approximately the point at which the track left the chamber. Wire 58 (there are 64 sense wires in the radial direction) would be the last wire on a track that passed midway between the barrel and endcap calorimeters. Therefore, tracks with a hit on wire 58 or greater are matched only with barrel clusters and all other tracks are matched only with endcap clusters.

The selection criteria applied to the matched tracks are summarized in Table 4.5. The cuts that use only ECAL or TEC information are grouped together. The third category of cuts combines information from more than one subdetector. In some cases, the value of the cut is different for endcap and barrel clusters.

Table 4.5: Cuts used for electron selection.

	Cut	Barrel	Endcap
ECAL	$\mathrm{N}_{\mathrm{crystals}}$	> 5	> 5
	$\lvert\cos\theta\rvert_{\mathrm{cluster}}$	$< .69$	0.84-0.97
	E_9/E_{25}	$> .95$	$> .95$
	E	3-30 GeV	3-30 GeV
TEC	Outer Wire	≥ 58	< 58
	hits/span	> 0.7	> 0.7
	DCA	< 5 mm	< 5 mm
	$\Delta\phi_{grid/cathode}$	> 10 mrad	> 10 mrad
	$\Delta\phi_{match}$	< 5 mrad	< 10 mrad
	E/p	< 1.5	< 2.0
	$\mathrm{E}_{\mathrm{cone}}$	< 3 GeV	< 3 GeV
	$\Delta\phi_{\mathrm{nearest}}$	> 10 mrad	> 20 mrad

ECAL cuts

Noise in the photodiode and amplification system of the crystal readout can result in false energy signals. The noise is correlated between only a few crystals and a typical electromagnetic shower results in energy deposition in many crystals. A cut on the minimum number of crystals ($\mathrm{N}_{\mathrm{crystals}}$) eliminates false clusters formed around noisy crystals.

If a cluster falls too close to the edge of the calorimeter, much of the shower will not be detected. A cut on the polar angle ($\lvert\cos\theta\rvert_{\mathrm{cluster}}$) of the cluster is made to ensure that the shower is contained well within the fiducial volume of the calorimeter.

The ratio E_9/E_{25} is a measure of the transverse shape of the electromagnetic shower. It is defined as the ratio of the energy deposited in a 3×3 array of crystals to the energy in a 5×5 array centered on the highest energy crystal of the cluster (see Fig. 4.8). From test beam and simulated data it is known that this ratio can be used

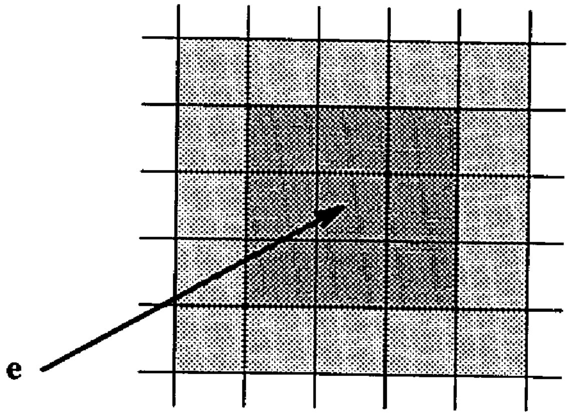

FIG. 4.8: Definition of E_9/E_{25}.

to separate electron from pion showers. In multi-hadronic events the power of this method is reduced due to the overlap of showers from nearby particles. Figure 4.9 shows the average E_9/E_{25} for electrons and pions as a function of the angle to the nearest cluster, from Monte Carlo events. When the cluster is relatively isolated, E_9/E_{25} is effective for separating electrons from pions. Conversely, a cut in E_9/E_{25} implies a minimum amount of isolation.

There are many sources of low energy electrons (for example, the cascade decay $\pi \rightarrow \mu \rightarrow e$, the Dalitz decay $\pi^0 \rightarrow e^+e^-\gamma$ and kaon decays), but electrons from b decays can have very high energies due to the large mass and hard fragmentation of the b quark. Thus a minimum energy cut on the ECAL cluster (E) eliminates much of the background. The electron energy from b decays is bounded from above, so a maximum energy cut is also imposed. The maximum energy of the electron in the rest frame of the b hadron is about 2.3 GeV(see Section 2.4). The maximum boost occurs when the b hadron receives all of the beam energy, which gives a boost of about 9. The maximum energy of the electron in the lab frame is therefore $\sim$ 21 GeV. The

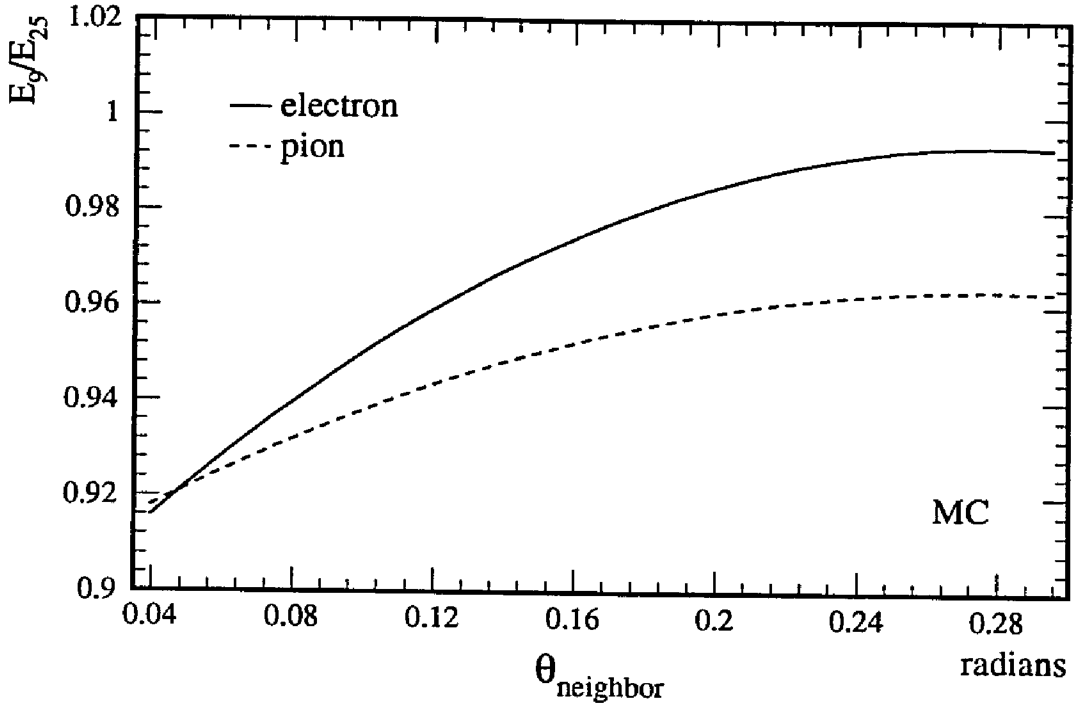

FIG. 4.9: Average E_9/E_{25} as a function of the angle to the next nearest cluster from simulated events.

cut is chosen at a higher energy to account for detector resolution and the effect of overlapping showers.

TEC cuts

The TEC cuts are employed to select tracks that have been reliably reconstructed and originate in the vicinity of the interaction vertex. The ratio hits/span is the the number of TEC wires on the track that had hits divided by the number of wires between the innermost hit and the outermost hit with respect to the center of the detector. Ideally, the ratio is one; however, hits can be lost due to single wire inefficiencies or reconstruction errors in assigning hits to tracks. The majority of tracks have a hits/span ratio of greater than 0.9.

The cut on the distance of closest approach (DCA) to the interaction region eliminates tracks that do not come from the neighborhood of the interaction region. The mean decay length of a b hadron at LEP energies is approximately 2 mm. The 5 mm DCA cut, therefore, accepts practically all b decays but rejects cosmic ray tracks, tracks from photon conversions in the beam pipe and other tracks that do not originate from the interaction vertex.

The single wire resolution deteriorates for tracks that pass near the anode or cathode wire plane since the drift field no longer remains uniform in this region [75]. This leads to a significant degradation in the precision of the transverse momentum measurement. These tracks are discarded by making a cut on the angle between the track and the wire plane ($\Delta\phi_{grid/cathode}$).

Other cuts

A major source of background comes from charged tracks that overlap with high energy photons or π^0's. Precise track-cluster matching can distinguish between these false candidates and energetic electrons. The quantity $\Delta\phi$, the angle between the point at which the track enters the ECAL and the energy-weighted center of gravity of the ECAL cluster in the R-ϕ plane, is corrected for the effect of the finite penetration depth of the electron shower and the BGO crystal tilt. Since the correction is only valid for electron showers, the resolution of $\Delta\phi$ for electrons is improved.

Electrons in the energy range selected for this analysis are highly relativistic. Since most electrons deposit all of their energy in the ECAL, the transverse energy of the cluster ($E_\perp = E \sin\theta_{\text{cluster}}$) should be equal to the transverse momentum of the track measured by the TEC ($p_\perp$). Making a cut on the ratio $E_\perp/p_\perp$ can eliminate matches of tracks and clusters not resulting from an electron.

The electromagnetic calorimeter is approximately 25 radiation lengths thick, so electromagnetic showers rarely penetrate the entire calorimeter. Because of their higher mass, pions do not radiate as many bremsstrahlung photons in the BGO as do electrons and have a higher probability of reaching the hadron calorimeter. Therefore, the energy in the hadron calorimeter behind the ECAL cluster can indicate if the cluster was due to a hadronic particle. The energy behind the ECAL cluster ($\mathrm{E_{cone}}$) is defined as the energy in the hadron calorimeter in a 7° cone behind the cluster.

The energy in the ECAL cluster is not a good estimate of the electron energy when a neighboring shower overlaps it. Overlap from charged tracks is reduced by making a cut on the angular separation in the R-ϕ projection ($\Delta\phi_{\mathrm{nearest}}$) of the nearest track extrapolated to the surface of the calorimeter.

Figures 4.10 and 4.11 show the comparison of data with Monte Carlo for the major cuts that select electrons. Each histogram is made by requiring all cuts except the one that is plotted. The data and Monte Carlo are normalized to the total number of events and the signal from the semileptonic decay of the b is indicated in each plot. The barrel and endcap distributions are plotted separately. The cuts on the total cluster energy and the transverse shower shape (E_9/E_{25}) are responsible for most of the loss of b decay signal.

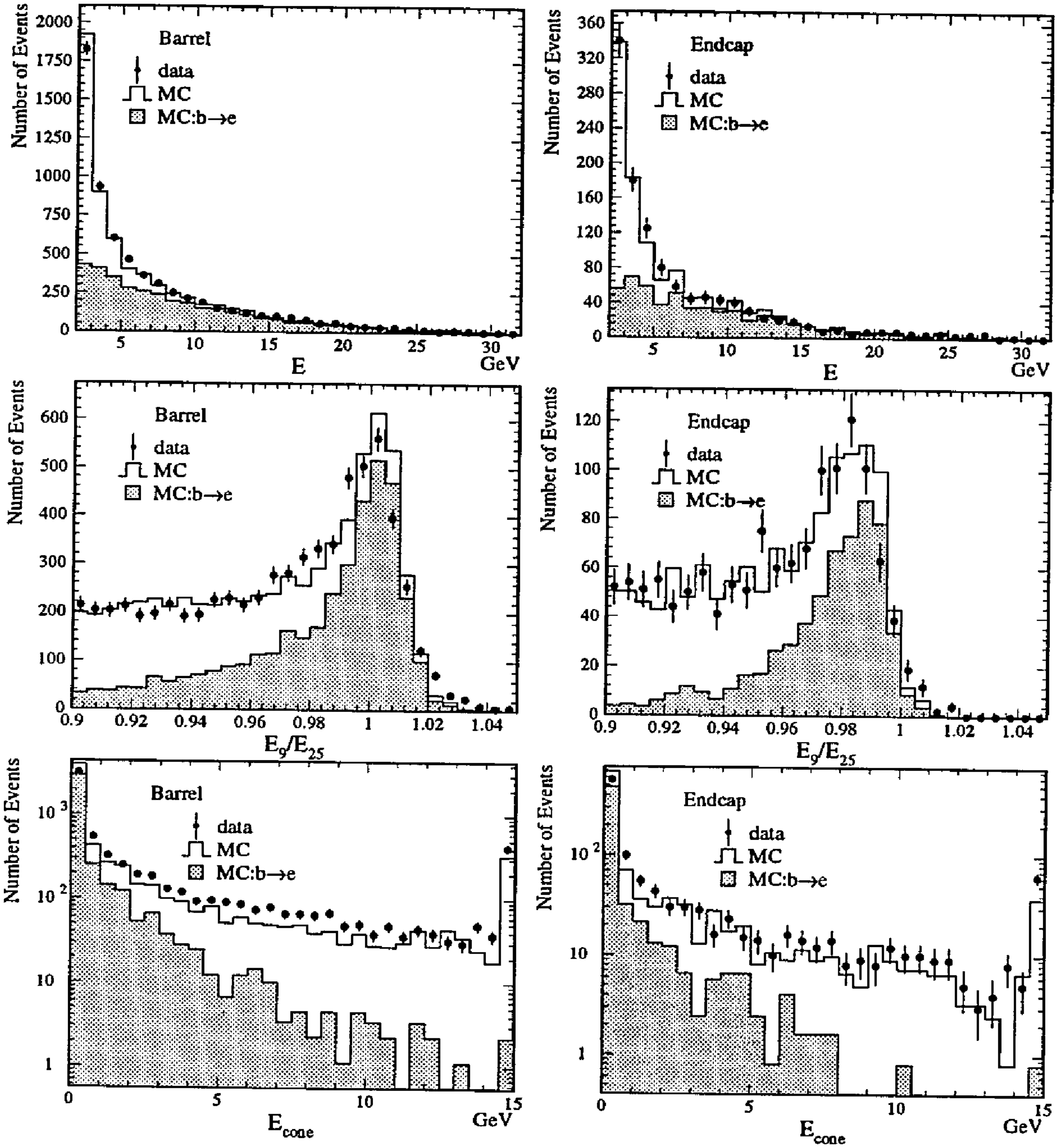

FIG. 4.10: Cut variables used to select electrons from matched TEC track and ECAL cluster pairs.

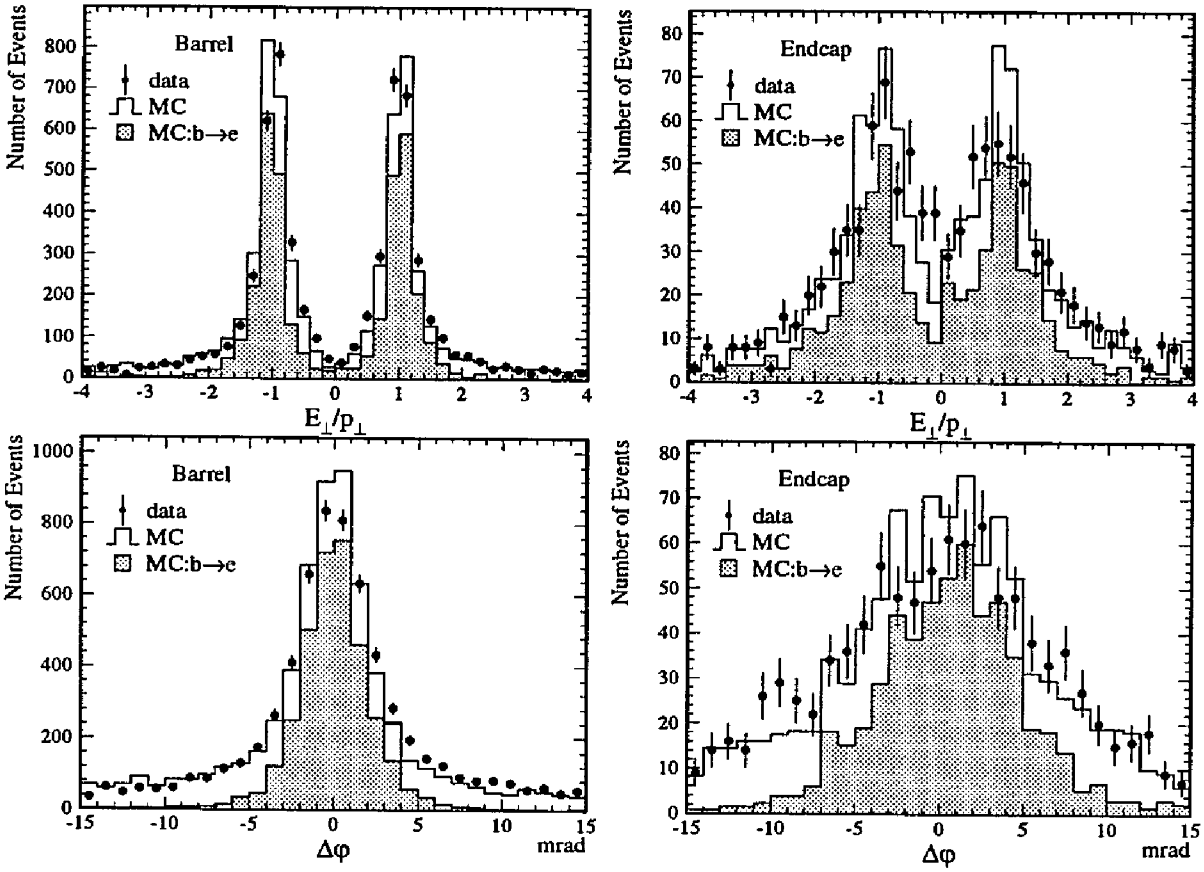

FIG. 4.11: Cut variables used to select electrons from matched TEC track and ECAL cluster pairs (continued).

4.6 Muon Identification

To reach the muon chambers from the interaction vertex, a particle must traverse approximately 6 nuclear absorption lengths and 130 radiation lengths of material. For the most part, only energetic muons can penetrate this much material; however, there is significant background among the tracks detected in the muon chamber from the punch-through of hadronic particles (mostly charged pions and kaons) produced in nuclear interactions at the back end of the hadron calorimeter.

In the data reconstruction process, track segments in each set of muon chambers are combined to form tracks that span all three chambers. A complete fit of this track is made with all of the hits in the various muon chambers. Muon identification begins with a reconstructed MUCH track that is required to have track segments in at least 2 (out of 3) p-chambers and at least 1 (out of 2) z-chamber. Additional constraints are applied to require that the tracks come from the interaction region. All of the cuts are summarized in Table 4.6.

Table 4.6: Cuts used for muon selection.

$N_{\mathrm{p-seg}}$	> 1
$N_{z-\mathrm{seg}}$	> 0
R/σ_R	< 4
$\|z\|/\sigma_z$	< 4
R	< 200 mm
$\|z\|$	< 300 mm
p	4-30 GeV

The muon tracks are extrapolated back to the center of the detector, and the transverse (longitudinal) point of closest approach to the interaction vertex, $R \pm \sigma_R$

$(z \pm \sigma_z)$, is determined from the track parameterization. These distances must be less than four standard deviations from zero and have absolute maximum limits. Because there can be appreciable multiple scattering of the muon as it makes its way through the inner detector, the vertex requirements are less stringent than for TEC tracks.

The dominant sources of low energy muons are from the weak decays of π, K and D mesons. There are more sources of low energy muons with higher branching ratios than sources of low energy electrons. To reduce this larger background, a higher minimum momentum cut is required for muons compared to the minimum energy required for electrons. The momentum of muons from the semileptonic decay of the b hadrons has an upper bound for the same reason as given in the previous section for electrons, and therefore a maximum momentum cut is also imposed.

The comparison of data with Monte Carlo for each cut variable is displayed in Figs. 4.12 and 4.13. In each histogram all cuts were applied except the one that is plotted. The plots are normalized to the total number of events. The simulation of the z-chamber efficiency does not match well with the data distribution. The main difference lies in dividing the sample between 1 and 2 z-segments. Since the selection requires at least one chamber, the total efficiency does not differ much between data and Monte Carlo. The good agreement for the measured momentum, which includes the z-chamber information, confirms the adequacy of the z-chamber simulation.

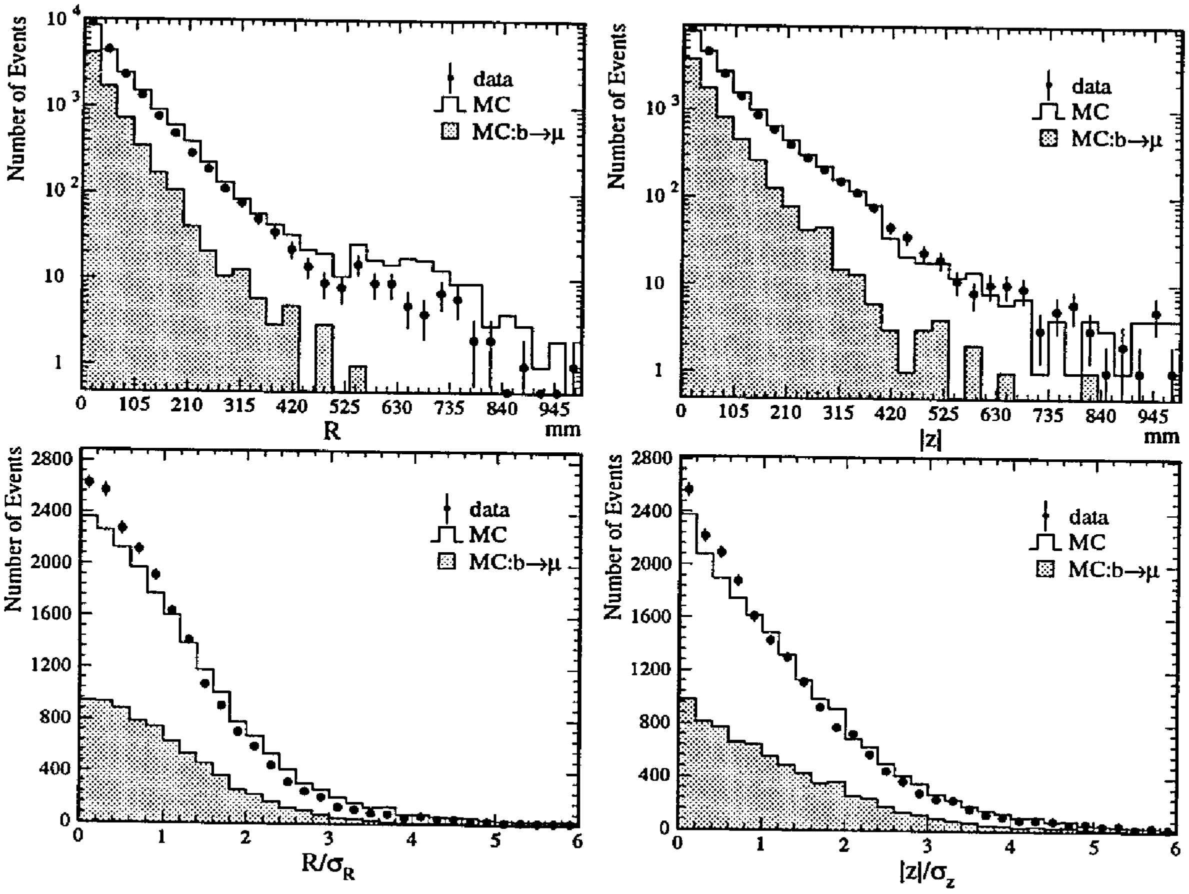

FIG. 4.12: Cut variables used to select muons.

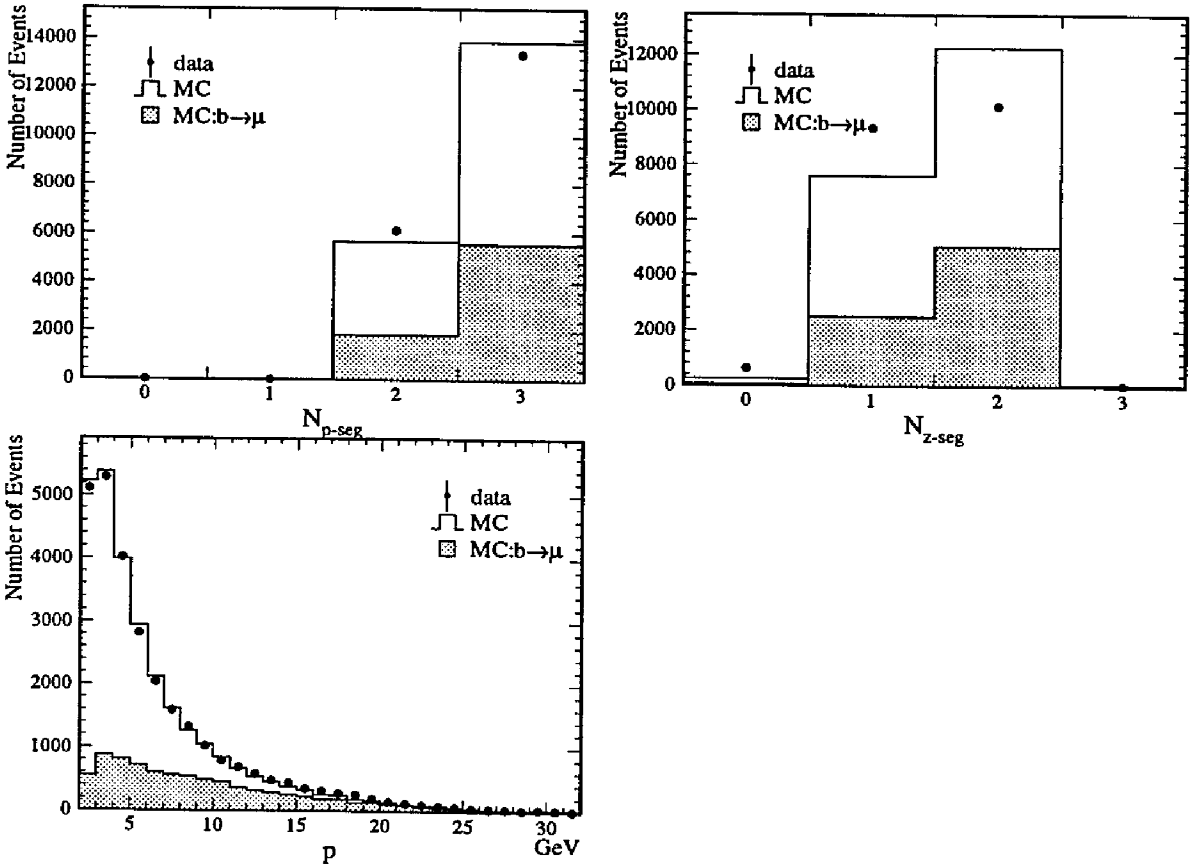

FIG. 4.13: Cut variables used to select muons (continued).

Chapter 5

Analysis

5.1 Introduction

In order to measure $A_{b\bar{b}}$ a data sample containing $b\bar{b}$ quarks must be selected, the production axis of the primary quark pair must be determined, and the hemisphere that contained the b (or $\bar{b}$) quark must be identified. The semileptonic decay of the b quark provides a method for both identifying $b\bar{b}$ events and determining the sign of the charge of the quark that decayed. The observed asymmetry using lepton tagging, $A^{obs}_{b\bar{b}}$, must then be corrected for B^0-$\bar{B}^0$ mixing. The mixing parameter, χ, can be measured from events in which both b quarks are tagged by a lepton.

Since there are many sources of leptons in hadronic events, lepton identification alone is not sufficient for extracting $A^{obs}_{b\bar{b}}$ and χ. The transverse momentum of the lepton with respect to the nearest jet (p_T), however, can be exploited to distinguish semileptonic b decays from background. Additional information provided by the energy of the jet nearest to the lepton (E_{jet}) can further enhance the b selection efficiency.

Implicit in the lepton tagging scheme is the requirement that the detector accurately determine the charge of the lepton. The probability that the lepton charge is measured incorrectly, which is referred to as charge confusion, must be determined from the data and included in the calculation of $A_{b\bar{b}}$.

The following sections describe the experimental observables used in the asymmetry and mixing measurements and the calculation of the charge confusion probability.

5.1.1 Thrust Axis

At center-of-mass energies around the Z resonance there is a large amount of kinetic energy in the final state even after the primary quark pair has hadronized. This results in highly collimated jets of hadrons that on average approximate the direction of the leading quark pair. The experimental determination of this direction is based on the thrust axis, which is defined as the unit vector $\hat{n}$ that maximizes the thrust

$$T = \max\left[\frac{\sum_i |\vec{p_i} \cdot \hat{n}|}{\sum_i |\vec{p_i}|}\right],$$

where the sum runs over the momentum vector of all of the clusters in the detector. This axis is well defined even in events with more than two jets. For example, gluon bremsstrahlung from one of the primary quarks can result in hadronic events with 3 or more jets. The Feynman diagram for this process and a schematic drawing of

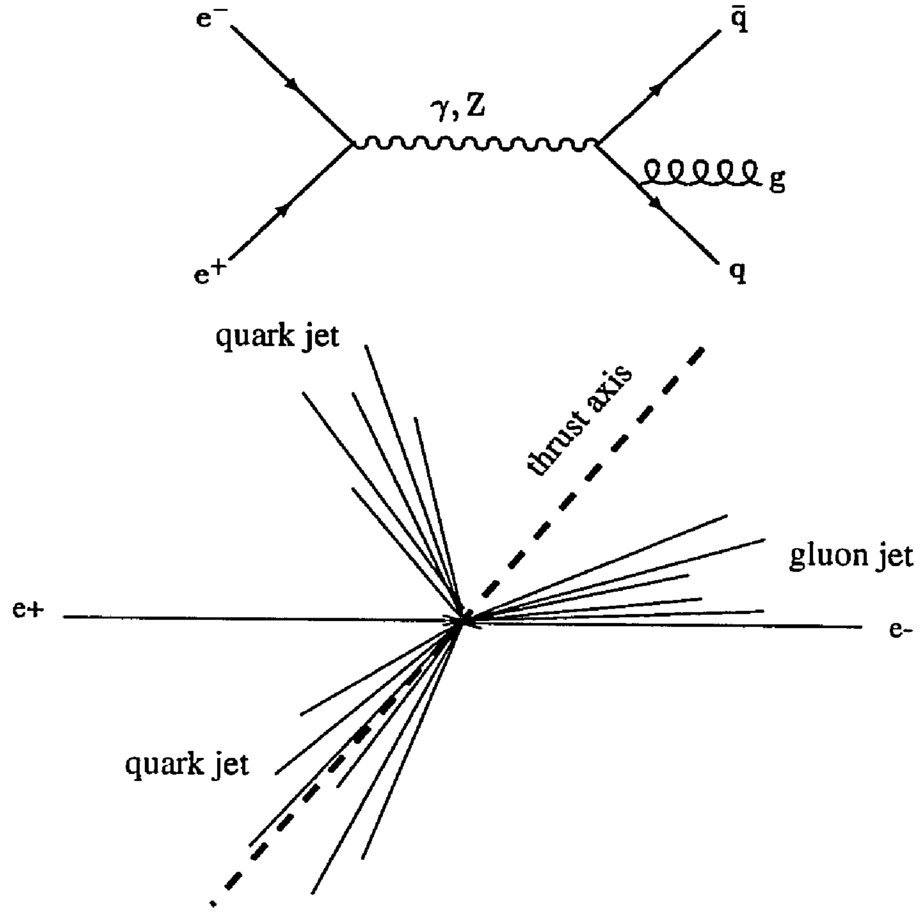

FIG. 5.1: Lowest order diagram for final state gluon bremsstrahlung and the associated event topology. The quarks and gluon each hadronize into a jet.

the experimentally observed topology of such an event is depicted in Fig. 5.1. From $b\bar{b}$ events generated with JETSET 7.3 (which includes gluon radiation), one can see in Fig. 5.2 that the thrust axis agrees with the original quark axis to within a few degrees. The polar angle of this axis with respect to the beam line θ_{thrust} is used in the determination of $A^{\mathrm{obs}}_{b\bar{b}}$.

5.1.2 Transverse Momentum: p_T

It was described in Section 2.4 that the transverse momentum of the lepton with respect to the parent hadron direction can be used to identify prompt b decay events.

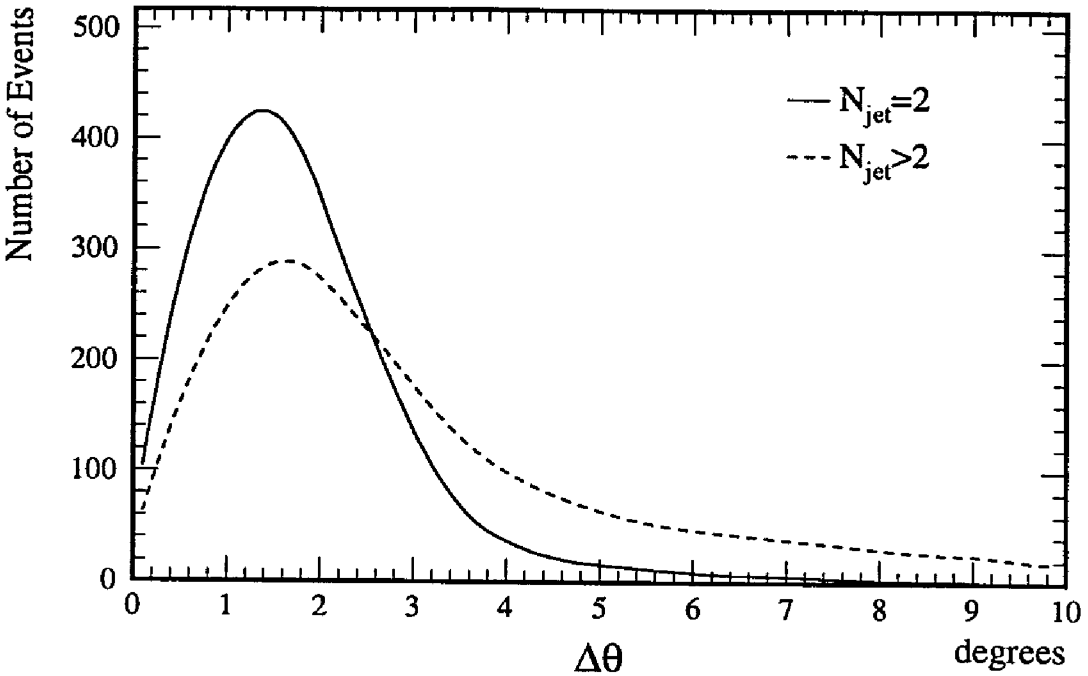

FIG. 5.2: Angle between the thrust axis and the production axis of the b quark in $b\bar{b}$ events generated with JETSET 7.3 in which at least one of the b quarks decayed semileptonically.

Since the decay is not completely reconstructed, the precise direction of the parent b hadron is not experimentally determined. However, the axis of the jet closest to the selected lepton is a good approximation of the b hadron direction. The jet axis is determined experimentally by adding the momentum vectors of the jet constituents. The direction of the resultant vector is the axis of the jet.

Figure 5.3 compares the direction of the b hadron to both the axis of the nearest jet and the thrust axis in simulated $b\bar{b}$ events in which at least one b quark decayed semileptonically. In multijet events ($N_{jet} > 2$), the jet axis is significantly better than the thrust axis in indicating the b hadron direction. Because of gluon radiation (see Fig. 5.1), the b hadron direction may deviate significantly from the thrust axis.

The p_T used in this analysis is calculated using the axis of the nearest jet after

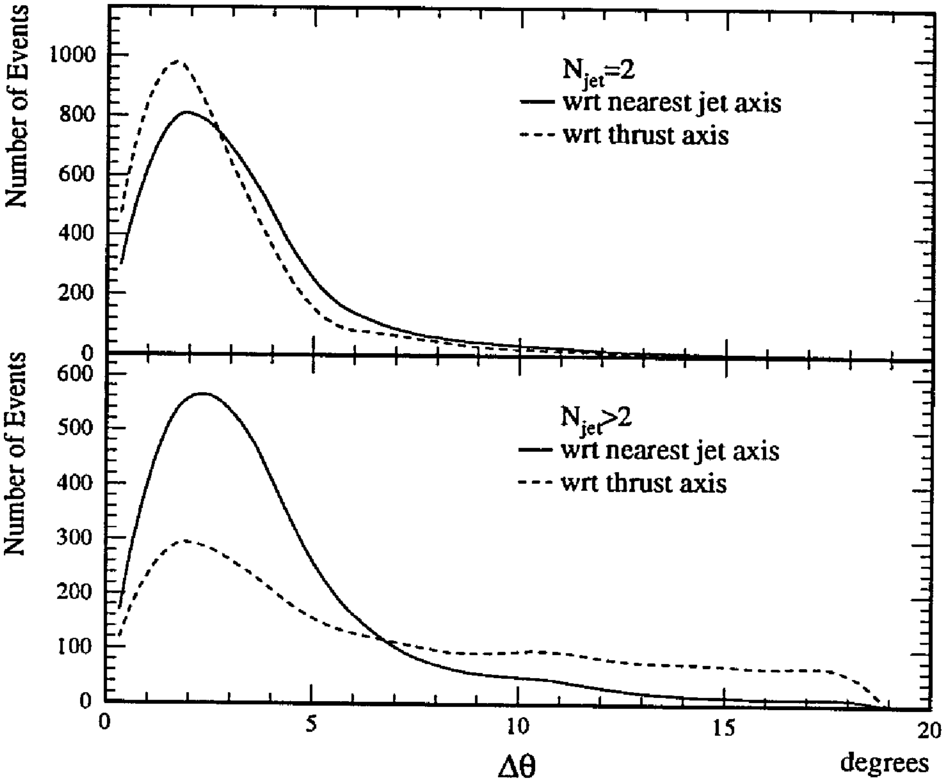

FIG. 5.3: Angle between the b hadron and either the thrust axis or the axis of the jet closest to the lepton from JETSET 7.3 generated $b\bar{b}$ pairs that decay semileptonically.

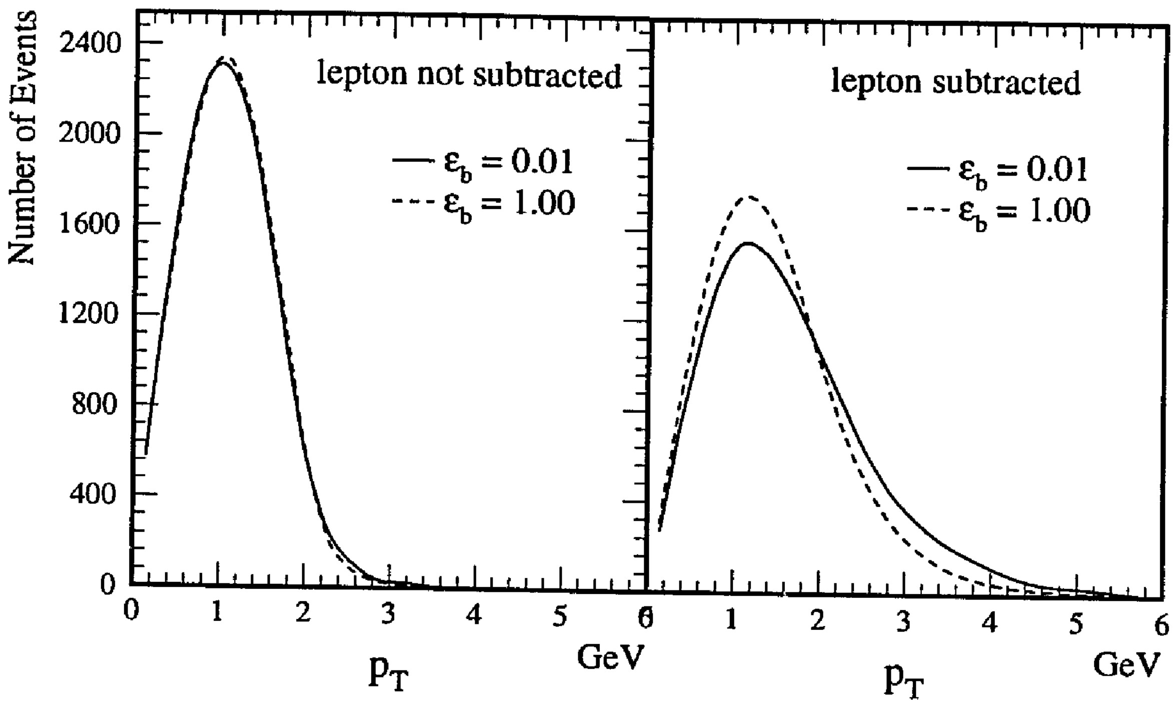

FIG. 5.4: Transverse momentum of the prompt lepton from $b\bar{b}$ events generated with JETSET 7.3 using the Peterson fragmentation function with ϵ_b= 0.01 and 1.00. The result of subtracting the lepton from the jet before calculating p_T is indicated in the second plot.

the lepton has been removed from the jet. Since the fragmentation for b quarks is hard, the non-b hadrons in the jet do not acquire much of the available kinetic energy. The fragmentation for lighter quarks is much softer, so more of the kinetic energy is carried by the nonprimary hadrons. Since the b hadron carries a greater fraction of the momentum of a jet, the decay products of the b hadron will, on average, have greater momentum than the other particles in the jet. Subtracting the lepton from the jet exploits this difference in average momenta and enhances the selection power of p_T. To illustrate this, Fig. 5.4 shows a comparison of the two methods of calculating p_T for the decay of a b quark with either hard ($\epsilon_b = 0.01$) or soft ($\epsilon_b = 1.00$) Peterson fragmentation. Without lepton subtraction, the p_T distribution for hard and soft fragmentation is identical; however, with lepton subtraction, the hard fragmentation results in higher values of p_T.

5.1.3 Charge Confusion

The sign of the lepton charge must be accurately measured to determine the side of the event that contained the b or $\bar{b}$ quark. For muons, the charge is determined from the curvature of the track found in the muon chambers. The electron charge is determined from the curvature of the track in the TEC that was matched with the ECAL cluster.

The momentum resolution of the muon chambers is 3% at 45GeV [30]. Such high resolution results in only a small amount of charge confusion. Since the sum of the charges in a Z decay must be zero, the amount of muon charge confusion can be estimated by counting the number of like-sign muons in $Z \rightarrow \mu^+\mu^-$ events. From an analysis of muon pairs in the data, the probability for measuring the wrong muon charge was determined to be $0.2 \pm 0.2\%$ [76].

The lever arm (0.317 m) for the curvature measurement of tracks in the TEC is much less than that for measurement in the muon chambers ($\sim$ 3 m), which results in reduced momentum resolution and greater charge confusion for tracks in the central drift chamber.

The amount of charge confusion in the TEC can be directly measured over a broad range of transverse momenta by examining Z decays to a pair of tau leptons. The branching ratio for a tau lepton to decay to a muon and two neutrinos is 17.6%. The probability that at least one tau in a $Z \rightarrow \tau^+\tau^-$ event decays to a muon is therefore 32.1%. Since the muon must share the initial momentum of the tau lepton with the two neutrinos in the decay, the momentum spectrum of the muon extends from zero up to the beam energy. The experimental signature for these tau decays is extremely clean: one hemisphere of the event contains exactly one track in the central drift chamber and one track in the muon chambers. Using the precision muon chambers to define the transverse momentum and charge of the muon, the charge confusion in the TEC is simply the fraction of events in which the TEC charge disagrees with the muon chamber charge.

The angular coverage of the muon chambers includes all tracks that intersect with the barrel portion of the ECAL. However, the endcap ECAL region being well outside this volume, the technique of using muons tracked by the muon chambers to determine the charge confusion does not work for tracks in the forward region. For tracks in this region an alternative method based on the sum of the charges of all tracks in a tau pair event can be used. A tau lepton decays 86% of the time into a single charged particle, a tau neutrino and zero or more neutral hadrons ("1-prong" decay). Thus, 74% of all tau pair events are 1-prong/1-prong. The sum of the charges of the two tracks in such events must be zero due to charge conservation, so the fraction of detected like-sign tau pairs is a measure of the charge confusion in the TEC.

Tau pairs were selected in the barrel region of the detector ($\cos\theta < 0.7$) by making the following cuts:

1. The total energy in the ECAL must be between 2 and 60GeV.

2. The number of clusters in the ECAL must be less than 13.
3. The number of tracks in the TEC must be less than 9.
4. There must be at least one scintillator counter hit within 3 ns of the beam crossing.
5. The event can contain only two or three jets, each with energy greater than 3GeV.
6. The angle between the two most energetic jets must be at least 166°.
7. The event can contain only one muon and the muon momentum must be less than 0.88 E_{beam}.
8. The event is rejected if it contains an ECAL cluster with energy 0.88 E_{beam} and a shower profile that is consistent with an electron.

These cuts were derived from the analysis used to measure the $Z \rightarrow \tau^+\tau^-$ cross-section in the barrel region of the detector [72], and they can be extended to include the endcap region by making the following modifications:

1. The scintillator cut is not required for $\cos\theta > 0.8$.
2. The total energy in the ECAL must be greater than 6GeV.
3. Events with $\cos\theta > .97$ are rejected.
4. Events with the thrust axis in the gap region of the BGO ($\cos\theta$= 0.7-0.8) are rejected if the ratio of front energy to total energy in the HCAL in this region is greater than 80%.

In a large fraction of tau events in the forward region, the hadronic showers are completely contained within the hadron calorimeter endcaps and no scintillators fire. The scintillator cut is therefore relaxed in the endcap region.

Since the fiducial volume of the muon chambers only extends to $\cos\theta = 0.8$, muon pairs cannot be rejected for the endcap region by detecting tracks in the muon chambers. Muons do not deposit much of their energy in the BGO, so increasing the cut on the minimum energy in the calorimeter eliminates much of the muon pair background.

The identification of energetic clusters in the ECAL consistent with electron showers is used to reject Bhabha events; however, there is a gap in the ECAL coverage in polar angles between 44° and 36°. Tracks in this region go directly into the hadron calorimeter. The front segment of the HCAL is approximately 22 radiation lengths and 0.8 nuclear absorption lengths thick. Electrons deposit nearly all of their energy in this region, while hadrons penetrate much further into the HCAL. The cut on the ratio of front over total energy eliminates electromagnetic showers and therefore rejects Bhabhas.

From the 1991 data sample, 10498 events satisfied the tau selection cuts listed above. The angular distribution of the thrust axis in the data and Monte Carlo is displayed in Fig. 5.5. The data and Monte Carlo are normalized to the number of events in the barrel region of the detector ($\cos\theta < 0.7$). Muon pair and Bhabha events are suppressed but cannot be completely eliminated in the endcap region.

Charge Confusion in the Barrel Region

The muon selection cuts from Chapter 4 were applied to the selected sample of tau events with the additional requirements that the muon track be reconstructed in all three p-segment chambers and that there be a single track in the TEC chamber in the same hemisphere as the muon. The TEC track was required to satisfy the quality cuts used in the electron identification selection. The transverse momentum distribution

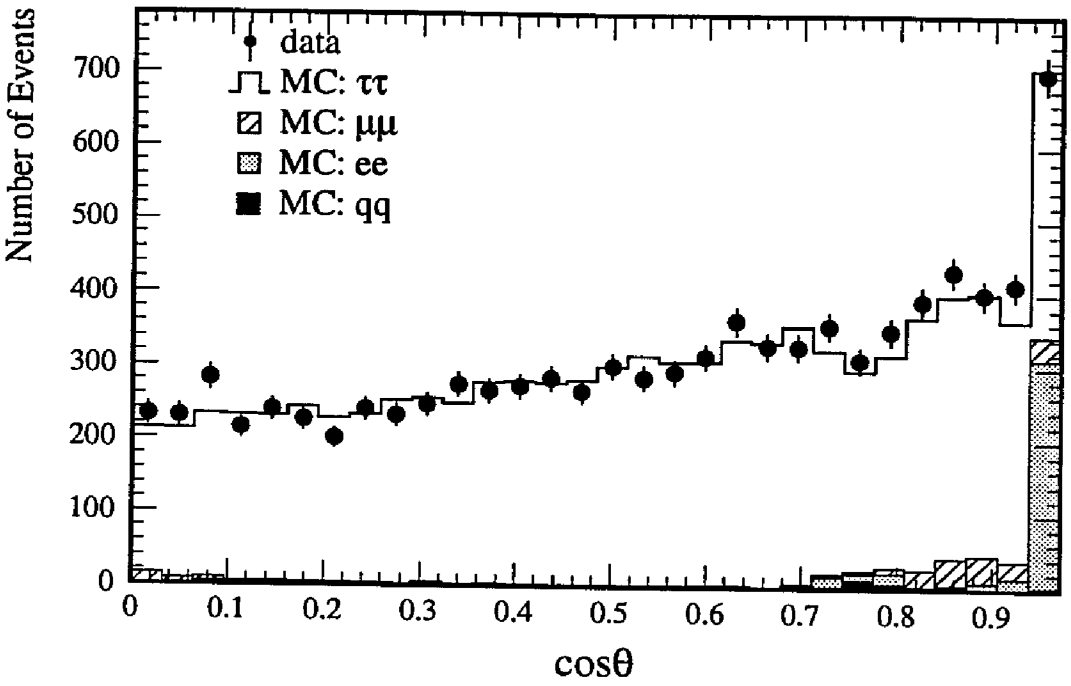

FIG. 5.5: Data and Monte Carlo events that satisfy the tau pair selection criteria. The data and Monte Carlo are normalized to the number of events in the barrel region of the detector ($\cos\theta < 0.7$).

of the 973 muons that satisfy these cuts is displayed in Fig. 5.6. The fraction of these muons in which the charge determined by the TEC disagreed with the charge determined by the MUCH is a direct measure of the TEC charge confusion. Binning the data in terms of the $p_\perp$, the transverse momentum measured by the MUCH, the charge confusion in the TEC is shown in Fig. 5.7. Fitting a second order polynomial to the data results in a parameterization of the charge confusion of the following form

$$f = a + bp_\perp + cp_\perp{}^2,$$

where

$$a = 0.0129 \pm 0.0120,$$

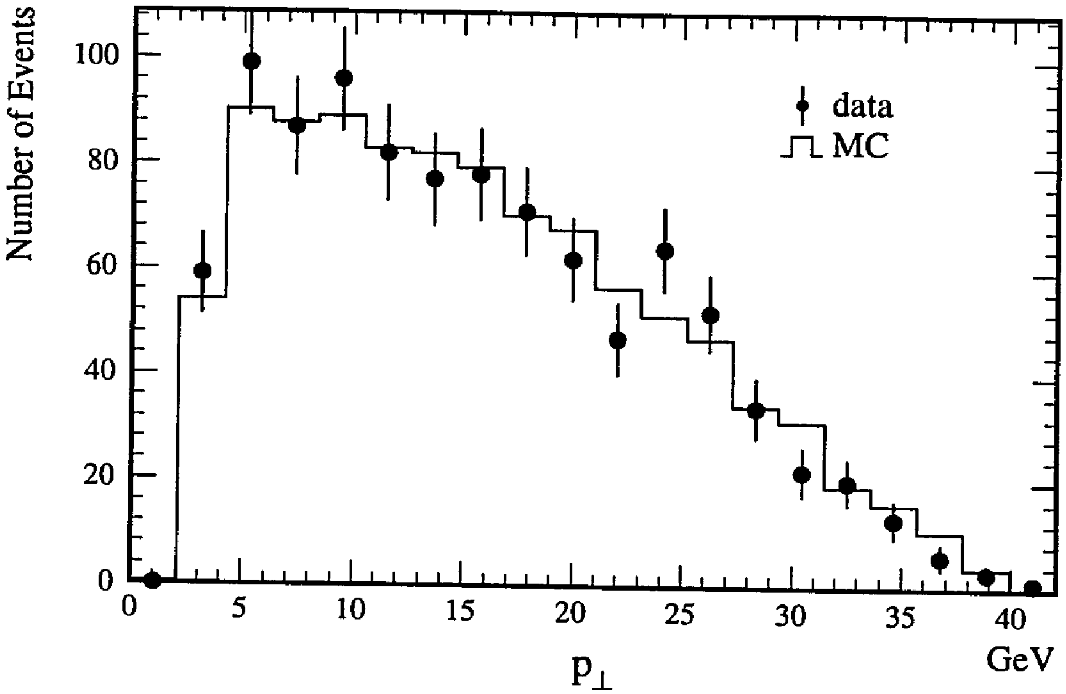

FIG. 5.6: Comparison of data and Monte Carlo distributions of the transverse momentum of muons with matching TEC tracks from selected tau events.

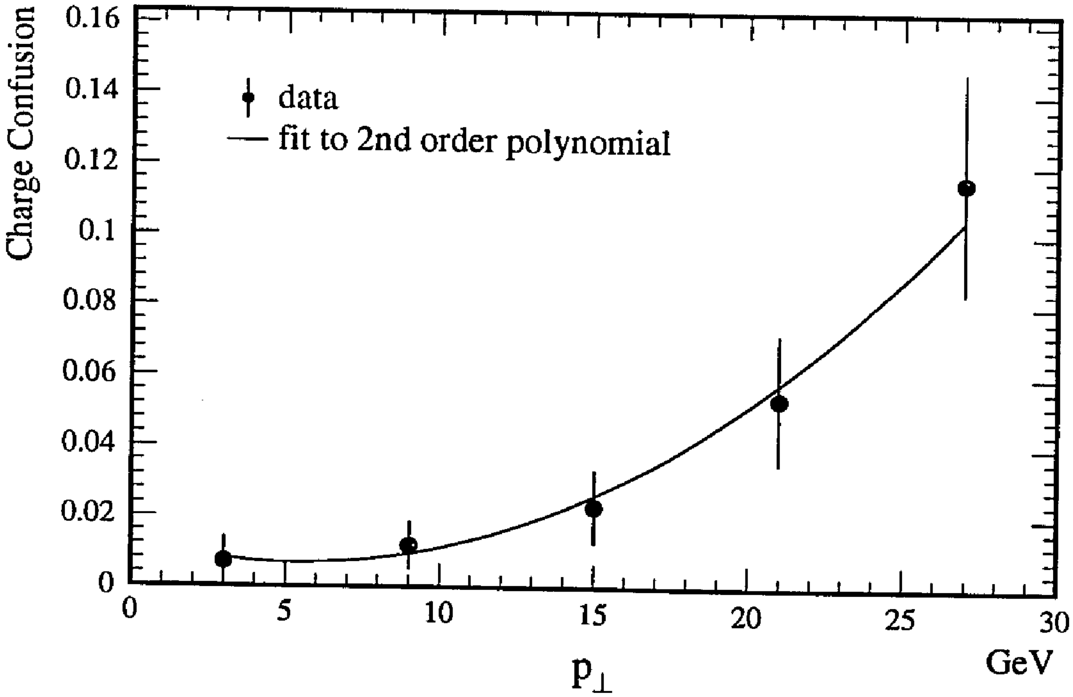

FIG. 5.7: Charge confusion in the TEC for tracks in the barrel region from muon tracks matched with TEC tracks in selected tau events.

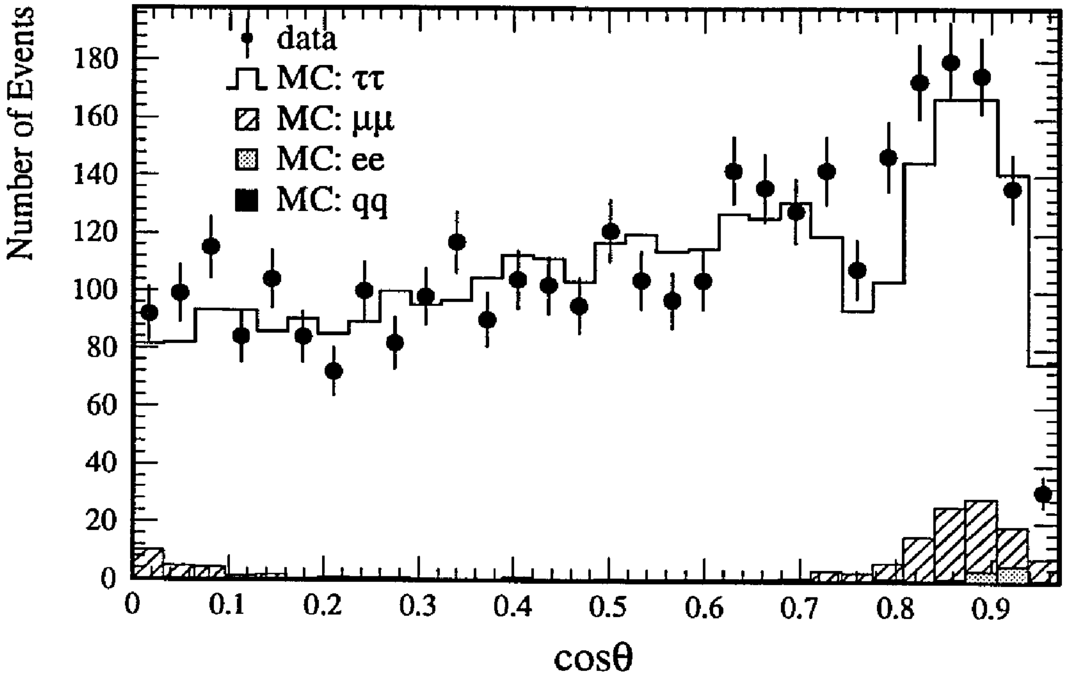

FIG. 5.8: Thrust axis distribution for selected 1-prong/1-prong tau pair events.

$$b = -0.00228 \pm 0.00239 \text{ GeV}^{-1}, \text{ and}$$

$$c = 0.000210 \pm 0.000099 \text{ GeV}^{-2}.$$

Charge Confusion in the Endcap Region

In addition to the tau selection cuts detailed above, 1-prong/1-prong tau decays were selected by requiring that there be two and only two tracks in the TEC and that both tracks satisfy the quality criteria used in the electron identification. The thrust axis distribution for the 3364 events that passed these cuts is displayed in Fig. 5.8. The Monte Carlo is normalized to the data in the barrel region ($\cos\theta < 0.7$) so that the relative efficiency of the barrel and endcap regions can be compared.

Agreement between the data and Monte Carlo in the endcap region is question-able. There is a slight excess of data events in the gap between the ECAL barrel and endcap ($0.7 < \cos\theta < 0.8$). Whether this can be attributed to a genuine error in the simulation or to a legitimate unsimulated inefficiency in the data is not clear. However, tracks in this region do not enter the endcap, so their effect on the measurement of the charge confusion for tracks that do enter the endcap is small.

The tracking efficiency in the far forward region is worse than what is indicated by the Monte Carlo. There are fewer data than Monte Carlo events in the last bin in $\cos\theta$ in Fig. 5.8, which is not the case in Fig. 5.5 in which there were no significant tracking requirements. Since the Monte Carlo events are not used in the charge confusion measurement, this difference in efficiency poses no serious problem.

The Monte Carlo events indicate that background from muon and electron pairs is highly suppressed but cannot be completely eliminated. Since the sum of the charges for these events should also be zero, they contribute to the number of like-sign events in the same way as do the 1-prong/1-prong tau events.

The fraction of like-sign events as a function of the thrust angle is plotted in Fig. 5.9. There is significantly more charge confusion in the data than in the Monte Carlo and the charge confusion increases dramatically for tracks in the forward region. Since the precision with which the curvature, and thereby the charge, of a given track can be measured depends on the transverse track length, tracks in the forward region, which exit through the end flange without traversing much of the central drift chamber, are not well measured.

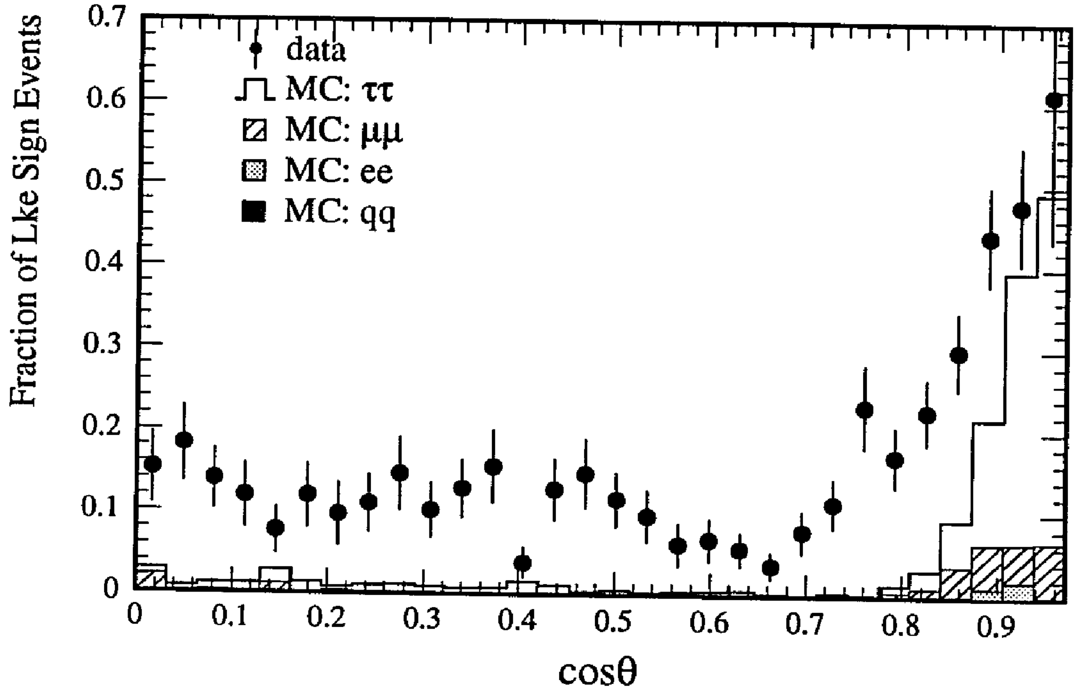

FIG. 5.9: Fraction of events with the same sign for selected 1-prong/1-prong tau pair events.

The probability of obtaining a like-sign event is

$$P_{12} = p_1(1 - p_2) + p_2(1 - p_1), \tag{5.1}$$

where p_1 and p_2 are the probabilities for incorrectly measuring the charge of each track. Since the charge confusion is expected to vary as a function of the transverse track length, the data were binned in terms of the outer wire number (N_{out}) of each track. A three parameter chisquare fit to the fraction of like-sign events in the data was performed using Eq. (5.1), where the three parameters corresponded to the charge confusion for tracks with $N_{out} \leq 20$, $20 < N_{out} < 40$, and $N_{out} \geq 40$. The data distribution for the outer wire number of the two tracks with the choice of binning is displayed in Fig. 5.10. The fraction of like-sign events in each bin is given in

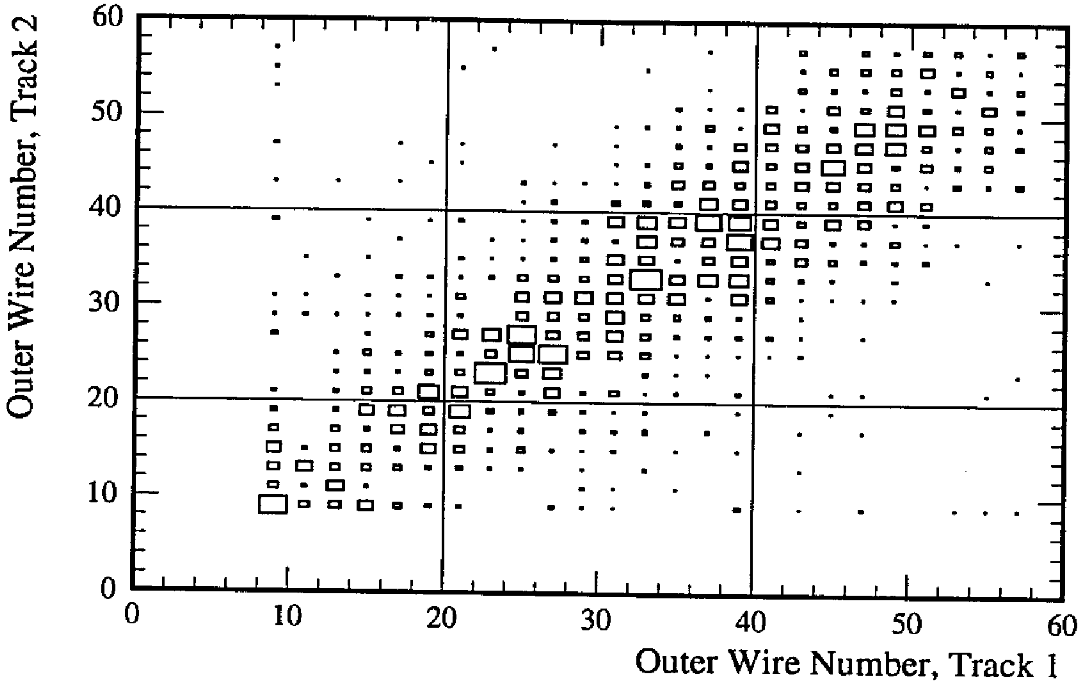

FIG. 5.10: Scatter plot of the outer wire number of the two tracks in 1-prong/1-prong selected tau events. The grid indicates the choice of binning used in the fit.

Table 5.1. Since the probability is symmetric, $P_{ij} = P_{ji}$, the off-diagonal bins were

Table 5.1: Fraction of like-sign events binned in the outer wire number of the two tracks.

N_{out}	≤ 20	20 - 40	≥ 40
≥ 40	0.1980 ± 0.0008	0.2066 ± 0.0014	0.2000 ± 0.0160
20 - 40		0.3869 ± 0.0008	0.4737 ± 0.0026
≤ 20			0.5000 ± 0.0025

grouped together. The result of the chisquare fit is listed in Table 5.2. As expected,

Table 5.2: Charge confusion from two track selected tau events.

N_{out}	charge confusion
≥ 40	0.1005 ± 0.0170
20 - 40	0.2311 ± 0.0218
≤ 20	0.3915 ± 0.0619

the charge confusion increases for low values of N_{out}.

Measured in this way, the charge confusion is averaged over the transverse momentum of all of the tracks in the bin. It was seen in the barrel region (see Fig. 5.7) that the charge confusion increases with higher transverse momentum. The momentum of a track that was incorrectly reconstructed is not correlated with the true momentum, and unlike the barrel case, in the endcaps region there is no external measurement of the momentum to use as a reference. Furthermore, it is impossible in a given like-sign event to determine which track was incorrectly reconstructed. Thus the charge confusion in the endcap region measured from 1-prong/1-prong tau events cannot be parameterized in terms of the true transverse momentum. This poses a severe limitation on determining the charge confusion for inclusive electrons in hadronic events, since the momentum spectrum of such events is significantly different from that of tau events.

5.2 The Asymmetry Measurement

5.2.1 Introduction

Three different methods for determining $A_{b\bar{b}}$ were performed: counting, acceptance, and likelihood. The counting method measures the asymmetry by counting the number of events in the forward and backward region. The statistical error on this method can be simply parameterized and used to estimate the statistical significance of various subsets of the data sample. In particular, the significance of including the sample of events tagged by an electron in the BGO endcaps can be investigated this way.

The acceptance method uses the Monte Carlo to calculate the acceptance of the detector which is applied to the data to produce the corrected angular distribution from which the asymmetry can be measured directly. This method is superior to the counting method because it uses more detailed angular information; however, it still relies heavily on the simulation of the detector acceptance.

The most flexible method that is least sensitive to the detector acceptance is the likelihood method. A probability, which is a function of $A_{b\bar{b}}$, is assigned to each event. Maximizing the product of the probabilities for all events determines the preferred value of the asymmetry. This method is extremely versatile because many characteristics of the event, for example the thrust axis direction and the lepton momentum, can be included in the calculation of the event probability.

The first two methods treat each data event with the same statistical weight, so it is important to eliminate as much background from the sample as possible. For this reason, a p_T cut is imposed in those methods. This eliminates some of the signal and reduces the statistical precision of the measurement. In contrast, the likelihood method gives higher weights to events that are likely to be prompt b decays. In this way, the full data sample is used but the diluting effect of the background is suppressed.

Applying the selection criteria described in Chapter 4 to the data collected in 1991 results in the number of events listed in Table 5.3. In events that had multiple lepton candidates the one with the highest p_T was chosen.

Table 5.3: The 1991 data sample selecting at most one lepton per event.

lepton	no p_T cut	$p_T > 1$ GeV
e barrel	4118	3175
e endcap	784	549
μ	15499	6657
Total	20401	10381

Table 5.4 lists the Monte Carlo prediction for the composition of the data sample broken down into separate event categories. The third column lists the asymmetry of the event category as tagged by the emitted lepton (A_{tag}). Note that category 4, the cascade decay $b \to c \to \ell^+$, has a tagged asymmetry exactly opposite to $A_{b\bar{b}}$, which tends to decrease the overall observed asymmetry.

Category 5 consists of charged tracks that come from the decay of b hadrons other than the decays listed in categories one through four. The charge of the track is correlated with the b quark charge for some of these events. For example, pions or kaons from the direct decay of the virtual W boson emitted by the b quark carry the same charge information as does the lepton in the semileptonic decay. If the

Table 5.4: Monte Carlo prediction for the composition of the single lepton sample in percent (%). The abbreviations *bar.* and *end.* stand for barrel and endcap respectively. The event categories include the charge conjugate of the listed process. Also, X represents charged tracks that were misidentified as leptons and leptons from the decay of light hadrons.

			no p_T cut			$p_T > 1$ GeV		
k	$A_{\rm tag}$	Category	e bar.	e end.	μ	e bar.	e end.	μ
1	$A_{b\bar b}$	$b \to \ell^-$	67.97	59.53	37.18	78.10	73.63	70.93
2	$A_{b\bar b}$	$b \to \tau^- \to \ell^-$	2.10	2.27	1.67	1.62	2.32	1.63
3	$A_{b\bar b}$	$b \to \bar c \to \ell^-$	0.62	0.86	1.53	0.34	0.50	0.73
4	$-A_{b\bar b}$	$b \to c \to \ell^+$	6.08	8.17	12.09	4.28	4.92	7.57
5	$\eta A_{b\bar b}$	$b \to X$	4.73	6.26	4.41	3.98	4.53	2.92
6	$-A_{c\bar c}$	$c \to \ell^+$	3.43	3.67	16.27	2.06	2.03	6.07
7	$A_{\rm back}$	background	15.08	19.24	26.85	9.62	12.07	10.13

pion or kaon is misidentified as a lepton, these events contribute to the observed asymmetry. The tagged asymmetry of this category is proportional to $A_{b\bar b}$, where η is the constant of proportionality, and can be determined from the fraction of events that are correlated with the b quark charge.

The tagged asymmetry from c$\bar{\rm c}$ events is opposite in sign to the b$\bar{\rm b}$ asymmetry and represents a significant background in the muon tagged sample. On the Z peak, the b and c asymmetries are related through Eq. (2.2),

$$\frac{A_{c\bar c}}{A_{b\bar b}} = \left(\frac{v_b a_b}{v_b^2 + a_b^2}\right)\left(\frac{v_c^2 + a_c^2}{v_c a_c}\right),$$

which is only weakly dependent on $\sin^2\theta_W$ and is approximately 0.70 ± 0.05 in the Standard Model. Therefore, in this analysis $A_{c\bar c}$ was fixed to $0.7 \times A_{b\bar b}$.

The background category consists of leptons from nonheavy quark decay and charged tracks that have been misidentified as leptons. From Monte Carlo studies,

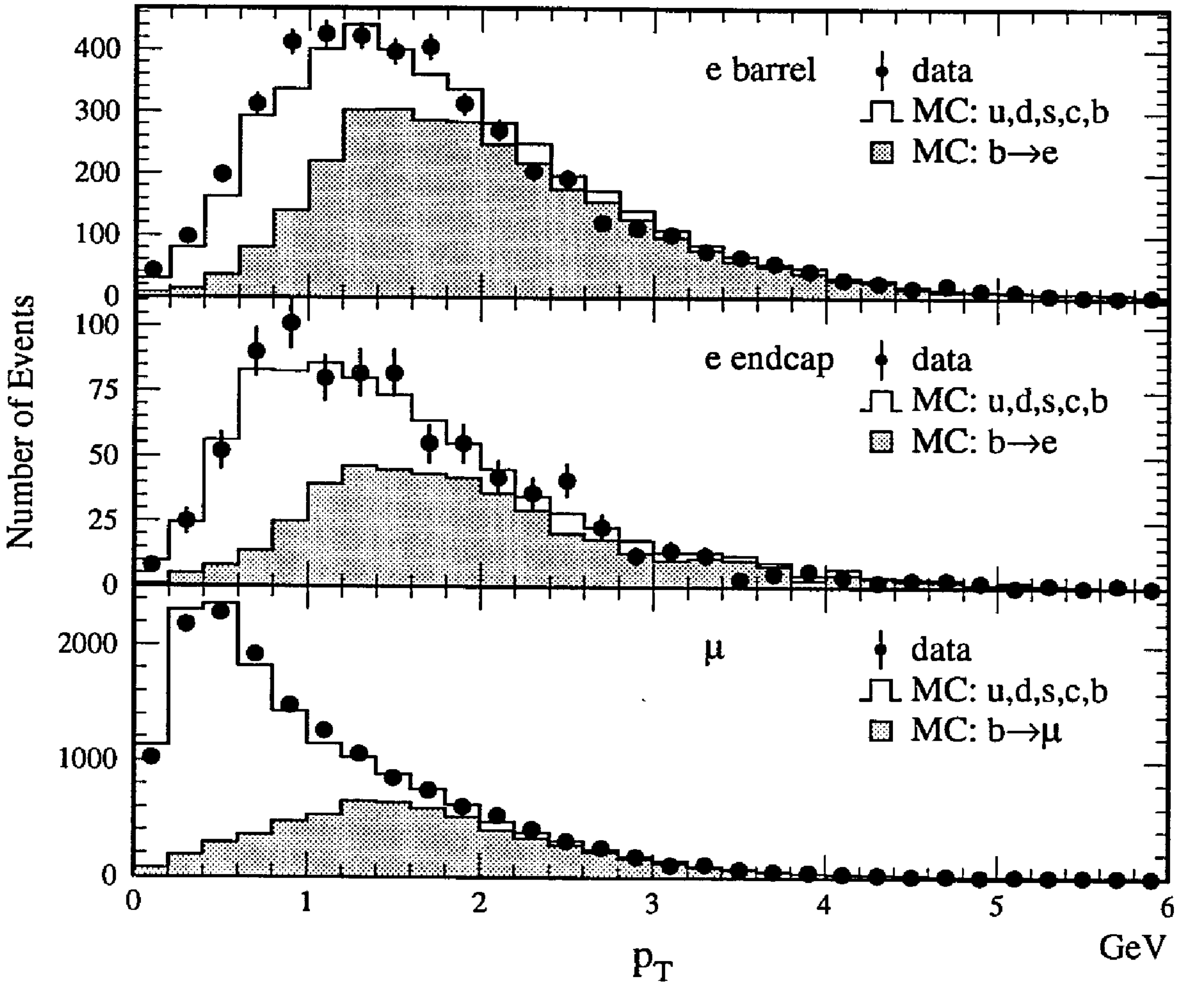

FIG. 5.11: Transverse momentum of the lepton with respect to the nearest jet.

the asymmetry for these events is found to be consistent with zero.

Figure 5.11 shows the p_T distributions for electrons and muons. There is much less background at low p_T values in the electron sample than in the muon sample. The shower shape requirement in the electron selection results in a minimum amount of isolation of the electron cluster in the ECAL, which translates into an implied p_T cut. Much of the background in both lepton samples can be removed by making a p_T cut at around 1 GeV; however, a significant number of signal events will be lost.

5.2.2 The Counting Method

The counting method is conceptually the simplest way of determining $A_{b\bar{b}}$. For a given data sample, the observed asymmetry A^{obs} is

$$A^{\mathrm{obs}} = \frac{N_F - N_B}{N_F + N_B},$$

where N_F and N_B are the number of events in the forward and backward regions respectively. In terms of the experimental observables, forward is defined as $x \geq 0$ and backward as $x < 0$ where

$$x = \cos\theta = -Q_\ell \cos\theta_{\mathrm{thrust}},$$

Q_ℓ being the lepton charge and θ_{thrust} the angle between the thrust axis and the electron beam. The thrust axis direction is chosen to be on the same side of the event as the lepton.

The total observed asymmetry is the weighted sum of the observed asymmetries of the various event categories (A_k^{obs})

$$A^{\mathrm{obs}} = \sum_k A_k^{\mathrm{obs}} F_k,$$

where F_k is the fraction of events of type k in the sample. The asymmetry of each category is the result of convoluting the angular distribution with the acceptance. If the acceptance is symmetric with respect to $\cos\theta$, then A_k^{obs} is proportional to the full asymmetry $A_k^{\mathrm{obs}} = c_k A_k$, where the constant of proportionality c_k is independent of the asymmetry. The derivation of this relation and a formula for c_k is given in the Appendix, Section A.1.

In addition, errors in the measurement of the charge of the lepton reduces the observed asymmetry by $(1-2\epsilon)$, where ϵ is the probability of determining the wrong charge.

In terms of the categories in Table 5.4, the observed asymmetry is

$$\frac{A^{\mathrm{obs}}}{1-2\epsilon} = (c_1F_1 + c_2F_2 + c_3F_3 - c_4F_4 + \eta c_5F_5)A_{\mathrm{b\bar{b}}}^{\mathrm{obs}} - c_6F_6A_{\mathrm{c\bar{c}}} + A_{\mathrm{back}}F_7,$$

where $A_{\mathrm{b\bar{b}}}^{\mathrm{obs}} = (1-2\chi)A_{\mathrm{b\bar{b}}}$. Since the input b and c quark asymmetries are known $(A_{\mathrm{b\bar{b}}}^{\mathrm{mc}}, A_{\mathrm{c\bar{c}}}^{\mathrm{mc}})$, the Monte Carlo can be used to determine the coefficients c_k, the fractions F_k and the background asymmetry A_{back}. The observed asymmetry can then be written as

$$\frac{A^{\mathrm{obs}}}{1-2\epsilon} = C_{\mathrm{b\bar{b}}}\frac{A_{\mathrm{b\bar{b}}}^{\mathrm{obs}}}{A_{\mathrm{b\bar{b}}}^{\mathrm{mc}}} + C_{\mathrm{c\bar{c}}}\frac{A_{\mathrm{c\bar{c}}}}{A_{\mathrm{c\bar{c}}}^{\mathrm{mc}}} + A_{\mathrm{back}}F_7, \tag{5.2}$$

where the constants determined from the Monte Carlo for $\mathrm{b\bar{b}}$ and $\mathrm{c\bar{c}}$ events have been grouped together into $C_{\mathrm{b\bar{b}}}$ and $C_{\mathrm{c\bar{c}}}$.

Since the amount of charge confusion in the endcap region is much greater than that in the barrel, endcap electron events will be treated separately.

Asymmetry in the Barrel Region

For leptons in the barrel region of the detector, $A_{b\bar{b}}^{obs}$ was extracted from the observed asymmetry of the data with a p_T cut of 1.0 GeV. The results are listed in Table 5.5.

Table 5.5: The $b\bar{b}$ asymmetry from the counting method combining the muon and barrel electron samples with $p_T > 1$ GeV.

lepton	$A_{b\bar{b}}^{obs}$
μ	0.057 ± 0.020
e	0.086 ± 0.031
Total	0.066 ± 0.017

The charge confusion for the electron sample was determined to be 1.3 ± 1.0% by applying the parameterization from Section 5.1.3 determined from tau events to the transverse energy distribution of the electron sample in the data. Since the bulk of the distribution is below 10 GeV, the charge confusion for the electron sample is small.

As can been seen in Fig. 5.11, a cut on the p_T of the lepton increases the purity of the event sample. This results in two competing effects: a reduction of statistics and an enhancement of the observed asymmetry. Since the asymmetry of the major backgrounds is negative or nearly zero, reducing the background will increase the observed asymmetry. The location of the p_T cut was determined by modeling the asymmetry error to find a balance between the loss of events and the enhancement of the observed asymmetry.

The fractional error on the observed asymmetry is

$$\frac{\delta A^{\rm obs}}{A^{\rm obs}} = \sqrt{\frac{(1/A^{\rm obs})^2 - 1}{N}},$$

where N is the total number of selected events. In terms of the purity (p) and efficiency (e) of selecting prompt b decays in the sample, the observed asymmetry is

$$A^{\rm obs} \simeq C p A^{\rm obs}_{\rm b\bar{b}},$$

where C is a constant factor that accounts for acceptance and charge confusion. The Monte Carlo predicts that C is 0.75 for electrons and 0.89 for muons. The number of selected events is

$$N = \frac{e}{p} N_{\rm q\bar{q}}\, {\rm Br}({\rm b}\to\ell)\, {\rm Br}({\rm Z}\to{\rm b\bar{b}}),$$

where $N_{\rm q\bar{q}}$ is the number of selected $\rm q\bar{q}$ events, $\rm Br(Z\to b\bar{b})$ is the $\rm Z\to b\bar{b}$ branching ratio, and $\rm Br(b\to\ell)$ is the b semileptonic branching ratio.

Using the Monte Carlo to estimate the purity and efficiency, the fractional error $\delta A^{\rm obs}/A^{\rm obs}$ calculated using the equations listed above is plotted in Figure 5.12. The values used in the plot are $A^{\rm obs}_{\rm b\bar{b}} = 0.9$, $\rm Br(b\to\ell) = 0.117$, $\rm Br(Z\to b\bar{b}) = 0.152$, and $N_{\rm q\bar{q}} = 297300$. The shape of the distribution is insensitive to $A^{\rm obs}_{\rm b\bar{b}}$ and C, as well as to $\rm Br(b\to\ell)$, $\rm Br(Z\to b\bar{b})$, and $N_{\rm q\bar{q}}$. Changing any of these parameters will change the overall scale but does not change the location of the minimum.

For both electrons and muons the minimum fractional error occurs at a p_T cut

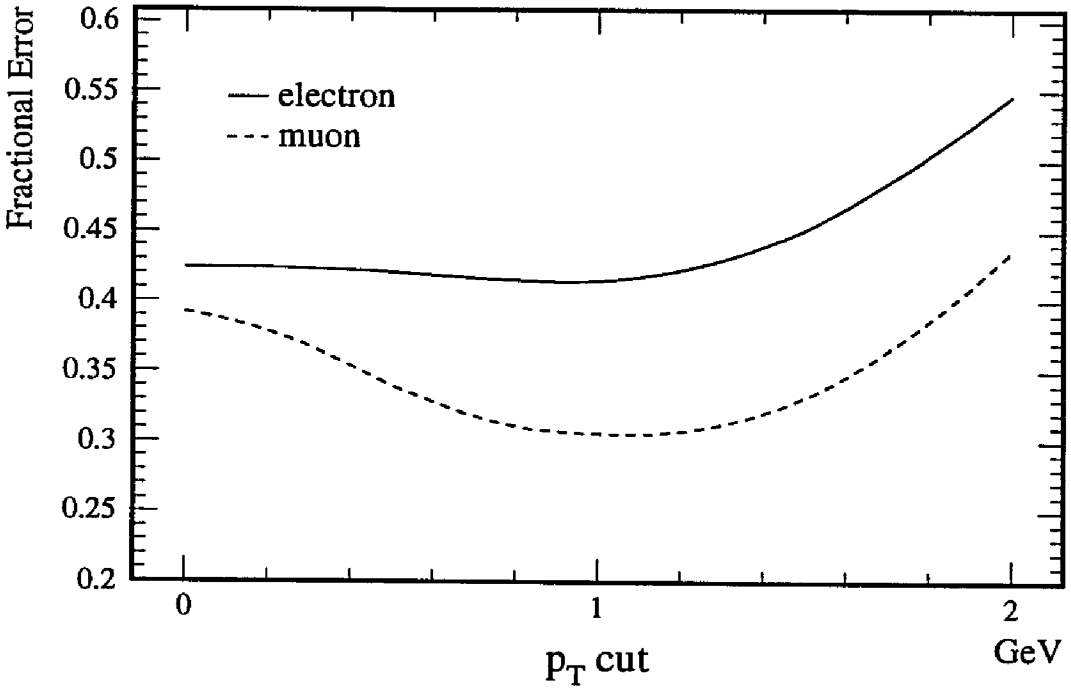

FIG. 5.12: Fractional error in A^{obs} as a function of p_T cut as predicted by the Monte Carlo.

of around 1.0 GeV. Since the selection efficiency for muons is greater than that for electrons, the muon error is smaller. For electrons, the purity does not improve much until the p_T cut is greater than 1.0 GeV; however, the improvement is offset by a large loss of events.

Systematics

Table 5.6 lists the contributions to the systematic error in the measurement of $A_{\text{b}\bar{\text{b}}}^{\text{obs}}$ using the counting method. Each contribution is varied by its stated error and the observed change in the asymmetry $\Delta A_{\text{b}\bar{\text{b}}}^{\text{obs}}$ is recorded in the table.

The first class of contributions affects the relative fraction of b and c decays in the data sample. The b$\bar{\text{b}}$ and c$\bar{\text{c}}$ partial widths, which determine the total number of heavy quark events produced from Z decay, were derived from the Standard Model

Table 5.6: Systematic errors in the counting method.

Contribution	value	variation(±)	$\Delta A^{\mathrm{obs}}_{\mathrm{b\bar{b}}}$
$\Gamma_{\mathrm{b\bar{b}}}$ (MeV)	378.0	2.5	0.0002
$\Gamma_{\mathrm{c\bar{c}}}$ (MeV)	313.4	5.2	0.0002
Br(b→ℓ)	0.117	0.006	0.0008
Br(c→ℓ)	0.096	0.006	0.0002
$\epsilon_b(x_E)$	0.05	0.01	< 0.0001
$\epsilon_c(x_E)$	0.50	0.10	0.0001
e charge confusion	0.013	0.010	0.0003
μ charge confusion	0.002	0.002	0.0002
$A_{\mathrm{c\bar{c}}}/A_{\mathrm{b\bar{b}}}$	0.7	0.3	0.0007
p_T cut (GeV)	1.00	0.25	0.0141
MC statistics			0.0075
Total (quadrature)			0.0160

using the Z mass measured by L3, m_H= 100 GeV and m_t= 150 GeV. The errors on the partial width are determined by the error on the Z mass and the variation of the top quark mass in the range 90-250 GeV and the Higgs mass in the range 50-1000 GeV. Since the heavy quarks are tagged through their semileptonic decay, the branching ratios Br(b→ℓ) and Br(c→ℓ) determine the fraction of events that can be detected. The value for Br(c→ℓ) is an average from measurements taken at PEP and PETRA [77] and the value for Br(b→ℓ) is an average as discussed in Section 2.4.

Variation of the heavy quark fragmentation parameters $\epsilon_b(x_E)$ and $\epsilon_c(x_E)$ alter the momentum spectrum of the emitted lepton. Since the momentum spectrum only enters through the p and p_T cut in the counting method, the effect from altering the fragmentation is small.

The error attributed to Monte Carlo statistics was calculated analytically from Eq. (5.2) using the corresponding errors for the constants determined from the finite sample of Monte Carlo events. The largest single error results from varying the location of the p_T cut.

5.2.3 Endcap Electrons

The BGO endcaps contribute to the measurement of $A_{\mathrm{b\bar{b}}}^{\mathrm{obs}}$ in two ways:

1. by increasing the acceptance for b events tagged with an electron, and
2. by sampling the region of the angular distribution that has a large asymmetry.

To clarify the second point, consider a perfect detector and a 100% pure sample of events that have asymmetry A. The differential cross-section is $\frac{1}{N}\frac{d\sigma}{dx} = \frac{3}{8}(1+x^2) + Ax$, so counting events with $|x| < 0.77$ results in an observed asymmetry $0.86 \times A$, whereas counting events with $|x| > 0.77$ results in $1.32 \times A$. The angle $\cos\theta = 0.77$ roughly corresponds to the division between the endcap and barrel portion of the BGO calorimeter.

Using the formula for the fractional error in the observed asymmetry, the expected improvement by adding endcap electron events can be estimated in the following way. The total observed asymmetry is the sum of the asymmetry in the barrel (A_{bar}) and endcap (A_{end}) regions weighted by the fraction of events in each region (F_{bar}, F_{end})

$$A^{\mathrm{obs}} = A_{\mathrm{bar}}F_{\mathrm{bar}} + A_{\mathrm{end}}F_{\mathrm{end}},$$

where the barrel region includes both the electron and muon sample. The ratio of the fractional error with and without endcap events is

$$R = \frac{\delta A^{\rm obs}}{A^{\rm obs}} / \frac{\delta A_{\rm bar}}{A_{\rm bar}} = \sqrt{(\frac{(1/A^{\rm obs})^2 - 1}{(1/A_{\rm bar})^2 - 1}) F_{\rm bar}}.$$

For asymmetries less than about 0.7, the ratio is closely approximated by

$$R \simeq \frac{A_{\rm bar}}{A^{\rm obs}} \sqrt{F_{\rm bar}}. \tag{5.3}$$

As can be seen from Table 5.3, the endcap electrons with a p_T cut at 1 GeV increase the electron sample by 15%, which represents an increase of 5% in the total lepton selection. According to Eq. (5.3) this translates into an improvement in the fractional error by less than 3%. To estimate the improvement from the increased observed asymmetry in the endcap, the selection efficiency and charge confusion in the data must be compared to the Monte Carlo.

The polar angle ($\cos\theta_e$) distribution for selected electrons is shown in Fig. 5.13. The data and Monte Carlo are normalized to the number of events in the barrel region. The gap between the barrel and endcap is clearly visible and appears slightly larger than the actual gap because the electron selection does not allow the ECAL cluster to fall too close to the edge of the calorimeter. In order to use the Monte Carlo to calculate $A_{\rm b\bar{b}}^{\rm obs}$ in the endcap region, the Monte Carlo events are binned in $\cos\theta_e$ and reweighted to reflect the lower selection efficiency seen in the data.

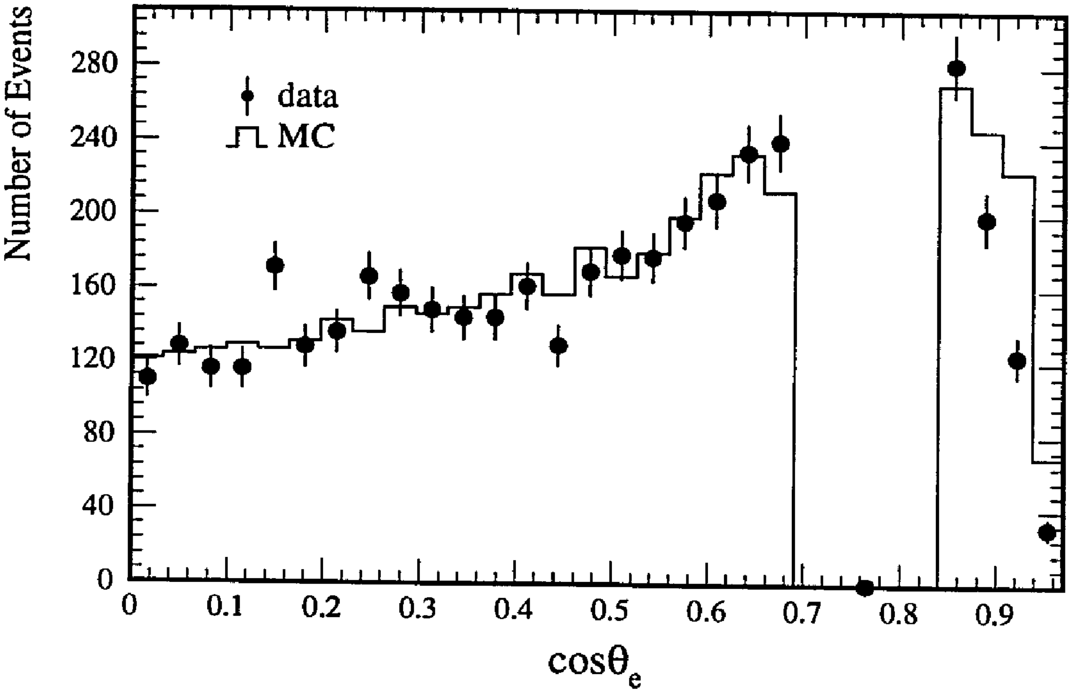

FIG. 5.13: Angular distribution of the selected electrons within the fiducial volume of the ECAL with $p_T > 1$ GeV. The data and Monte Carlo are normalized to the number of events in the barrel region ($\cos\theta_e < 0.7$).

The amount of charge confusion in the endcap sample was estimated using the results of the 1-prong/1-prong tau analysis. The data were binned in terms of the outer wire number of the electron track and the average amount of charge confusion was determined to be 25.1 ± 2.0%. This estimate, however, does not account for the difference between the transverse momentum distribution of the tracks in the electron sample and the tau sample used to parameterize the charge confusion (see Fig. 5.14). The momenta of the tracks in the tau sample are significantly higher than that of the endcap electrons and since the charge confusion increases with the transverse momentum, the endcap electron charge confusion is most likely overestimated. It was seen in the tau sample that the charge confusion was significantly worse in the data than in the Monte Carlo, so a lower bound on the electron charge confusion can

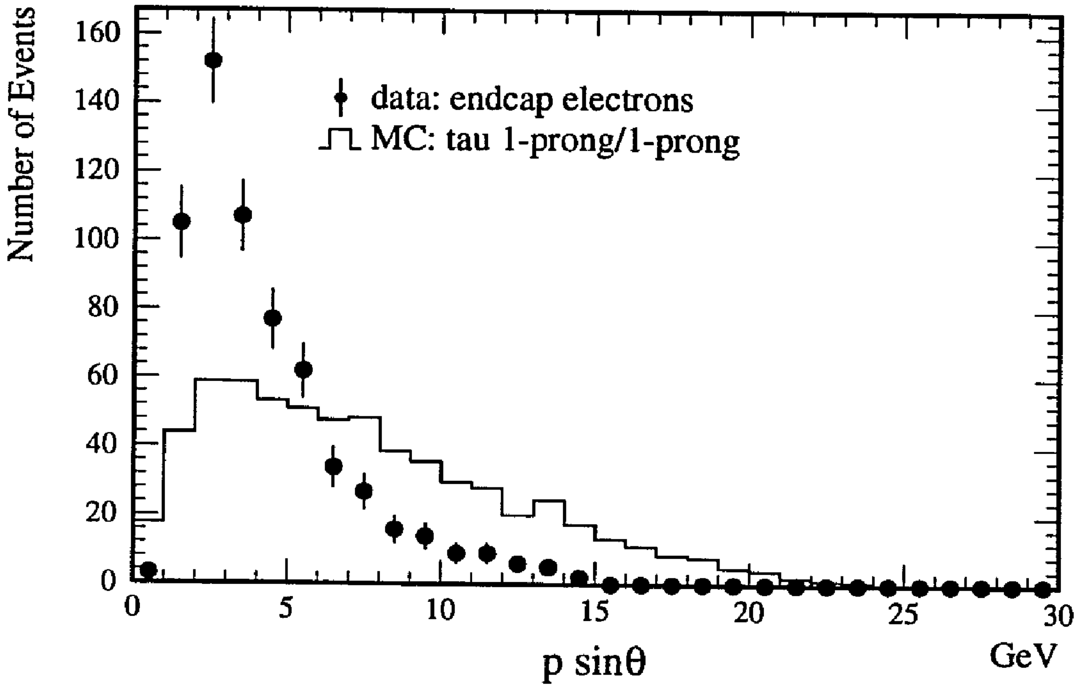

FIG. 5.14: Comparison of transverse momentum distribution for endcap electrons and 1-prong/1-prong selected tau events. For the inclusive electrons, the transverse energy of the ECAL cluster is plotted. For the Monte Carlo tau events, the generated transverse momentum of the track is plotted.

be determined from simulated data. The charge confusion predicted by the Monte Carlo for endcap electrons is 8.4 ± 0.5%. The true amount of charge confusion lies somewhere between these two extremes, so taking the average of these two values, the charge confusion is 18 ± 10%, where the error is chosen to cover the upper and lower extremes.

Using the value of the $b\bar{b}$ asymmetry measured in the barrel region (see Table 5.5), $A^{\text{obs}}_{b\bar{b}} = 0.066$, and the charge confusion from above, then the Monte Carlo predicts that the observed asymmetry in the barrel region is $A_{\text{bar}} = 0.044$ and, in the endcap region, $A_{\text{end}} = 0.055$. This would reduce the fractional error of the observed asymmetry by less than 2%. Therefore, the total improvement by including endcap electron events is expected to be less than 5%.

Turning to the real data, the observed asymmetry from endcap electron events with a p_T cut of 1 GeV is 0.013 ± 0.044, which results in $A_{b\bar{b}}^{obs} = 0.018 \pm 0.066$. The error on $A_{b\bar{b}}^{obs}$ increased because of the charge confusion correction factor $(1-2\epsilon)$, which is 0.62 in this case. The observed asymmetry is within one standard deviation of the Monte Carlo prediction; however, the low value could be indicative of unresolved problems in the data.

A number of effects mitigate the utility of endcap electrons in the asymmetry measurement. The correction due to charge confusion in the endcaps is large and has a large associated error. Because of the low tracking efficiency, the acceptance is not greatly increased. The Monte Carlo simulation of the tracking efficiency as a function of polar angle does not match well with the data. Overall, the expected improvement by including endcap electron events is small. Therefore, *endcap electron events are not included* in the determination of $A_{b\bar{b}}^{obs}$.

5.2.4 The Acceptance Method

The counting method of determining $A_{b\bar{b}}^{obs}$ is not sensitive to the shape of the angular distribution of the events. The only information extracted from the data is the number of forward and backward events. In contrast, by binning the data in $\cos\theta$ and using the Monte Carlo to calculate the background and acceptance for each bin, the angular distribution of prompt b decays can be reconstructed. The asymmetry can then be measured directly by fitting the analytic form of the differential cross-section to the acceptance corrected angular distribution.

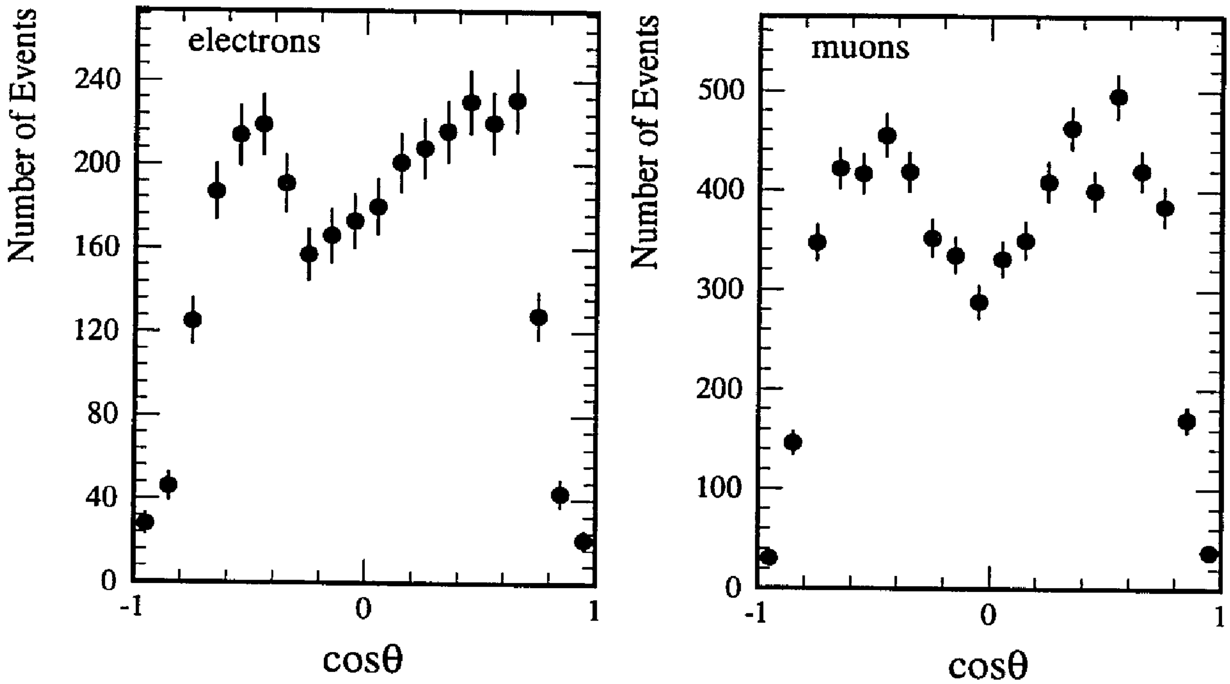

FIG. 5.15: The lepton-tagged thrust axis distribution for data with $p_T > 1$ GeV. No corrections have been applied.

The angular distribution of the data with $p_T > 1$ GeV before any corrections have been made is displayed in Fig. 5.15. Since there is no lepton detection in the forward region (endcap electron events have been excluded), the acceptance quickly falls off as the thrust axis approaches the beam pipe.

The acceptance for detecting prompt b decays in each bin was determined by comparing the selected lepton sample to the generated sample in the Monte Carlo simulation. To prevent a bias, the acceptance was symmetrized by averaging the bins at ±x. In Figure 5.16 the error bars indicate the acceptance before the symmetrization and the smooth curve shows the result of the symmetrization. The curve falls well within the statistical error of the unsymmetrized distribution. The muon acceptance dips near $\cos\theta = 0$ due to a 23 cm gap between the forward and backward halves of

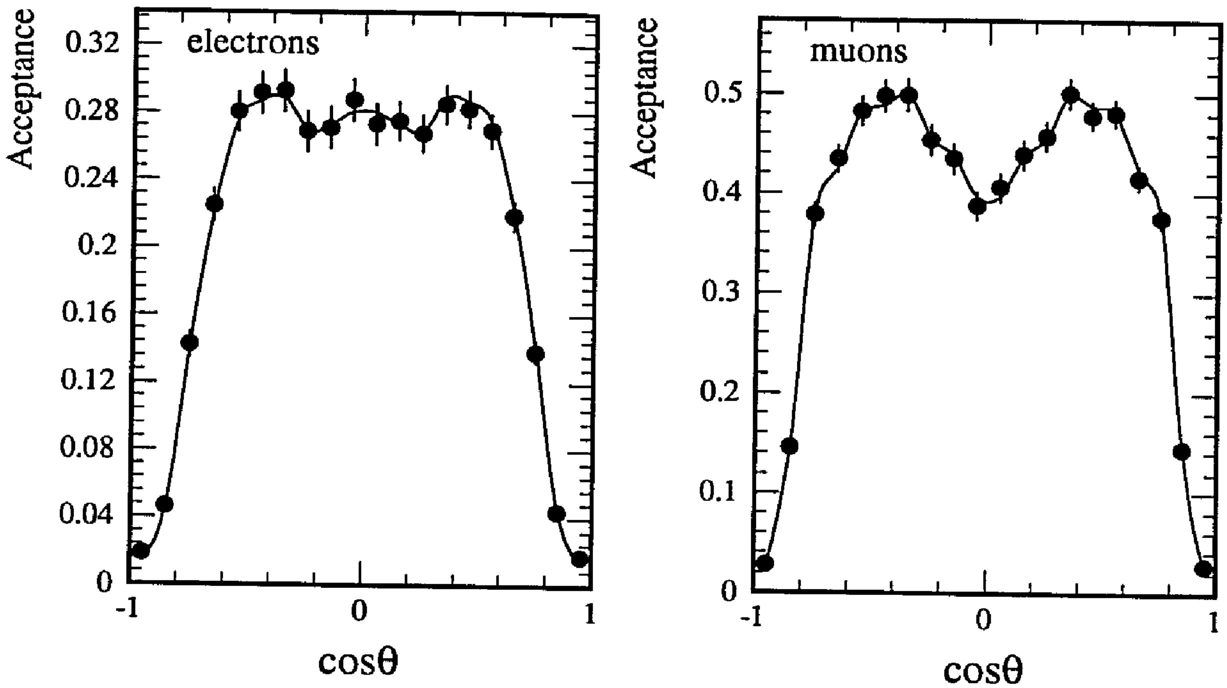

FIG. 5.16: Acceptance for prompt b decays ($b \rightarrow \ell$) as a function of $\cos\theta$ from Monte Carlo simulated events.

the muon chamber.

The number of background events (category 7) in each bin not associated with b or c quark decay was determined from the Monte Carlo and subtracted from the data, then each bin was divided by the acceptance. The shape of the remaining distribution is determined by the asymmetries of the tagged heavy quark decays. The fitted asymmetry of this distribution is related to the $\mathrm{b\bar{b}}$ and $\mathrm{c\bar{c}}$ asymmetries by

$$\frac{A^{\mathrm{fit}}}{1-2\epsilon} = (F_1' + F_2' + F_3' - F_4' + \eta F_5')A^{\mathrm{obs}}_{\mathrm{b\bar{b}}} - F_6' A_{\mathrm{c\bar{c}}}, \tag{5.4}$$

the F_k' being the relative fraction of category k remaining in the background subtracted sample. The parameter η, which is related to the charge correlation for nonleptonic b decays, was determined to be 0.317 ± 0.017 from the Monte Carlo.

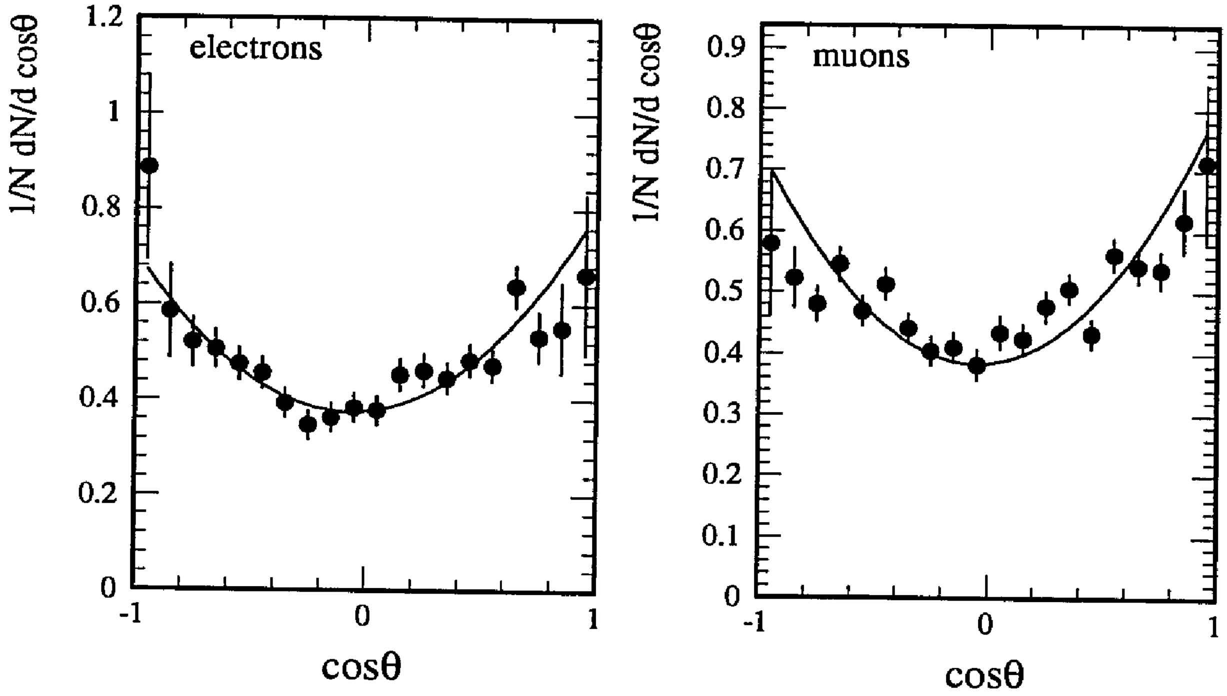

FIG. 5.17: Background subtracted and acceptance corrected data with $p_T > 1$ GeV. The smooth curves indicate the result of a fit to the function $f(x) = C\left[3/8(1+x^2) + A^{\rm fit}x\right]$.

The background subtracted, acceptance corrected distributions for electrons and muons are given in Fig. 5.17. The smooth curve indicates the result of a two parameter chisquare fit of the differential cross-section

$$\frac{1}{N}\frac{dN}{dx} = f(x) = C\left[3/8(1+x^2) + A^{\rm fit}x\right],$$

where the two parameters are the observed asymmetry $A^{\rm fit}$ and the normalization factor C. The b$\bar{\rm b}$ asymmetry was then extracted from the observed asymmetry by applying Eq. (5.4) and the results are recorded in Table 5.7. The electron result differs by about one standard deviation from the result obtained with the counting method (see Table 5.5). The difference is entirely due to fluctuations near $\cos\theta = 0$ which

Table 5.7: Asymmetry determined from the background subtracted, acceptance corrected thrust axis distribution for events with $p_T > 1$ GeV.

lepton	$A^{\mathrm{obs}}_{\mathrm{b\bar{b}}}$
μ	0.055 ± 0.020
e	0.056 ± 0.026
Total	0.055 ± 0.016

contribute a significant asymmetry in the counting method but not in the acceptance method. Since the form of the angular distribution is fixed, the acceptance method is less susceptible to fluctuations in a few bins.

Systematics

The various contributions to the systematic errors in the acceptance corrected measurement are listed in Table 5.8. Two contributions were added that did not appear in the counting method, namely that the effect of varying the correlation constant η

Table 5.8: Systematic errors for the acceptance method.

Contribution	value	variation(±)	$\Delta A^{\mathrm{obs}}_{\mathrm{b\bar{b}}}$
$\Gamma_{\mathrm{b\bar{b}}}$ (MeV)	378.0	2.5	0.0006
$\Gamma_{\mathrm{c\bar{c}}}$ (MeV)	313.4	5.2	0.0010
Br(b→ℓ)	0.117	0.006	0.0010
Br(c→ℓ)	0.096	0.006	0.0002
$\epsilon_b(x_E)$	0.05	0.01	< 0.0001
$\epsilon_c(x_E)$	0.50	0.10	0.0001
e charge confusion	0.013	0.010	0.0002
μ charge confusion	0.002	0.002	0.0002
$A_{\mathrm{c\bar{c}}}/A_{\mathrm{b\bar{b}}}$	0.7	0.3	0.0012
η	0.317	0.017	< 0.0001
bins	20	2	0.0005
p_T cut (GeV)	1.00	0.25	0.0058
MC statistics			0.0078
Total (quadrature)			0.0099

was negligible and that changing the number of bins in $\cos\theta$ had little effect. The location of the p_T cut proved to be much less critical than in the counting method, most likely due to the insensitivity of the acceptance method to fluctuations in the data.

The error associated with the Monte Carlo statistics was determined by adding in quadrature two contributions, one from the corrections to each bin in the angular distribution and one from the constants used in Eq. (5.4). The effect of the Monte Carlo statistics on the corrected angular distribution was calculated by including the error for the background subtraction and the acceptance correction in the error for each bin. This caused a corresponding increase in the parameter errors in the fit. Subtracting, in quadrature, the error due solely to the data statistics left the contribution from the Monte Carlo statistics. The second contribution was calculated analytically from Eq. (5.4) using the corresponding error on the constants determined from the Monte Carlo.

The total systematic error for the acceptance method is significantly lower than for the counting method and is dominated by the Monte Carlo statistics.

5.2.5 The Likelihood Method

Using the lepton momentum spectrum to determine which events are likely to be prompt b decays, once can extract the maximum statistical significance in determining the asymmetry from a maximum likelihood fit. The likelihood function is formed from the product of the probabilities, P, for observing each event in the data sample

$$L = \prod_i P(\bar{\mathrm{x}}_\mathrm{i}, A_{\mathrm{b\bar{b}}}), \tag{5.5}$$

where $\bar{\mathrm{x}}_\mathrm{i}$ is a set of experimental observables for event i. Maximizing L, or equivalently minimizing $-\log L$, determines the most likely value of $A_{\mathrm{b\bar{b}}}$. The event probability is obtained from a sum over the probabilities for observing an event of type k (see Table 5.4) with $x_i = \cos\theta_i$

$$P(\bar{\mathrm{x}}_\mathrm{i}, A_{\mathrm{b\bar{b}}}) = \sum_k P_k(\bar{\mathrm{x}}_\mathrm{i})\ f_k(x_i, A_k), \tag{5.6}$$

where P_k is the probability of producing event type k and f_k is the angular distribution $\frac{3}{8}(1+x^2)+A_k x$. A key advantage to using the likelihood method is that symmetrical detector inefficiencies in $\cos\theta$ do not affect the result of the minimization of the likelihood function. A short proof of this feature of the likelihood function can be found in the appendix, Section A.2

The probability P_k was determined by binning the data in terms of the experimental observables and counting the number of Monte Carlo events in the bin of that type. Various choices of observables and binning schemes will be investigated, but a simple check on the likelihood method itself can be performed by considering the entire sample as a single bin. The probability P_k is then just the fraction of events of type k in the sample. The close agreement between the results of the likelihood fit with one bin and $p_T > 1$ GeV compared to the acceptance method results can be seen in Table 5.9.

Table 5.9: Consistency check on the likelihood fit by using *one bin* and $p_T > 1$ GeV compared to the acceptance method. NOTE: this is not the best fit for the likelihood method.

lepton	$A_{b\bar{b}}^{obs}$ from	
	one bin fit	acceptance
e	0.057 ± 0.020	0.055 ± 0.020
μ	0.061 ± 0.026	0.056 ± 0.026
Total	0.059 ± 0.016	0.055 ± 0.016

The sensitivity of the event probability function to prompt b decays can be improved by including information about the momentum spectrum of the detected lepton. Since the leptons from prompt b decay tend to have higher values of p_T, which can be seen in Fig. 5.11, the category probability P_k was determined by binning the Monte Carlo in p_T and counting the number of events of each category in the bin. The p_T distributions for electrons and muons differ, especially with regard to the amount of background at low p_T values, so the probability P_k was calculated separately for the two types of leptons.

The question of how to bin the data in order to achieve the most precise result is difficult to answer in general. Small bin sizes are desirable to maximize the sensitivity to the shape of the sampled distribution. However, since the probability is determined from a finite number of Monte Carlo events, large bin sizes are desirable to reduce statistical fluctuations of the number of events in the bin.

To chose an appropriate bin size, a statistic was introduced that measures the sensitivity to the desired signal for a given choice of bins. A plot of the sensitivity as a function of the number of bins guides the choice of the optimal bin size. In addition, different bin variables can be compared based on their sensitivity function distribution. The sensitivity function is defined as

$$S(N_{\mathrm{bins}}) = \sqrt{\sum_{n}^{N_{\mathrm{bins}}} \frac{(F_n - \bar{F})^2}{\sigma_n^2}}, \tag{5.7}$$

where N_{bins} is the total number of bins, F_n is the fraction of signal events in bin n, $\bar{F}$ is the fraction of signal events in the entire sample, and σ_n is the statistical error of F_n. Varying the size of the bins affects the function S in two ways:

1. Bins with fractions very different from $\bar{F}$ contribute large values to S.
2. Bins with few events have large statistical errors which contribute small values to S.

Large values of the function S indicate that the signal is well separated from the background in the binning scheme. A few other observations about the function S should be made:

- S is exactly zero if $N_{\mathrm{bins}} = 1$.
- If the bin variable is a random number, then the sensitivity function monotonically increases with the number of bins. This is due to statistical fluctuations of F_n about $\bar{F}$; however, the slope is constant and small.
- If the number of bins is so large that each bin has only one (or zero) events in it, then S is no longer significant.

The sensitivity to prompt b decays obtained by making bins of equal size in the p_T distributions for electrons and muons in the Monte Carlo is displayed in Fig. 5.18. The average number of events in each bin is superimposed on the plots. The maximum

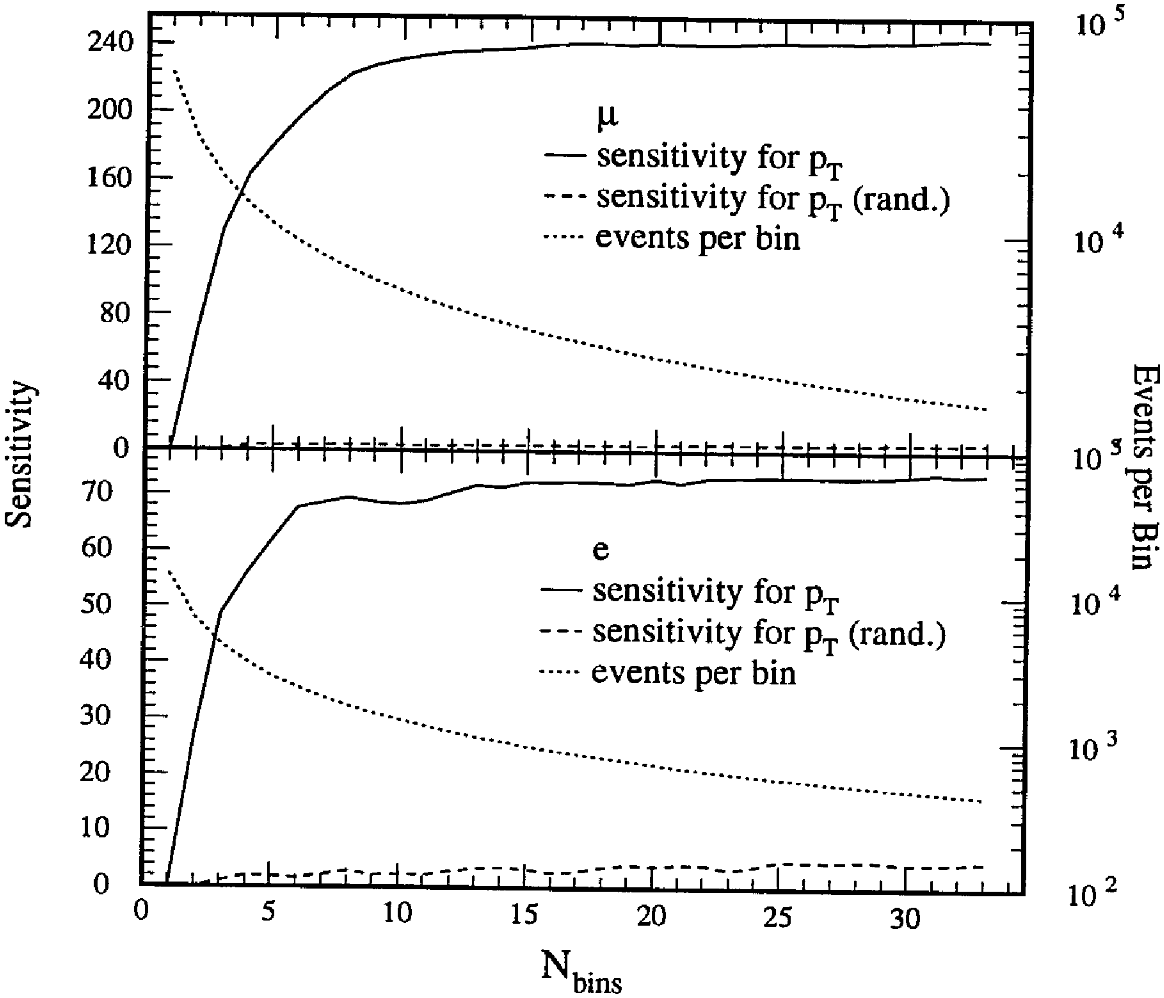

FIG. 5.18: Sensitivity to prompt b decays and average bin population for events binned in p_T. The sensitivity for events binned with p_T randomized is also indicated.

separation of prompt b from background is reached when the number of bins exceeds 10. The average bin population is quite high so S is meaningful for the entire plotted range. To verify that the sensitivity function is exploiting the difference between the p_T distributions of prompt b decays and background, S was also calculated after the p_T values of the Monte Carlo events were randomly reordered. The relative fractions of each event types therefore remained the same, but any information contained in the p_T distribution was lost. The sensitivity function results from the randomized p_T distribution are also indicated in Fig. 5.18. The plots confirm the expectations that the sensitivity to prompt b decays in the randomized variable does not improve by increasing the number of bins but that significant improvements are possible by binning the true p_T distribution.

Choosing N_{bins}= 15, the b$\bar{\mathrm{b}}$ asymmetry determined from a maximum likelihood fit to the 1991 data sample without a cut on p_T is given in Table 5.10. The change in the log of the likelihood as a function of the $A^{\mathrm{obs}}_{\mathrm{b\bar{b}}}$ is displayed in Fig. 5.19.

Table 5.10: Asymmetry determined from likelihood fit with no p_T cut.

lepton	$A^{\mathrm{obs}}_{\mathrm{b\bar{b}}}$
μ	0.053 ± 0.019
e	0.066 ± 0.026
Total	0.059 ± 0.015

Using the function S it can be shown that the sensitivity to prompt b decays increases by incorporating into the fit the energy of the nearest jet to the lepton (E_{jet}). A study of the effects on the analysis by including this information can be found in Appendix B. The study indicates that the error on $A^{\mathrm{obs}}_{\mathrm{b\bar{b}}}$ decreases by less than 2%

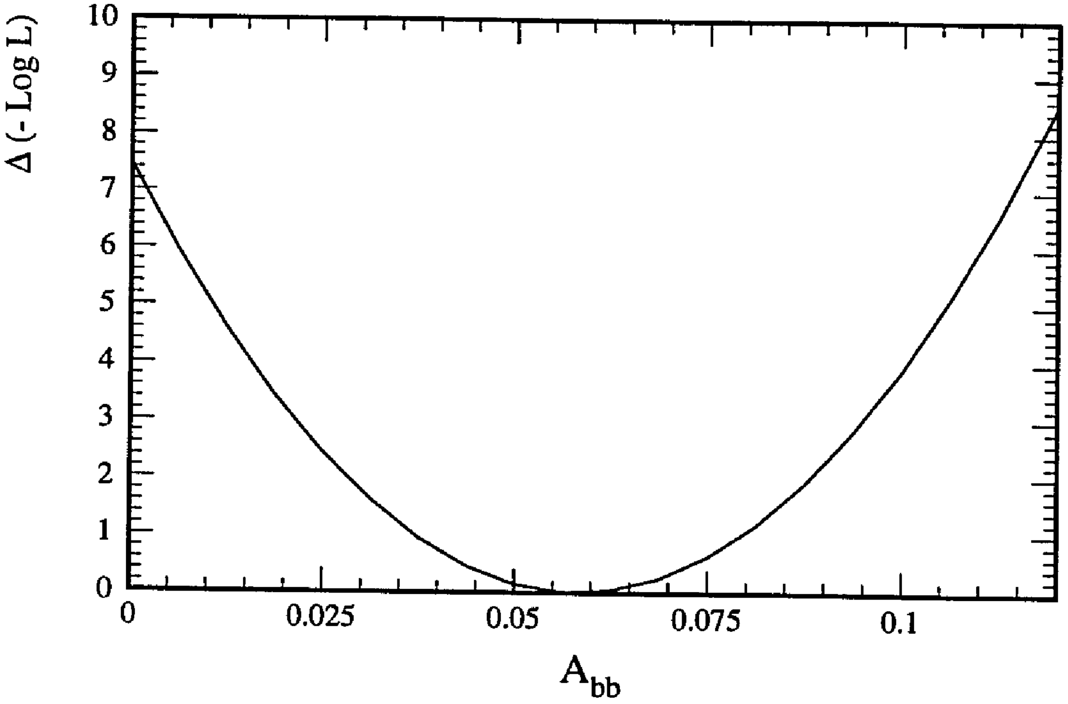

FIG. 5.19: Change in the log likelihood as a function of $A^{\mathrm{obs}}_{\mathrm{b\bar{b}}}$.

which is not significant enough to change the quoted error of 0.015. Therefore, E_{jet} is not employed for the final results.

Systematics

The contributions to the systematic error in the likelihood method binned in p_T are listed in Table 5.11. Varying the choice of the number of bins, N_{bins}, was the single greatest source of error. The background asymmetry, A_{back}, enters explicitly into the calculation of the likelihood function. A_{back} and its associated error were determined from the Monte Carlo, but the effect of varying it on the systematic error is small.

The error due to the finite Monte Carlo statistics was determined iteratively, by varying the number of events of each category in each bin by the square root of the number of events of that type ($n \pm \sqrt{x}$). The total error was calculated by adding, in

Table 5.11: Systematic errors for the likelihood method.

Contribution	value	variation(±)	$\Delta A^{\text{obs}}_{\text{b}\bar{\text{b}}}$
$\Gamma_{\text{b}\bar{\text{b}}}$ (MeV)	378.0	2.5	0.0005
$\Gamma_{\text{c}\bar{\text{c}}}$ (MeV)	313.4	5.2	0.0008
$\text{Br}(\text{b}\rightarrow\ell)$	0.117	0.006	0.0007
$\text{Br}(\text{c}\rightarrow\ell)$	0.096	0.006	0.0002
$\epsilon_b(x_E)$	0.05	0.01	0.0002
$\epsilon_c(x_E)$	0.50	0.10	0.0001
e charge confusion	0.013	0.010	0.0002
μ charge confusion	0.002	0.002	0.0002
$A_{\text{c}\bar{\text{c}}}/A_{\text{b}\bar{\text{b}}}$	0.7	0.3	0.0015
η	0.317	0.017	< 0.0001
A_{back}	0.0113	0.008	0.0001
Nbins	15	2	0.0021
MC statistics			0.0004
Total (quadrature)			0.0029

quadrature, the result of each iteration. Since the bin population was large, on the order of 10^3 events per bin, the total error due to Monte Carlo statistics was small.

The systematic error for the likelihood method is significantly smaller than for the acceptance and counting methods. The improvement comes mainly from eliminating the p_T cut and eliminating the Monte Carlo statistics error from the calculation of the acceptance.

5.3 The Mixing Measurement

5.3.1 Introduction

A direct measure of B^0-$\bar{B}^0$ mixing can be made from events in which both the b and $\bar{b}$ quark decayed semileptonically. In the absence of mixing, the two leptons will have opposite charges. However, if one of the b quarks oscillates into its charge conjugate before it decays, then the pair of leptons will have the same charge. Thus, like sign dilepton events indicate the presence of mixing.

Since the L3 detector can identify both electrons and muons in multi-hadronic events, there are three sets of lepton pairs that are accepted: ee, μe, and $\mu\mu$. The data sample was collected by applying the lepton selection criteria discussed in Chapter 4 and requiring that there be a pair of leptons with an opening angle of greater than 60°. If an event contained more than one pair of leptons that met this requirement, then the pair that had the maximum p_T was chosen. For data collected in 1991 the charge combination for each lepton pair type is displayed in Table 5.12. Electrons in the ECAL endcap were excluded because of the large amount of charge confusion in this region (see Section 5.1.3). For completeness, the total number of selected

Table 5.12: The 1991 data sample showing the number of events for each lepton and charge combination. Endcap electron events were excluded.

	no p_T cut			$p_T > 1$ GeV		
charges	ee	μe	$\mu\mu$	ee	μe	$\mu\mu$
$\ell^+\ell^+$	14	56	113	10	24	26
$\ell^-\ell^-$	8	64	86	5	29	26
$\ell^+\ell^-$	43	205	342	35	116	121
Total	65	325	541	50	169	173

electrons in the endcap region are given in Table 5.13.

Table 5.13: Total number of endcap electrons selected in 1991 data. Note that these are not used in the analysis. e′(e) denotes an endcap (barrel) electron.

p_T cut	e′e′	ee′	μe′
none	4	5	17
1 GeV	2	2	7

The composition of the selected dilepton data was estimated from Monte Carlo simulations and the major event categories are listed in Table 5.14. The sample is dominated by prompt b decays ($b \rightarrow \ell$); and making a cut on the p_T of both leptons further enhances the fraction of prompt b decays. Particles represented by X in the decay reactions are either leptons or charged tracks misidentified as leptons that originate from the decay of light hadrons (i.e. hadrons that do not contain a b or c quark). Event categories 1 through 6 are sensitive to B^0-$\bar{B}^0$ mixing which leads to

Table 5.14: Monte Carlo prediction of the composition of the selected dilepton sample in percent (%). The event categories display the lepton charge combination without B^0-$\bar{B}^0$ mixing. The event fractions include the charge conjugate of the listed process. Also, $b \rightarrow \ell^-$ includes the decays $b \rightarrow \bar{c} \rightarrow \ell^-$ and $b \rightarrow \tau^- \rightarrow \ell^-$; and X represents charged tracks that were misidentified as leptons and leptons from the decay of light hadrons.

k	Category		no p_T cut			$p_T > 1$ GeV		
			ee	μe	$\mu\mu$	ee	μe	$\mu\mu$
1	$b \rightarrow \ell^-$	$\bar{b} \rightarrow \ell^+$	70.9	55.6	37.4	78.9	77.4	73.2
2	$b \rightarrow \ell^-$	$\bar{b} \rightarrow \bar{c} \rightarrow \ell^-$	13.5	22.9	24.4	10.1	12.3	16.1
3	$b \rightarrow c \rightarrow \ell^+$	$\bar{b} \rightarrow \bar{c} \rightarrow \ell^-$	0.7	1.7	4.3	0.0	0.3	0.8
4	$b \rightarrow \ell^-$	$\bar{b} \rightarrow X$	12.4	12.2	11.0	10.3	8.1	7.7
5	$b \rightarrow c \rightarrow \ell^+$	$\bar{b} \rightarrow X$	1.7	2.8	3.7	0.8	0.9	1.0
6	$b \rightarrow X$	$\bar{b} \rightarrow X$	0.0	0.4	0.6	0.0	0.3	0.2
7	$c \rightarrow \ell^+$	$\bar{c} \rightarrow \ell^-$	0.0	1.6	7.5	0.0	0.2	0.5
8	X	X	0.8	2.7	11.2	0.0	0.5	0.7

nonzero probabilities for observing lepton charge combinations different from those listed in the table. Note that category 2, $b \rightarrow \ell^-$ $b \rightarrow \bar{c} \rightarrow \ell^-$, contains a prompt lepton and contributes like sign events even in the absence of mixing.

The mixing parameter, which is the probability that the charge of the detected lepton has changed sign due to B^0-$\bar{B}^0$ oscillation, for the decays in the various event categories is given in Table 5.15. The mixing parameter for $b \rightarrow X$ decay is related to χ via

Table 5.15: Mixing parameter for various decays.

mixing parameter	decay
χ	$b \rightarrow \ell^-$
χ	$b \rightarrow c \rightarrow \ell^+$
χ	$b \rightarrow \bar{c} \rightarrow \ell^-$
χ_X	$b \rightarrow X^-$
0	$c \rightarrow \ell^+$
0	X

$$\chi_X = (1 - \chi)(1 - c) + \chi c,$$

where c is the probability that the sign of the charged track X is correlated with the b quark. From studies of Monte Carlo simulated data, c was determined to be $c = 0.555 \pm\ 0.021$.

Two methods for determining χ will be considered. The first method uses the ratio of the number of like-sign events to the total (the counting method). To achieve the best precision with this method it is necessary to enhance the signal from prompt b decays by making a p_T cut. The second method uses a maximum likelihood fit to the entire data sample by assigning a probability to every event based on experimental observables for each lepton.

5.3.2 The Counting Method

The fraction of like-sign events in the dilepton sample can be used to extract the B^0-$\bar{B}^0$ mixing parameter χ. The combination of charges for a given lepton pair depends on the event category and the mixing parameter for each decay. If χ_1, χ_2 are the mixing parameters for the decay on each side of the event, then the probability that one of the charges changed sign due to mixing is

$$P_c(\chi_1, \chi_2) = (1 - \chi_1)\chi_2 + \chi_1(1 - \chi_2)$$

and the probability that neither (or both) charges changed sign is

$$P_s(\chi_1, \chi_2) = 1 - P_c(\chi_1, \chi_2) = (1 - \chi_1)(1 - \chi_2) + \chi_1\chi_2.$$

Using Monte Carlo simulated events to predict F_k, the fraction of events in the sample of category k, the ratio of like-sign events to the total takes the form

$$\begin{aligned} R &= P_c(\chi, \chi)(F_1 + F_3) + P_s(\chi, \chi)F_2 + P_c(\chi, \chi_X)F_4 \\ &\quad + P_s(\chi, \chi_X)F_5 + P_c(\chi_X, \chi_X)F_6 + P_8F_8, \end{aligned} \tag{5.8}$$

where P_8 is the probability that a background event results in a like-sign pair of leptons. The probability was determined to be $P_8 = 0.584 \pm 0.030$ from Monte Carlo events.

Eq. (5.8) must also be convoluted with the effect of charge confusion in the lepton identification. If ϵ_1, ϵ_2 are the probabilities for determining the wrong charge for each lepton, then the observed ratio of like-sign events is

$$R^{obs} = P_s(\epsilon_1, \epsilon_2)R + P_c(\epsilon_1, \epsilon_2)(1 - R).$$

Recall that the charge confusion for electrons and muons is different so that the above correction depends on the lepton type.

The results of applying the counting method to the data sample with various p_T cuts is recorded in Table 5.16. The smallest fractional error is attained by making a p_T cut at 1 GeV. For this p_T cut, the mixing parameter determined from each lepton category is displayed in Table 5.17.

Table 5.16: Mixing parameter χ from counting method combining all three dilepton channels (e e, μ e, $\mu\,\mu$) for various p_T cuts.

p_T cut (GeV)	χ	$\Delta\chi/\chi$
0.00	0.046 ± 0.031	0.676
0.25	0.058 ± 0.030	0.520
0.50	0.089 ± 0.029	0.324
0.75	0.094 ± 0.025	0.269
1.00	0.106 ± 0.024	0.226
1.25	0.093 ± 0.023	0.248
1.50	0.070 ± 0.025	0.355
1.75	0.078 ± 0.035	0.448
2.00	0.092 ± 0.045	0.494

Table 5.17: Mixing parameter from the counting method with $p_T > 1$ GeV for each dilepton category.

lepton pair	χ
$\mu\mu$	0.088 ± 0.036
μe	0.120 ± 0.037
ee	0.117 ± 0.062
Total	0.106 ± 0.024

Systematics

The contributions to the systematic error in the counting method are listed in Table 5.18. The listed value of each contribution is varied by the stated error and the observed change in χ is reported in the table.

Table 5.18: Systematic errors in the counting method.

Contribution	value	variation(±)	$\Delta\chi$
$\Gamma_{b\bar{b}}$ (MeV)	378.0	2.5	< 0.0001
$\Gamma_{c\bar{c}}$ (MeV)	313.4	5.2	0.0001
Br(b→ℓ)	0.117	0.006	0.0045
Br(c→ℓ)	0.096	0.006	0.0040
$\epsilon_b(x_E)$	0.05	0.01	0.0003
$\epsilon_c(x_E)$	0.50	0.10	< 0.0001
e charge confusion	0.013	0.010	0.0030
μ charge confusion	0.002	0.002	0.0010
p_T cut (GeV)	1.00	0.25	0.0061
c	0.555	0.021	0.0015
P_8	0.584	0.030	0.0001
MC statistics			0.0131
Total (quadrature)			0.0161

Changing the physics parameters $\Gamma_{b\bar{b}}$, $\Gamma_{c\bar{c}}$, Br(b→ℓ), and Br(c→ℓ) can alter the relative fractions of the different event categories. In this way uncertainties in the semileptonic branching ratios result in significant contributions to the systematic error.

The fragmentation parameters ϵ_b and ϵ_c change the shape of the lepton momentum spectrum. Since the counting method ignores this shape except for a cut on p_T, the effect of varying these parameters is small.

The systematic errors attributed to Monte Carlo statistics, P_8, and c were determined analytically for each dilepton set from the formula for R and the corresponding errors for F_k, P_8, and c. Uncertainty in the determination of the fractions F_k leads to the greatest contribution to the systematic error. The p_T cut also has a large effect on the error because of the variation in the amount of background allowed in the sample and because of the change in the number of accepted events.

5.3.3 The Likelihood Method

Instead of imposing a p_T cut to improve the sensitivity to prompt b decays, a maximum likelihood fit to all of the data can be performed that utilizes additional information to identify (in a probabilistic way) the type of decay of each event. The likelihood function is defined as the product over all of the data sample of the probability of observing each event as a function of the mixing parameter χ:

$$L = \prod_i P(\bar{\mathrm{x}}_\mathrm{i}, Q_i, \chi),$$

where $\bar{x}_i$ is a set of experimental observables for the event and Q_i is the charge combination of the lepton pair,

$$Q_i = \begin{cases} 1 & \text{(like-sign event)} \\ -1 & \text{(unlike-sign event).} \end{cases}$$

The probability for a given event can be determined from a sum over the probabilities for each event category introduced in Table 5.14. The event probability is then

$$P(\bar{x}, Q, \chi) = \sum_k P_k(\bar{x}) W_k(\chi, Q),$$

where P_k is the probability of producing event type k with observables $\bar{x}$, and W_k is the probability that category k produces the charge combination Q. All of the dependence on the mixing parameter is contained in W_k which has the form

$$W_k(Q) = \begin{cases} P_c(\chi_1^k, \chi_2^k) & (Q \neq Q^k) \\ P_s(\chi_1^k, \chi_2^k) & (Q = Q^k), \end{cases}$$

where χ_1^k and χ_2^k represent the mixing parameters for each lepton in the event for category k. For the background category $k = 8$, the weight is

$$W_8(Q) = \begin{cases} P_8 & (Q = 1) \\ 1 - P_8 & (Q = -1). \end{cases}$$

The function W_k does not include the effect of charge confusion. Since the charge of one or both of the leptons could be incorrectly determined, the probability W_k is replaced by the mixture

$$W_k \to P_s(\epsilon_1, \epsilon_2)W_k + (1 - P_s(\epsilon_1, \epsilon_2))(1 - W_k),$$

where ϵ_1 and ϵ_2 are the charge confusion parameters as before.

The probability functions P_k are determined from Monte Carlo events by binning them in terms of a set of observables and counting the number of events in the bin. Before investigating binning strategies one can perform a consistency check on the method itself. If all of the data is placed in one bin, then the distributions P_k become fixed fractions for each k and the fit becomes analogous to the counting method. The results of the likelihood fit with a single bin and $p_T > 1$ GeV compared to the counting results are displayed in Table 5.19. The two methods are in good agreement for each combination of leptons.

Table 5.19: Consistency check on the likelihood fit by using *one bin* with $p_T > 1$ GeV compared with the results from the counting method. Note that this is not the best fit for the likelihood method.

lepton pair	χ determined from	
	one bin fit	counting
$\mu\,\mu$	0.089 ± 0.036	0.088 ± 0.036
μ e	0.119 ± 0.036	0.120 ± 0.037
e e	0.117 ± 0.061	0.117 ± 0.062
Total	0.107 ± 0.024	0.106 ± 0.024

The p_T distributions for the leptons in the selected events are shown in Fig. 5.20. As was observed in the single lepton distributions used to measure the $b\bar{b}$ asymmetry,

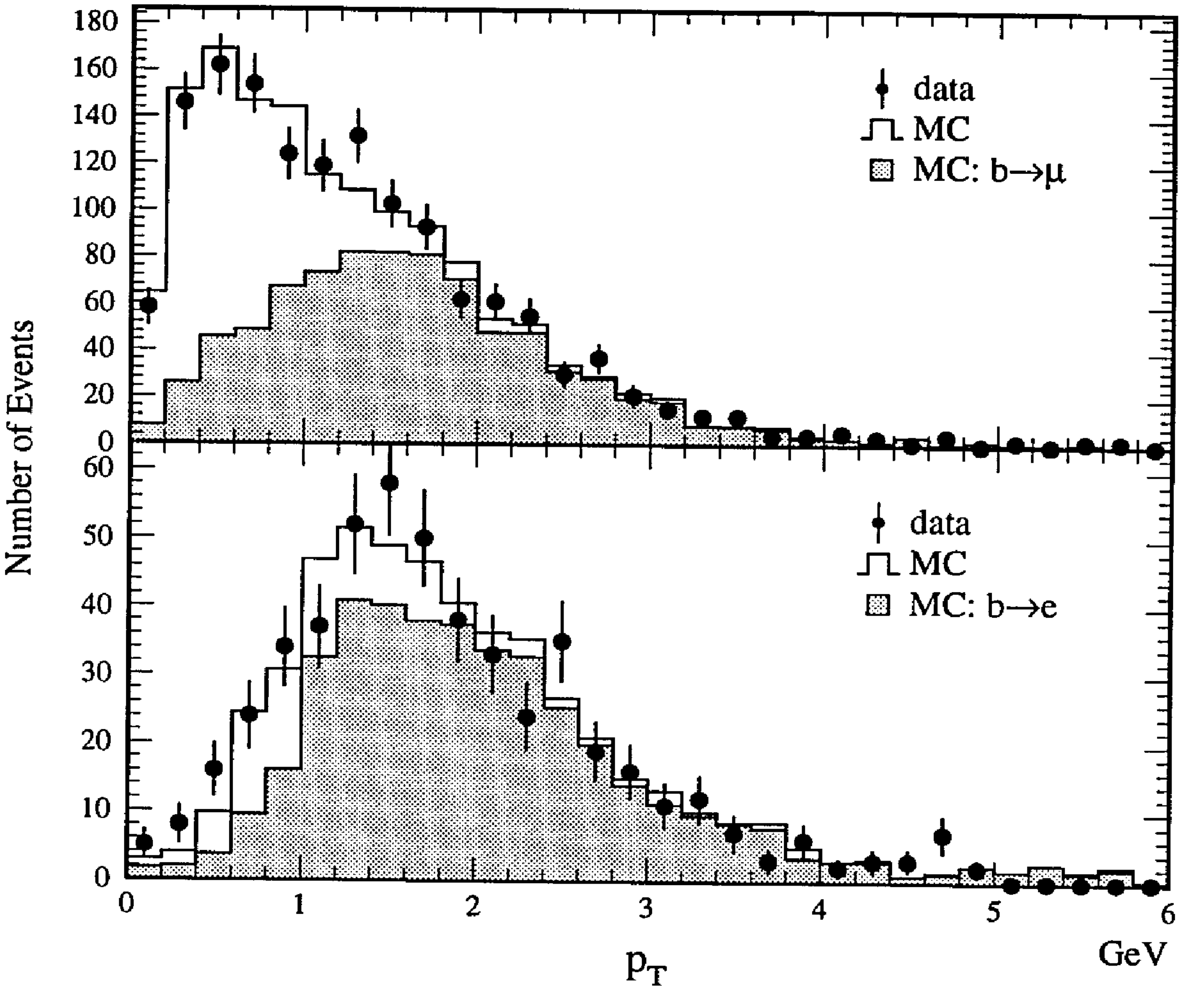

FIG. 5.20: Comparison between data and Monte Carlo p_T distributions for leptons from selected dilepton events.

leptons from prompt b decay cluster toward high values of p_T. This information can be exploited to distinguish prompt b decays from background by binning the Monte Carlo events and counting the number of events in each bin to determine the probabilities P_k.

The p_T distributions for the two leptons in an event are correlated (for example, given a high p_T lepton on one side of an event it is probable that the event is a b$\bar{\text{b}}$ event and therefore there is a high probability of detecting a high p_T lepton on the other side of the event). These correlations can be automatically accommodated by forming the joint probability $P_k(p_{T1}, p_{T2})$, which is calculated by binning in the two dimensional space formed by the p_T of each lepton.

Since the p_T distributions for electrons and muons are different, lepton 1 is defined to be the electron in μ e events. For the e e and $\mu\,\mu$ data samples the labeling of lepton 1 and 2 is chosen at random to avoid any systematic effect due to an accidental ordering of the two leptons.

The same problem concerning the choice of bin size arises as was encountered in the asymmetry fit but is even more crucial in this case since the size of the data sample is approximately 20 times smaller. As in the case of the asymmetry fit, the sensitivity function S described in Section 5.2.5 was employed here to determine the optimum bin size.

In order to apply the function S to the dilepton p_T distributions, a binning scheme must be chosen. Anticipating that the distributions will have a long, sparsely populated tail, the first bin division is placed such that a reasonably large number of

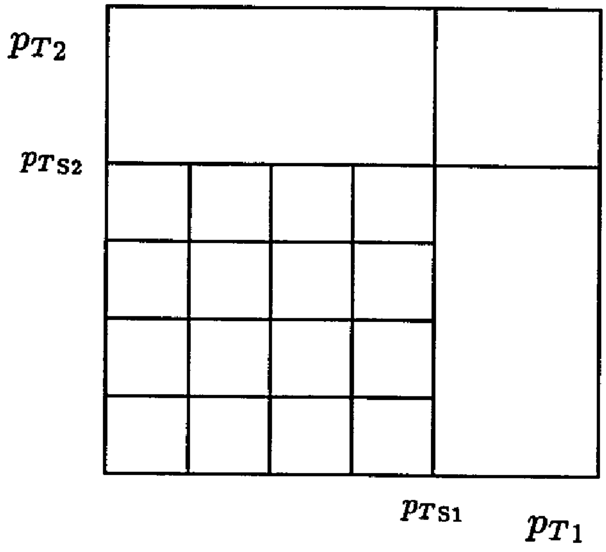

FIG. 5.21: General form of the binning scheme in the two dimensional space p_{T1} versus p_{T2}. In general, p_{TS1} does not have to be equal to p_{TS2}.

events will be found in that region. The remaining area of the two dimensional space is then divided into bins of equal size. A general diagram of this scheme is displayed in Fig. 5.21. The cutoffs for the tail are labeled p_{TS1} and p_{TS2}. The number of divisions on the p_T axis, j, is the same for both leptons ($j = j_1 = j_2$); the total number of bins is therefore $N_{\text{bins}} = j^2 + 3$.

The location of the cutoffs were selected such that there were approximately 150 Monte Carlo events in the bin. For muons the cutoff was 3.3 ± 0.2 and for electrons it was 3.5 ± 0.3. The quoted errors represent the region encompassing ± 50 events.

The sensitivity function S and the mean number of events per bin for various choices of j are displayed in Fig. 5.22. The sensitivity to prompt b decays quickly increases with the number of bins and then flattens out, reaching a maximum at about 28 bins ($j = 5$). The perceived increase in sensitivity in the e e sample above 40 bins is due to the sparseness of the Monte Carlo. Above 40, the bin population

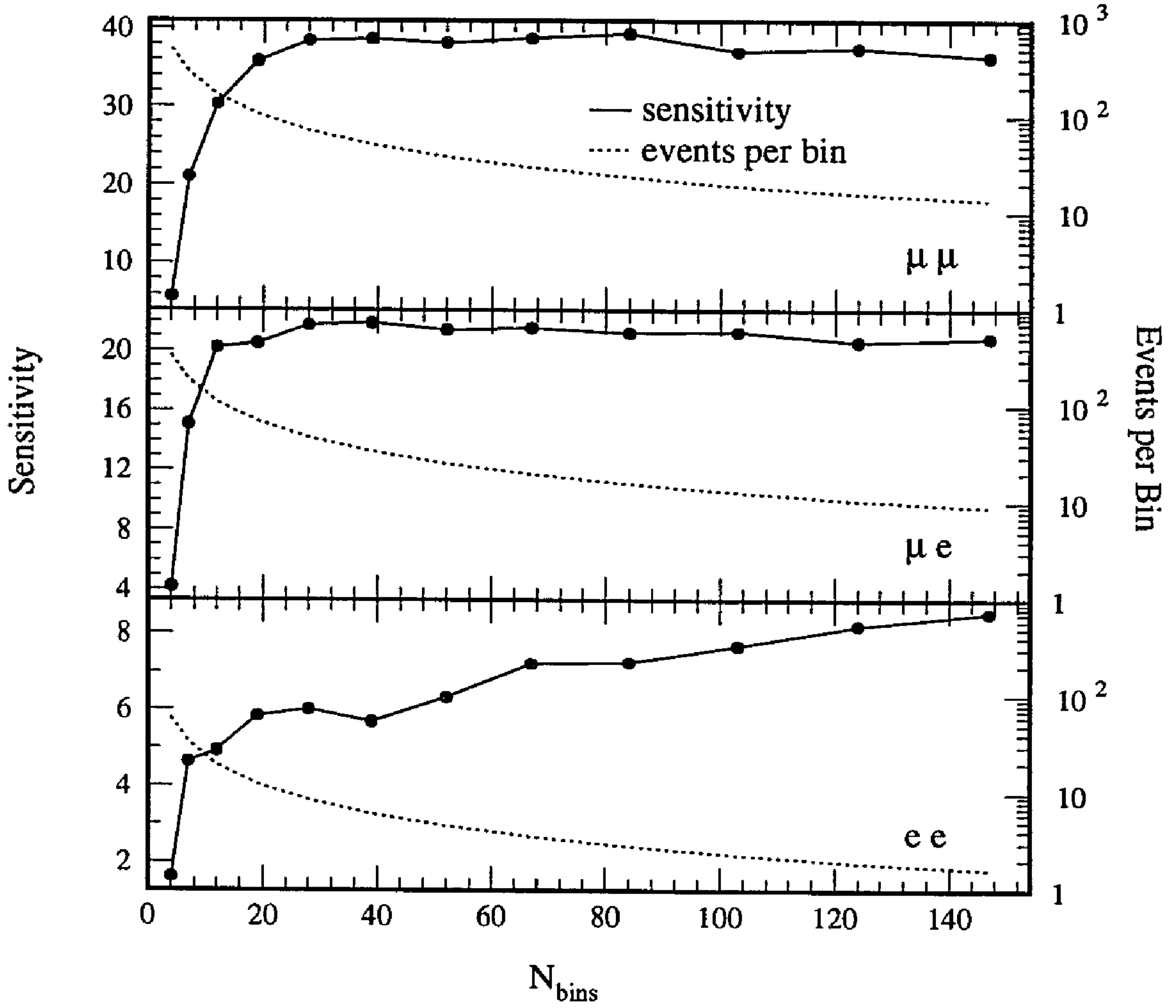

FIG. 5.22: Sensitivity function and average bin population for binning in p_T. The number of bins is $j^2 + 3$. The markers indicate the computed values of S at $(j = 1, 2, 3, \ldots)$ which were then connected by a straight line.

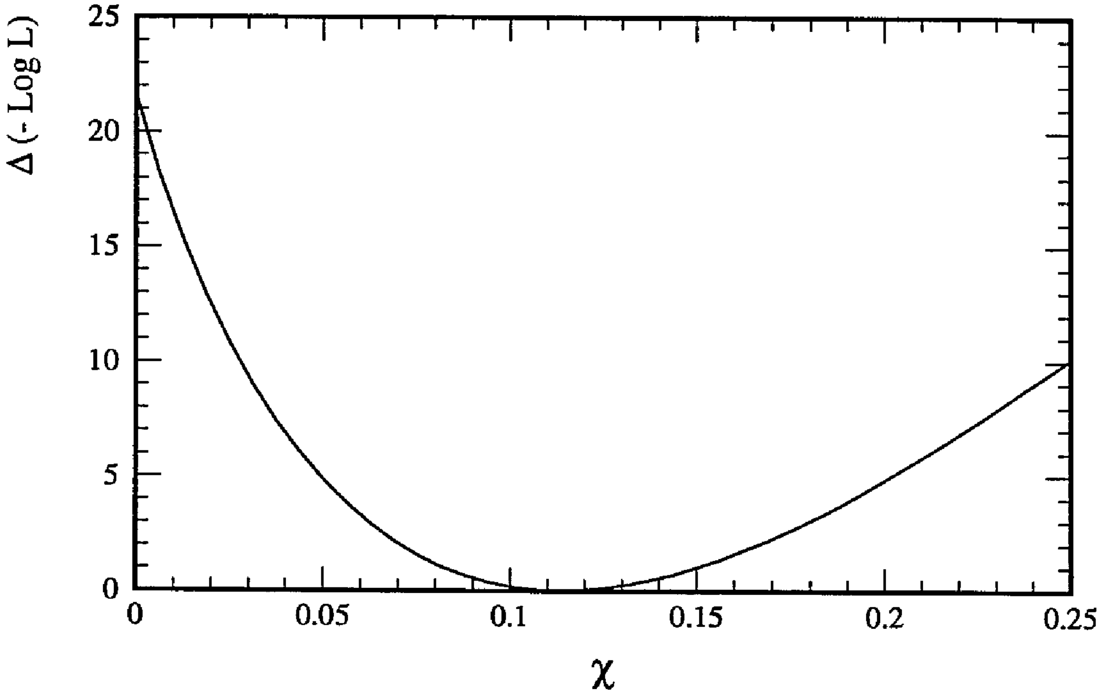

FIG. 5.23: Change in the log likelihood function for the mixing fit binned in p_T.

quickly approaches one and S reaches the limiting case in which each bin has either zero or one event. This region should therefore be avoided.

The results of the likelihood fit for χ choosing $j = 5$ are given in Table 5.20. The

Table 5.20: Maximum likelihood fit binned in p_T with $j = 5$ divisions.

lepton pair	χ
$\mu\,\mu$	0.073 ± 0.034
μ e	0.142 ± 0.038
e e	0.159 ± 0.067
Total	0.118 ± 0.024

shape of the log likelihood as a function of χ is plotted in Fig. 5.23. At the one standard deviation level, the error in χ is nearly symmetric.

As in the asymmetry measurement, the error on the mixing parameter can be reduced by including information about the energy of the nearest jet to each lepton

(E_{jet}). Appendix B describes the technique used to incorporate E_{jet} into the determination of the χ. The improvement in the error was found to be small, less than 3%, which does not warrant including E_{jet} in the final analysis.

Systematic Errors

The contributions to the systematic errors are listed in Table 5.21. To test the stability of the choice of binning scheme, the number of divisions j was varied by ±1 and the location of the p_T cutoff for electrons and muons were varied by their associated errors. These variations contributed significantly to the error since the average bin population is not large, often causing serious fluctuations of the number of events in the bins.

Table 5.21: Systematic errors in the likelihood method binned in p_T.

Contribution	value	variation(±)	$\Delta\chi$
$\Gamma_{b\bar{b}}$ (MeV)	378.0	2.5	< 0.0001
$\Gamma_{c\bar{c}}$ (MeV)	313.4	5.2	< 0.0001
Br(b→ℓ)	0.117	0.006	0.0023
Br(c→ℓ)	0.096	0.006	0.0016
$\epsilon_b(x_E)$	0.05	0.01	0.0009
$\epsilon_c(x_E)$	0.50	0.10	0.0002
e charge confusion	0.013	0.010	0.0038
μ charge confusion	0.002	0.002	0.0008
c	0.555	0.021	0.0012
P_8	0.584	0.030	0.0001
p_T cutoff e	3.5	0.3	0.0012
p_T cutoff μ	3.3	0.2	0.0020
j	5	1	0.0024
MC statistics			0.0098
Total (quadrature)			0.0115

The error due to the limited Monte Carlo statistics was calculated in the same way as the analogous error in the likelihood measurement of the asymmetry. An iterative procedure was performed that changed the number of Monte Carlo events for each category in each bin by its square root $(n \pm \sqrt{n})$. The value listed in the table is the sum, in quadrature, of the resulting change in $\mathcal{X}$ for each iteration.

The dominant systematic error in the likelihood method comes from the limited Monte Carlo statistics and is approximately half the size of the statistical error in the measurement of $\mathcal{X}$. This limitation is also manifest in the error associated with the choice of binning scheme.

5.4 Combined Results for 1990 and 1991

The detector configuration in 1990 was different from that in 1991. In particular, the BGO endcaps were not installed for the 1990 run, and for this reason, the energy resolution in the forward region was not as good. This affects the determination of the jet and thrust axes. Since these experimentally determined axes were used to calculate the event probabilities in the likelihood analyses, the 1990 and 1991 data were fitted separately.

For the barrel region of the detector the lepton selection criteria applied to 1990 and 1991 data were identical and the number of events that were selected is given in Table 5.22. In the dilepton events a minimum opening angle of 60° between the two leptons was required. The large increase in events in 1991 was due entirely to an increase in the integrated luminosity delivered by LEP.

Table 5.22: Number of selected events in the 1990 and 1991 running periods. Endcap electron events were excluded and no cut on p_T was made.

	Number of events		
	1990	1991	1990+1991
$q\bar{q}$	112727	294765	407492
$q\bar{q}+\mu$	5505	14795	20300
$q\bar{q}+e$	1298	3891	5189
$q\bar{q}+\mu\mu$	173	541	714
$q\bar{q}+\mu e$	97	325	422
$q\bar{q}+ee$	20	65	85

The results for the observed $b\bar{b}$ asymmetry ($A^{\mathrm{obs}}_{b\bar{b}}$) and the B^0-$\bar{B}^0$ mixing parameter (χ), determined from the data samples of each year, are given in Tables 5.23 and Table 5.24, respectively. The data were combined by adding the results of each

Table 5.23: The observed $b\bar{b}$ asymmetry from a maximum likelihood fit to the data binned in p_T.

lepton	$A^{\rm obs}_{b\bar{b}}$		
	1990	1991	1991+1990
μ	0.113 ± 0.031	0.053 ± 0.019	0.070 ± 0.016
e	0.009 ± 0.044	0.066 ± 0.026	0.052 ± 0.022
Total	0.077 ± 0.025	0.059 ± 0.015	0.063 ± 0.013

Table 5.24: Mixing parameter results determined from a maximum likelihood fit to the data binned in p_T.

lepton pair	χ		
	1990	1991	1991+1990
$\mu\mu$	0.104 ± 0.054	0.073 ± 0.034	0.081 ± 0.029
μe	0.155 ± 0.070	0.142 ± 0.038	0.145 ± 0.033
ee	0.275 ± 0.121	0.159 ± 0.067	0.186 ± 0.058
Total	0.147 ± 0.044	0.118 ± 0.024	0.125 ± 0.021

year in quadrature using the statistical errors only. The final results including the systematic errors that were determined in the previous sections are:

$$A^{\rm obs}_{b\bar{b}} = 0.063 \pm 0.013({\rm stat}) \pm 0.003({\rm syst})$$

and

$$\chi = 0.125 \pm 0.021({\rm stat}) \pm 0.012({\rm syst}),$$

where the first error is the statistical uncertainty and the second error is the systematic uncertainty. Correcting for B^0-$\bar{B}^0$ mixing, the asymmetry is

$$\boxed{A_{b\bar{b}} = 0.085 \pm 0.017({\rm stat}) \pm 0.004({\rm syst}).}$$

Chapter 6

Conclusion

The luminosity delivered to the L3 experiment in 1990 and 1991 was spread over a number of center-of-mass energies (see Fig. 6.1). Since the $b\bar{b}$ asymmetry is expected to vary with $\sqrt{s}$, the data were divided into three energy ranges: above, on, and below the Z resonance. The asymmetry for each of these samples corrected for B^0-$\bar{B}^0$ mixing is presented in Table 6.1.

Table 6.1: The $b\bar{b}$ asymmetry from the combined samples of 1990 and 1991 for three energy ranges.

$\sqrt{s}$(GeV)	$A_{b\bar{b}}$
89.72	$0.088 \pm 0.058 \pm 0.004$
91.25	$0.082 \pm 0.020 \pm 0.004$
92.81	$0.099 \pm 0.048 \pm 0.004$

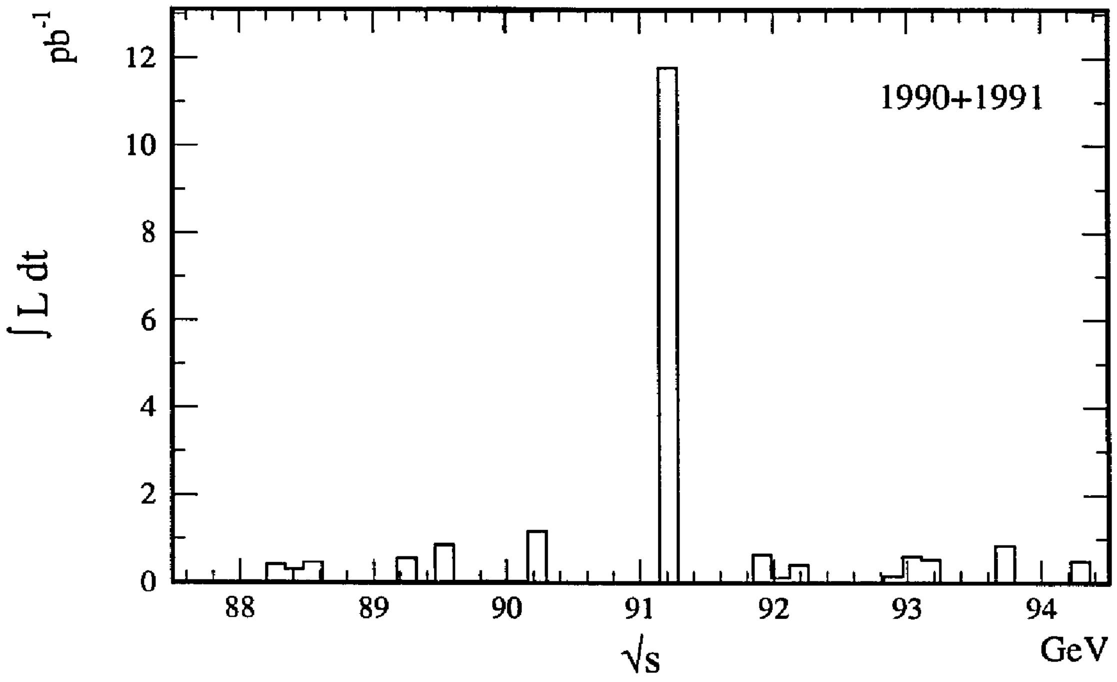

FIG. 6.1: Integrated luminosity delivered to the L3 experiment in 1990 and 1991.

6.1 Effective Couplings Fit

As was discussed in Section 2.2, the effective weak mixing angle $\sin^2\bar{\theta}_W$ can be extracted from the data without specifying a precise value for the top quark mass. This is possible because the electroweak radiative corrections, which depend on the mass of the top quark, can be separated from the QED corrections and absorbed into the definition of the fitted parameters. The effective couplings of the light fermions ($\mathrm{f} \neq \mathrm{b}$) to the Z are

$$g_\mathrm{A}^\mathrm{f} \equiv \sqrt{\rho} I_\mathrm{f}^3, \tag{6.1}$$

$$g_\mathrm{V}^\mathrm{f} \equiv \sqrt{\rho}(I_\mathrm{f}^3 - 2Q_\mathrm{f}\sin^2\bar{\theta}_W). \tag{6.2}$$

Extra sensitivity to vertex corrections involving the top quark for b$\bar{\mathrm{b}}$ final states alter the b parameters relative to the light fermions parameters, namely

$$\rho_{\mathrm{b}} \simeq \rho(1 - \tfrac{4}{3}\Delta\rho), \tag{6.3}$$

$$\sin^2\bar{\theta}_W^b = \sin^2\bar{\theta}_W R_{\mathrm{b}}, \tag{6.4}$$

where $R_{\mathrm{b}} \simeq 1 + \frac{2}{3}\Delta\rho$ and $\Delta\rho = (3G_F m_t{}^2)/(8\pi^2\sqrt{2})$. The effect of these additional corrections to the b$\bar{\mathrm{b}}$ asymmetry is minimal.

To extract $\sin^2\bar{\theta}_W$ from the data, the semi-analytic program ZFITTER 4.53 [78] was used to calculate the b$\bar{\mathrm{b}}$ asymmetry given the effective couplings to the Z and the measured parameters of the Standard Model. ZFITTER can calculate cross-sections and asymmetries of fermion pairs produced in e^+e^- annihilation, both in the framework of the Standard Model using the improved Born approximation and from a model-independent ansatz utilizing effective couplings. It includes electroweak radiative corrections to $\mathcal{O}(\alpha)$, higher order m_t-dependent corrections and gluonic QCD corrections up to $\mathcal{O}(\alpha_s^2)$. Cross-section calculations from ZFITTER were found to agree with the results of other programs [79, 80] to within 0.5%.

For the effective couplings fit, the Z mass and width were fixed to the values determined from L3 hadronic and leptonic cross-section data. The L3 measurements of m_Z and Γ_Z are [30]

$$m_Z = 91.115 \pm 0.006 \pm 0.007 \text{ (LEP) GeV}$$

$$\Gamma_Z = 2.490 \pm 0.010 \pm 0.005 \text{ (LEP) GeV},$$

where the error listed second is due to the uncertainty in the LEP beam energy. To calculate the small QCD corrections to the asymmetry, the strong coupling constant was set to the L3 measured value of $\alpha_s(m_Z{}^2) = 0.124 \pm 0.005$ [30]. The L3 result is a weighted average of α_s measured from the hadronic decay width of the τ lepton, the QCD correction to the hadronic Z width, and the jet topologies in hadronic events.

Fitting $\sin^2\bar{\theta}_W$ to the three measured values of $A_{b\bar{b}}$ by defining the effective couplings through Eqs. (6.1)-(6.4) resulted in

$$\boxed{\sin^2\bar{\theta}_W = 0.2336 \pm 0.0032.}$$

The asymmetry as a function of the center-of-mass energy for this value of $\sin^2\bar{\theta}_W$ is given in Fig. 6.2. In the fit ρ, ρ_b and R_b were fixed to their Standard Model values at $m_t = 90$ GeV and $m_H = 300$ GeV; however, the result of the fit was nearly independent of the choice of these parameters. Varying m_t from 90 GeV to 250 GeV changed the fitted value of $\sin^2\bar{\theta}_W$ by less than 0.0001, and the effect from varying the Higgs mass in the range 60-1000 GeV was smaller than 20 parts per million.

6.2 Standard Model Fit

An alternate approach to determine $\sin^2\bar{\theta}_W$ is to use the Standard Model to calculate the radiative corrections to the b$\bar{\text{b}}$ asymmetry by choosing a value for the top quark

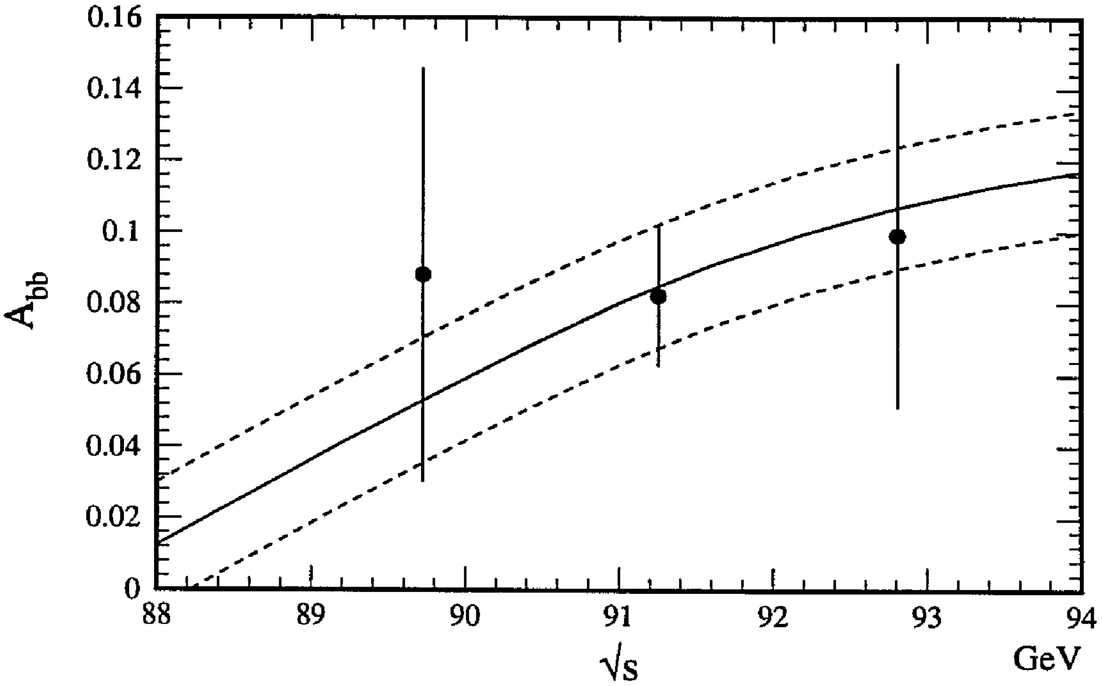

FIG. 6.2: The data points are the measured values for $A_{b\bar{b}}$. The solid curve represents the result of the effective couplings fit ($\sin^2\bar{\theta}_W = 0.2336 \pm 0.0032$), and the dashed curves show the one standard deviation errors from the fit.

and Higgs mass. The effective weak mixing angle is then treated as a derived quantity. Using the Standard Model branch of the ZFITTER program, four input parameters must be specified: the Z, top and Higgs masses, and α_s. Fixing the Z mass and α_s to the L3 measured values and choosing a Higgs mass of 300 GeV leaves only one free parameter in the fit, the mass of the top quark.

Fitting the top mass in the framework of the Standard Model resulted in

$$m_t = 124^{+91}_{-107}\ {}^{+22}_{-35}\ \text{(Higgs) GeV},$$

where the second error corresponds to varying the Higgs mass from 60-1000 GeV.

This value of the top mass corresponds to an effective weak mixing angle of

$$\sin^2\bar{\theta}_W = 0.2336^{+0.0024}_{-0.0033}.$$

The effect on $\sin^2\bar{\theta}_W$ of varying the Higgs mass was negligible. This measurement alone does not provide a strong constraint on the top quark mass; however, in terms of $\sin^2\bar{\theta}_W$ the measurement closely agrees with the result using effective couplings.

It should be remarked that the direct lower bound on the top quark mass is $m_t > 91$ GeV (95% CL) from CDF [81], which excludes nearly half of the one standard deviation error region determined from the $A_{b\bar{b}}$ data. The CDF limit, however, is only reliable for standard decay modes of the top. In certain situations of supersymmetric extensions of the Standard Model, the branching ratios of these decays would be suppressed and therefore the top quark would not be detected by the Fermilab collider experiments (CDF and D0). In contrast, the predictions from radiative corrections at LEP are completely independent of the top decay branching ratios. It is conceivable that in the near future, the limit on the top mass from CDF and D0 could be extended above the preferred value from LEP. If an unambiguous signal for the top quark fails to materialize at Fermilab, then this could be the first hint of physics beyond the Standard Model.

6.3 Comparison of L3 Measurements of $\sin^2\bar{\theta}_W$

A more stringent test of the Standard Model can be made by comparing values of the effective weak mixing angle determined from measurements that are sensitive to different couplings. In addition to the result from the $\mathrm{b\bar{b}}$ asymmetry, three other measurements of $\sin^2\bar{\theta}_W$ have been made with the L3 detector using the leptonic forward-backward asymmetry ($A_{\ell^+\ell^-}$), the tau polarization (P_τ) and the leptonic width of the Z (Γ_ℓ). Of these measurements, only Γ_ℓ, determined from the leptonic cross-sections, requires knowledge of the luminosity. The luminosity independence of the asymmetries and tau polarization simplify the analysis considerably.

In the improved Born approximation near the Z resonance, $\sin^2\bar{\theta}_W$ is related to these measurements in the following way:

$$\begin{aligned}
A_{\mathrm{b\bar{b}}} &= \tfrac{3}{4} A_{\mathrm{e}} A_{\mathrm{b}} \\
A_{\ell^+\ell^-} &= \tfrac{3}{4} A_{\mathrm{e}} A_{\ell} \\
P_\tau &= -A_\tau \\
\Gamma_\ell &= \frac{\sqrt{2} G_F m_Z{}^3}{12\pi} ({g_{\mathrm{A}}^{\mathrm{f}}}^2 + {g_{\mathrm{V}}^{\mathrm{f}}}^2),
\end{aligned}$$

where $A_{\mathrm{f}} = 2 g_{\mathrm{V}}^{\mathrm{f}} g_{\mathrm{A}}^{\mathrm{f}} / ({g_{\mathrm{V}}^{\mathrm{f}}}^2 + {g_{\mathrm{A}}^{\mathrm{f}}}^2)$. Figure 6.3 displays the value of $\sin^2\bar{\theta}_W$ for each of these measurements obtained from an effective coupling fit as in Section 6.1. Since the measurements depend on the neutral couplings and radiative corrections to different fermions, any flavor-dependent physics beyond the Standard Model could lead to an observable change in $\sin^2\bar{\theta}_W$. Each value in Fig. 6.3 has been measured with good

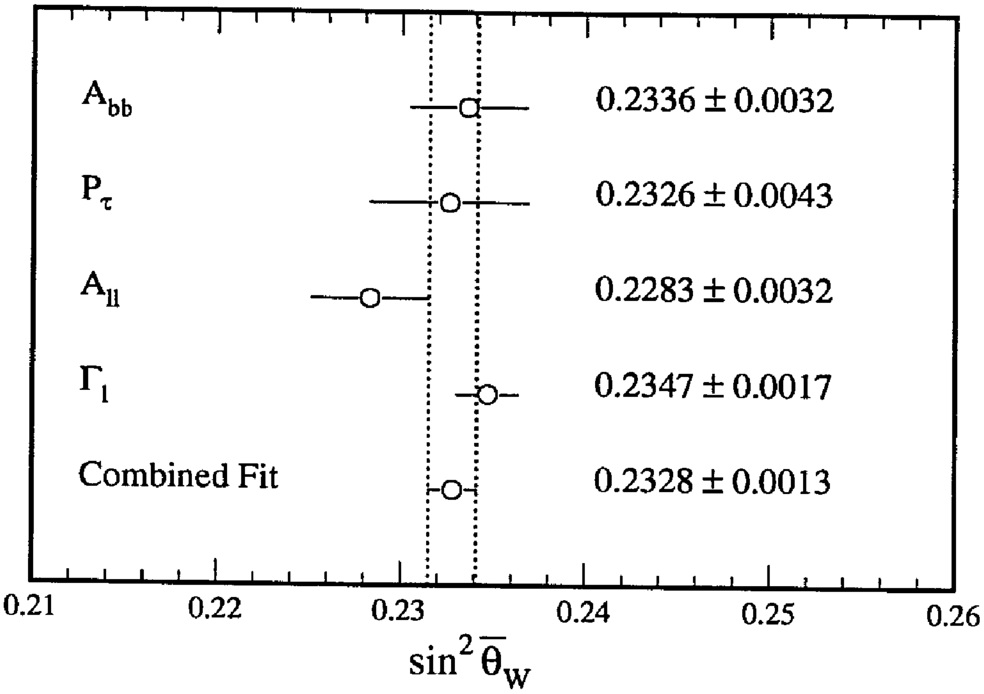

FIG. 6.3: Comparison of L3 measurements of $\sin^2\bar{\theta}_W$ using data collected in 1990 and 1991.

precision and no deviation from the Standard Model has been observed.

6.4 The Past

Previous measurements of $A_{b\bar{b}}$ date back to 1984 by experiments at PETRA at center-of-mass energies of around 35 GeV [21, 82–87]. Since that time, measurements have been reported by experiments at PEP [88–91] and the AMY collaboration at TRISTAN [92, 93]. All of these measurements, corrected for B^0-$\bar{B}^0$ mixing using the L3 value, are plotted in Fig. 6.4. The result of the Standard Model fit to the L3 result extrapolated down to lower energy is also displayed in the figure. Until LEP, all measurements were below $\sqrt{s} = 60$ GeV. There are two main consequences of attempting to measure the $b\bar{b}$ asymmetry at low energy: low statistics and low sensitivity to

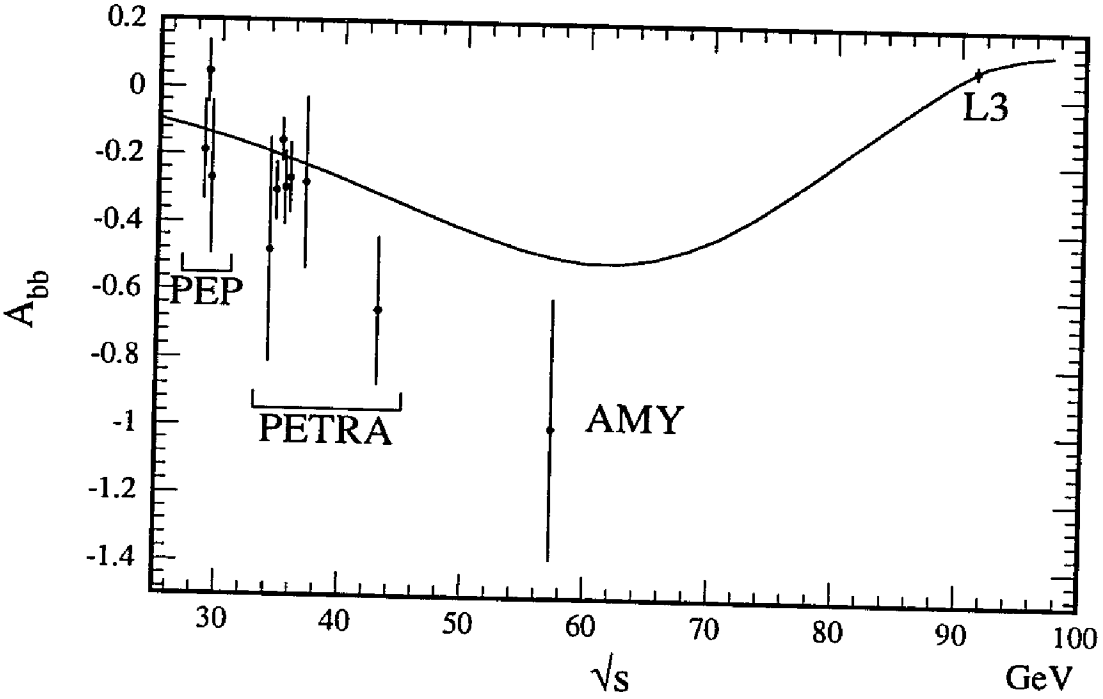

FIG. 6.4: Standard Model fit of $A_{b\bar{b}}$ from L3 extrapolated to lower energy, including the effects of QED, QCD and weak corrections. The value of $\sqrt{s}$ for some of the PEP and PETRA measurements was shifted by up to 0.5 GeV to improve the clarity of the plot. All measurements use the L3 value for B^0-$\bar{B}^0$ mixing.

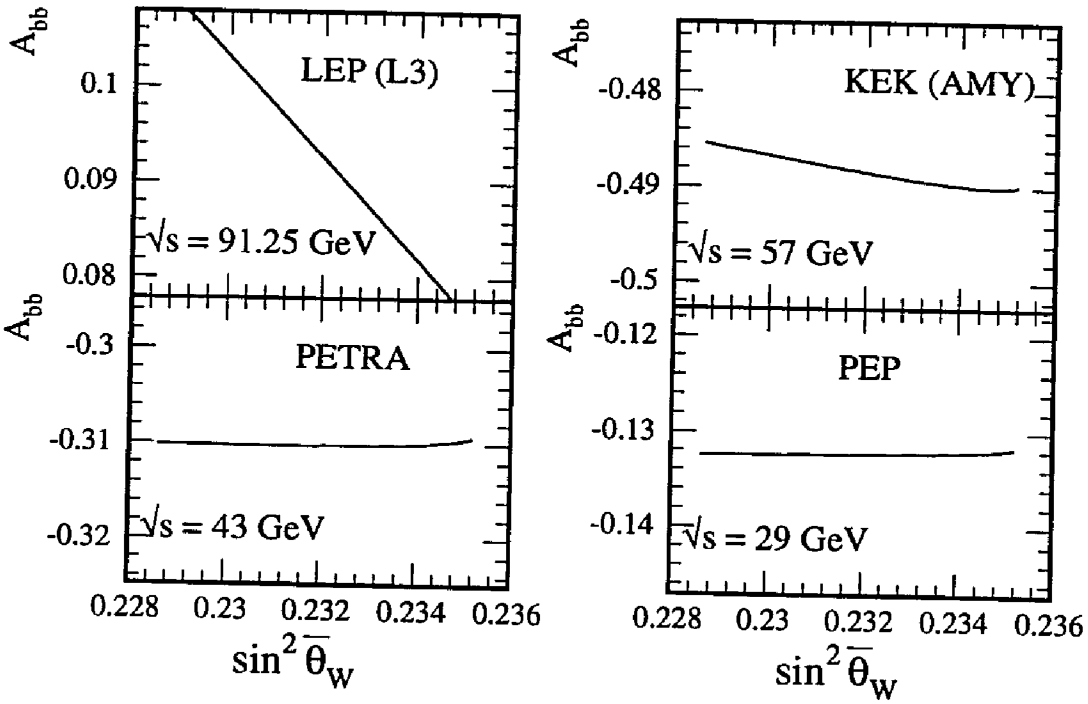

FIG. 6.5: $A_{b\bar{b}}$ as a function of $\sin^2\bar{\theta}_W$ for various values of $\sqrt{s}$. The divisions on each plot are the same size so that the slopes of the different distributions can be directly compared.

$\sin^2\bar{\theta}_W$.

The $b\bar{b}$ cross-section in the region $\sqrt{s}$ = 30-80 GeV is more than two orders of magnitude smaller than the peak cross-section at $\sqrt{s} = m_Z$, which results in a proportional reduction in data for a given amount of luminosity. For example, the AMY experiment collected 186 muon-tagged $b\bar{b}$ events from 33.3 pb^{-1} of integrated luminosity produced at an average center-of-mass energy of 57.2 GeV, while L3 collected more than 20,000 muon events with less than 20 pb^{-1} near the Z resonance.

The sensitivity of $A_{b\bar{b}}$ to $\sin^2\bar{\theta}_W$ in the region of interest for different center-of-mass energies is shown in Fig. 6.5. The divisions on each plot are the same so that the slope, which indicates the sensitivity, of each distribution can be directly compared. The slope at LEP energies is nearly 8 times steeper than at TRISTAN and the slope at PEP and PETRA energies are effectively zero.

Below the Z peak, the $b\bar{b}$ asymmetry originates from the interference between the photon and Z exchange diagrams, which only depends on the fermion charges and weak axial-vector couplings (see Section 2.2). On and above the peak, the Z exchange term, which depends on the weak vector couplings, dominates the asymmetry. This is clearly demonstrated in Fig. 6.5, since it is through the vector couplings that the sensitivity to $\sin^2\bar{\theta}_W$ enters. Thus, the LEP measurements are the first direct observation of the vector couplings of b quarks to the Z.

The PEP and PETRA measurements are consistent with the Standard Model but are not particularly sensitive to the weak mixing angle. The AMY measurement is hampered by extremely low statistics and does not provide a very reliable check on the LEP result.[1] The center-of-mass energy of TRISTAN is limited to about 60 GeV and barring orders of magnitude improvement in the luminosity, it is unlikely that AMY could probe the weak vector couplings.

6.5 The Future

The results presented here were derived from a sample of approximately 400,000 Z decays. In 1992 another 600,000 events were recorded and expectations are for an additional 1 million events in 1993. Since the relationship between $A_{b\bar{b}}$ and $\sin^2\bar{\theta}_W$ is approximately linear, an improvement in the asymmetry error will translate into

---

[1] Previous comparisons of the AMY results to the Standard Model [92, 93] did not include the effects of B^0-$\bar{B}^0$ mixing or radiative corrections. Both effects tend to increase the discrepancy between their result and the Standard Model.

a proportional improvement in the error on the weak mixing angle. Thus with two million events at the end of 1993 the statistical error on $\sin^2\bar{\theta}_W$ from $A_{b\bar{b}}$ could be cut in half to ~ 0.0015.

The bulk of the systematic errors on the measurement of $A_{b\bar{b}}$ are related to the amount of simulated data used to determine the composition of the selected data sample. In principle this is limited only by computing power. Upgrades of the existing computing facilities have been proposed and the production of simulated data is expected to keep pace with the increased luminosity provided by LEP.

A significant contribution to the systematic error is due to uncertainty in the fragmentation and semileptonic branching ratios of b quarks. Since these parameters can be measured with LEP data [30, 52], increased statistics will lead to improved values and thus smaller systematic errors.

It is clear that, in the near future, a significant increase in the amount of data will lead to more stringent tests of the Standard Model, but the current results indicate that any possible deviation will be small. In the far future, with ultrahigh statistics on the order of 10-100 million Z's and a reasonably well measured mass for the top quark (from the Fermilab experiments), the electroweak corrections observed through $\sin^2\bar{\theta}_W$ could begin to place bounds on the Higgs mass (see Appendix C).

Appendix A

Proofs

A.1 Observed Asymmetry Proof

Proof that the observed asymmetry is proportional to the full asymmetry for a detector acceptance function that is symmetric in $\cos\theta$.

The normalized differential cross-section is

$$\frac{1}{\sigma}\frac{d\sigma}{dx} = f(x) = \frac{3}{8}(1+x^2) + Ax, \tag{A.1}$$

where $x = \cos\theta$ and A is the asymmetry. This can be written as the sum of a symmetric and antisymmetric function of x,

$$f(x) = f^+(x) + Af^-(x),$$

where $f^+(x) = 3/8(1+x^2)$ and $f^-(x) = x$. The observed asymmetry is the convolution of this angular distribution with the acceptance, $a(x)$, of the detector

$$A^{\text{obs}} = \frac{\int_0^1 a(x)f(x)dx - \int_{-1}^0 a(x)f(x)dx}{\int_0^1 a(x)f(x)dx + \int_{-1}^0 a(x)f(x)dx},$$

which can be rewritten

$$A^{\text{obs}} = \frac{\int_0^1 \{a(x)f(x) - a(-x)f(-x)\}dx}{\int_0^1 \{a(x)f(x) + a(-x)f(-x)\}dx}.$$

If the acceptance is symmetric about x, $a(-x) = a(x)$, then

$$A^{\text{obs}} = \frac{\int_0^1 2a(x)Af^-(x)dx}{\int_{-1}^1 2a(x)f^+(x)dx}.$$

The asymmetry can now be factored out of the integral

$$A^{\text{obs}} = cA,$$

$$c = \frac{\int_0^1 a(x)f^-(x)dx}{\int_0^1 a(x)f^+(x)dx}.$$

Note that c is completely independent of A.

A.2 Likelihood Function Proof

Proof that the minimum of the likelihood function with respect to the asymmetry is independent of the detector acceptance, if the acceptance is symmetric in $\cos\theta$.

The likelihood function constructed from the normalized differential cross-section given in Eq. (A.1(is

$$L = \prod_i f(x_i), \tag{A.2}$$

where the product extends over all of the events. The true probability of observing an event for a given x is the convolution of $f(x)$ with the detector acceptance $a(x)$.

$$f'(x) = \frac{f(x)a(x)}{\int_{-1}^{1} f(x)a(x)dx}.$$

If the acceptance is symmetric, then

$$f'(x) = f(x)\left(\frac{a(x)}{\int_0^1 f^{+}(x)a(x)dx}\right) = D(x,a).$$

The function $D(x,a)$ depends on the acceptance but is independent of the asymmetry. The likelihood function obtained from $f'(x)$ is related to Eq. (A.2) through D:

$$L' = \prod_i f'(x_i) = L\prod_i D(x_i,a).$$

Thus L and L' differ by a multiplicative constant that does not depend on A, so the minimization of the likelihood L or L' will yield the same result.

The minimum of L' with respect to the asymmetry A occurs at

$$\frac{dL'}{dA} = 0.$$

Since

$$\frac{dL'}{dA} = \frac{dL}{dA} \prod_i D(x_i, a),$$

as long as the detector is turned on, i.e. $\prod_i D(x_i, a) \neq 0$, then the same value of A minimizes both L and L'.

Appendix B

Likelihood Fits Using E_{jet}

B.1 Introduction

The likelihood method used in the analysis of the $b\bar{b}$ asymmetry and B^0-$\bar{B}^0$ mixing in Chapter 5 is extremely versatile because a variety of detector information can be incorporated into the determination of the event probabilities P_k. This appendix explores the effect of introducing additional information in the form of E_{jet}, the energy of the nearest jet to the selected lepton, into the event probability calculation. The extra information enhances the discriminatory power of the probability function, which leads to smaller statistical errors.

The following section describes the definition of E_{jet} and how it relates to semileptonic b decay. The remaining sections give in detail the results of including E_{jet} information in the asymmetry and mixing measurements.

B.1.1 Jet Energy: E_{jet}

The neutrino associated with the semileptonic decay of a heavy quark passes through the detector without being observed. The measured energy of heavy quark jets (that decay semileptonically) is therefore lower than the energy of light quark jets. The hard fragmentation of the heavy quarks imparts a large boost to its decay products, which on average increases the amount of energy carried off by the neutrino and thereby further reduces the observed jet energy. As was shown in Section 5.1.2, the jet closest to the selected lepton, E_{jet}, is an experimental observable that is a good approximation of the heavy quark jet.

An accurate calculation of the jet energy is required to utilize the effect of missing energy to identify heavy quark jets. The response of the calorimeter depends on the type of charged particle that passes through it, so to determine the total energy of a jet a set of calibration constants is used that depends on the overall character of the jet. The algorithm used in this analysis combines the raw (i.e. uncorrected) energy from nine calorimeter regions using nine calibration constants. A gross determination of the character of the jet, based on the sum of raw energy in the hadronic and electromagnetic calorimeters, is used to choose among three sets of calibration constants: hadronic, electromagnetic and mixed. Since the showering plates in the hadron calorimeter are parallel to the beam pipe, the thickness of the calorimeter traversed by a particle originating from the interaction vertex depends on the polar angle of the track and therefore an angle-dependent correction is also applied.

Figure B.1 shows the 1991 data and Monte Carlo distributions of the energy of

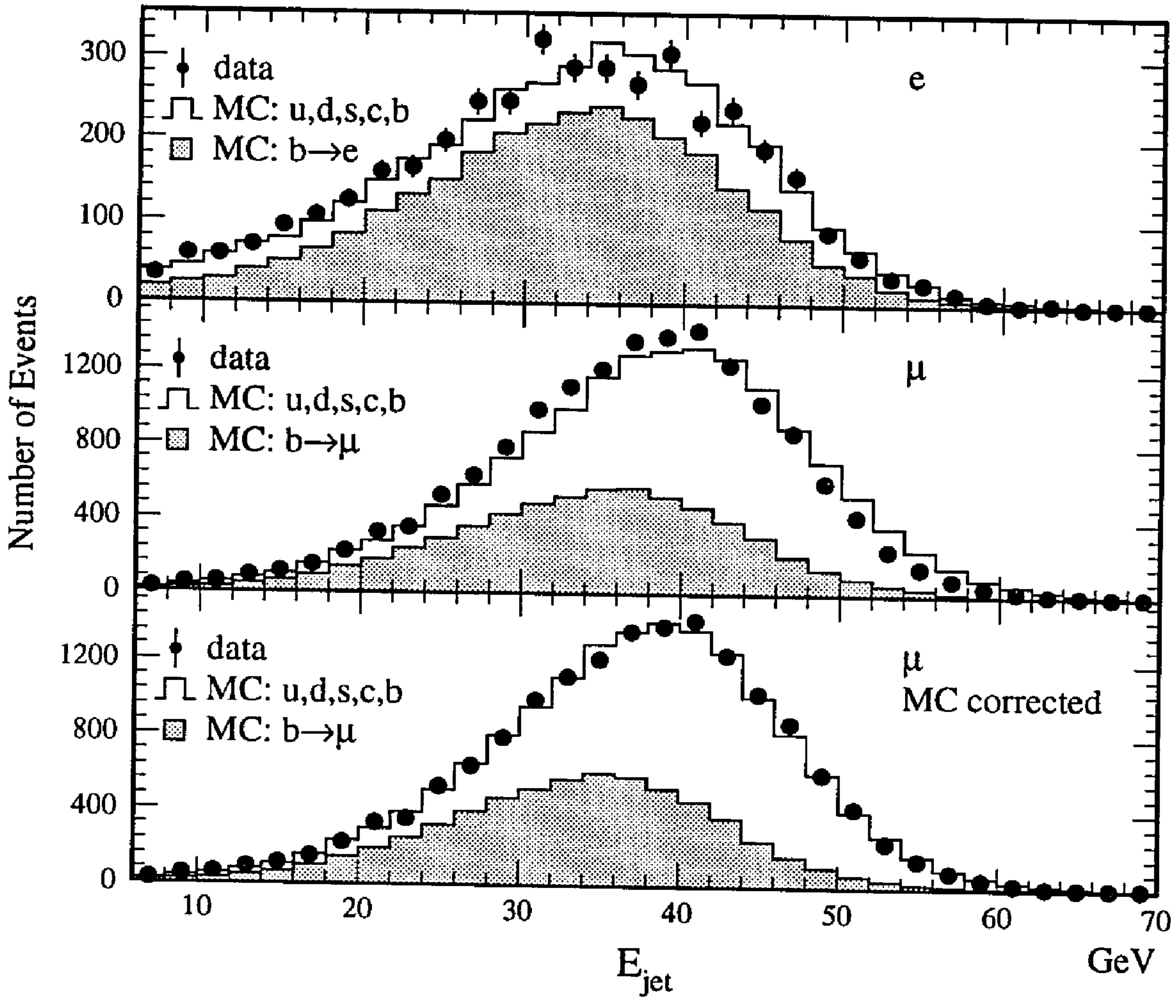

FIG. B.1: Energy of the jet closest to the selected lepton in hadronic events.

E_{jet} for the selected leptons in q$\bar{\mathrm{q}}$ events. A small discrepancy between data and Monte Carlo is visible in the muon plot. The Monte Carlo muon distribution has a larger width and is shifted with respect to the data. The origin of this discrepancy has not been clearly identified. There are known small problems with the simulation of muons in the hadron calorimeter which could account for the observed discrepancy. The agreement is much improved by rescaling the Monte Carlo muon distribution by 0.95 and shifting it by 1.0 GeV. The result of this correction is displayed in Fig. B.1 and is used in the analyses that follow.

Because of the missing neutrino energy, the energy of semileptonic b jets is on average lower than that of the background. The separation of the signal from the background in the E_{jet} distribution, however, is not nearly as good as in the p_T distribution. To illustrate this point Fig. B.2 shows the fraction of prompt b decays in the sample, determined from the Monte Carlo, as a function of E_{jet} and p_T. For high p_T values the fraction approaches 90%, with most of the background concentrated in a small region of the distribution. The most significant contribution from E_{jet} occurs in the muon sample, where there is a large amount of non-heavy quark background. Using E_{jet} to augment the information extracted from p_T enhances the separation of prompt b decays from background. The next two sections describe how this can be exploited in the likelihood fits for the asymmetry and mixing.

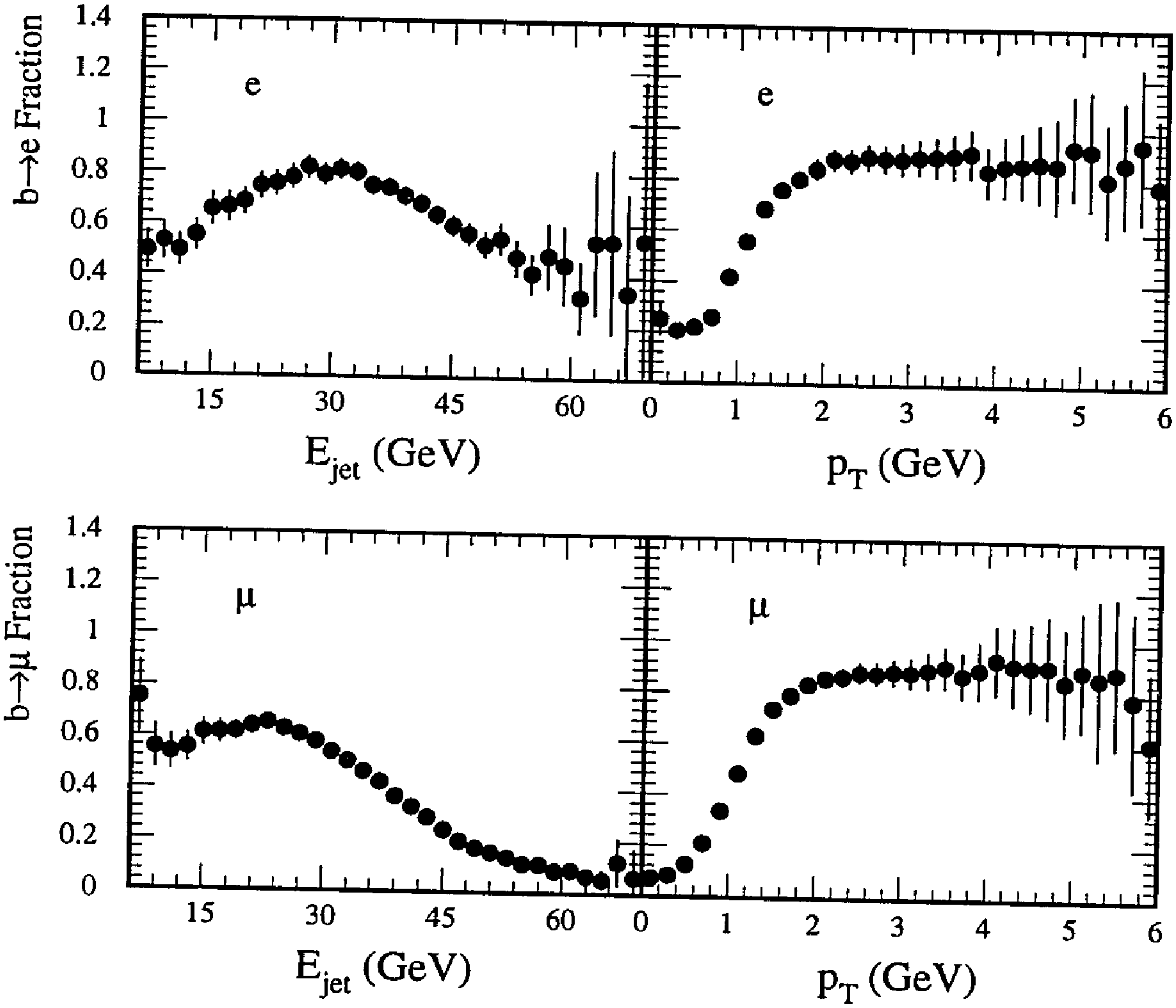

FIG. B.2: Monte Carlo prediction of the fraction of semileptonic b decays in the selected lepton sample.

B.2 The Asymmetry Measurement

The likelihood method described in Section 5.2.5 used the p_T distribution of the selected lepton to calculate the event probabilities P_k for the likelihood function defined by Eqs. (5.5) and (5.6). To include the jet energy information, $E_{\rm jet}$ can be added as a second dimension to the binning space: $P_k \rightarrow P_k(p_T, E_{\rm jet})$, where $E_{\rm jet}$ was restricted to the region 6-66 GeV. The number of divisions in p_T and $E_{\rm jet}$ are labeled N_{pT} and N_{Ejet}, respectively. The total number of bins is simply $N_{\rm bins} = N_{pT} N_{Ejet}$. The general problem of selecting the optimal number of bins arises, and again the sensitivity function defined by Eq. (5.7) was used as a guide to the appropriate choice.

Since the total number of bins grows geometrically, a lower value for N_{pT} was chosen compared to what was used in the p_T-only fit of Section 5.2.5. The number of p_T divisions was fixed at ten, which maintains a high average bin population in the fit without sacrificing much sensitivity to p_T. With this choice of N_{pT} the sensitivity as a function of N_{Ejet} is plotted in Fig. B.3. As expected, the sensitivity increases with the number of bins and the improvement is much more pronounced in the muon sample. To check that the increased sensitivity was not the result of a quirk in the binning scheme, $E_{\rm jet}$ was replaced with $E_{\rm rndm}$, a random variable that has the same overall shape. The total $E_{\rm jet}$ distribution can be crudely approximated by a Gaussian of width 9.6 GeV and mean 36.4 GeV. A random number, $E_{\rm rndm}$, generated from this Gaussian distribution was assigned to each data and Monte Carlo event. The sensitivity function using $E_{\rm rndm}$ in place of $E_{\rm jet}$ is also displayed in Fig. B.3. No improvement in sensitivity is observed for $E_{\rm rndm}$ since it carries no information about

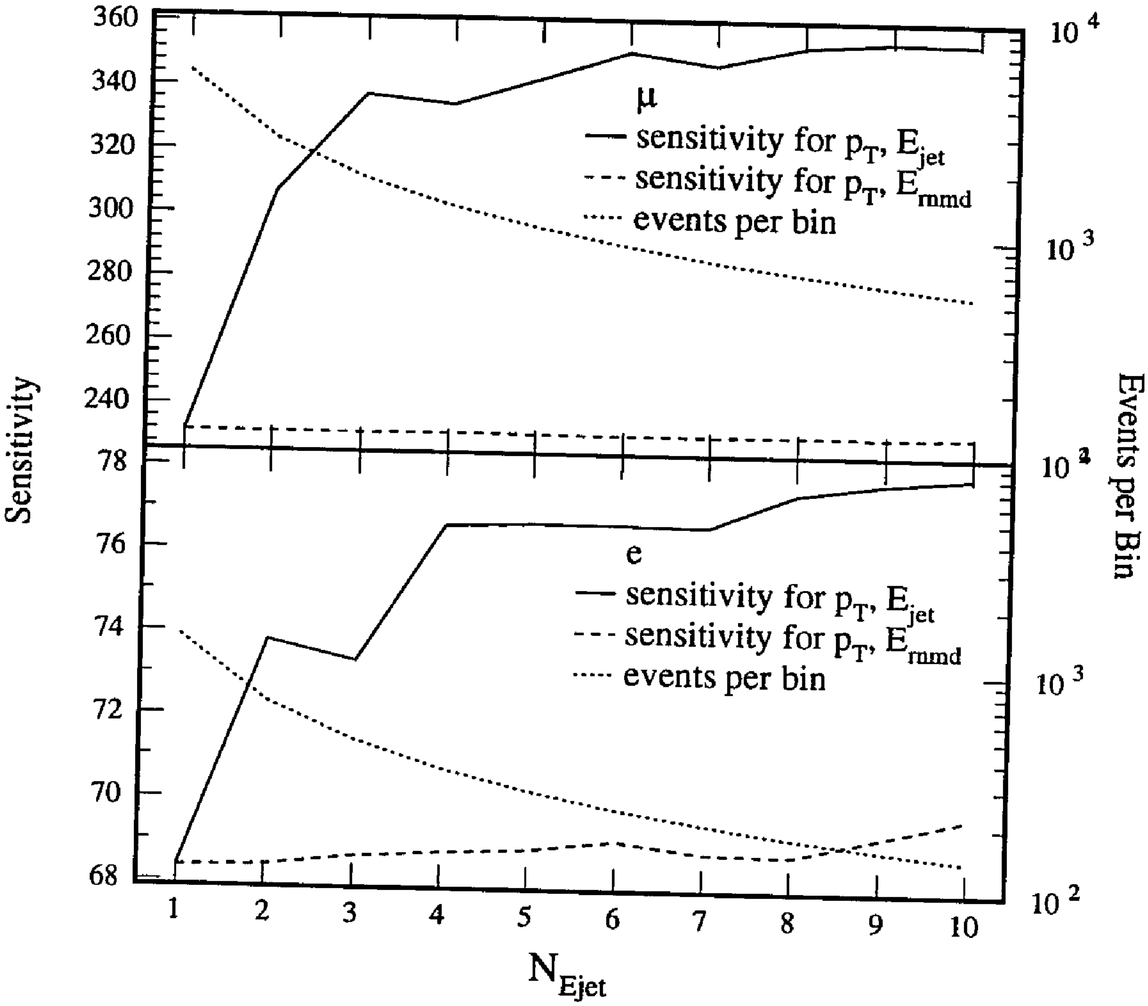

FIG. B.3: Sensitivity to prompt b decays binned in p_T and $E_{\rm jet}$, with $N_{pT} = 10$.

the desired signal.

A plateau in the sensitivity plots of Fig. B.3 occurs at N_{Ejet}= 6, and for this value the results of the likelihood fit for $A^{\rm obs}_{b\bar{b}}$ are given in Table B.1. Also listed in the table is the result using $N_{pT} = 60$ and $N_{Ejet} = 1$ and the result using $E_{\rm rndm}$ in favor of $E_{\rm jet}$. The former, which will be compared to the result of the $E_{\rm jet}$ fit, is identically equal to the p_T-only fit in Section 5.2.5 with $N_{\rm bins} = N_{pT} = 60$. Since this fit has the same total number of bins as the $E_{\rm jet}$ fit, any dependence of the error on the bin population should be minimized in the comparison of the results.

Table B.1: Asymmetry determined from likelihood fit with different binning choices.

lepton	$A^{\rm obs}_{b\bar{b}}$		
	$N_{pT} = 10$, $N_{Ejet} = 6$	$N_{pT} = 60$, $N_{Ejet} = 1$	$N_{pT} = 10$, $N_{Erndm} = 6$
μ	0.05357 ± 0.01831	0.05217 ± 0.01865	0.05291 ± 0.01905
e	0.06804 ± 0.02540	0.06557 ± 0.02550	0.07354 ± 0.02566
Total	0.05930 ± 0.01481	0.05761 ± 0.01501	0.06109 ± 0.01525

It was observed in the data and from Monte Carlo studies that if the asymmetry is small (less than 0.2), then the statistical error is approximately independent of the value of the asymmetry. This can also be seen directly from the asymmetry error in the counting method:

$$dA = \sqrt{(1 - A^2)/N}.$$

Therefore, the errors from the different binning schemes listed in Table B.1 can be compared directly. By including $E_{\rm jet}$ information in the fit, the errors are reduced by a small amount. The total improvement is less than 2%, most of which comes from the muon sample. The errors are correspondingly increased by using $E_{\rm rndm}$, but again the change is small, less than 2%. These results were independently confirmed by using a subset of the Monte Carlo as input data. The same change in the errors in the fits using $E_{\rm jet}$ and $E_{\rm rndm}$ were observed.

B.3 The Mixing Measurement

In the likelihood method of Section 5.3.3, which was used to measure the B^0-$\bar{B}^0$ mixing parameter, the event probabilities, P_k, were determined in a way analogous to the asymmetry fit. Since there are two leptons per event in the mixing sample, the joint probability is two dimensional: $P_k = P_k(p_{T1}, p_{T2})$, where p_{T1} and p_{T2} are the transverse momenta of the two leptons.

The straight forward approach to include $E_{\rm jet}$ information into the fit would be to increase the binning space to four dimensions: $P_k \rightarrow P_k(p_{T1}, p_{T2}, E_{{\rm jet}_1}, E_{{\rm jet}_2})$. This proves to be intractable since the bin populations in p_T are already small (see Fig. 5.22). Adding extra dimensions to the binning space would result in severely reduced statistics. To reduce the dimensionality of the problem, p_T and $E_{\rm jet}$ can be combined in the ratio $p_T/E_{\rm jet}$. This represents a mapping of the two dimensional space $p_T \times E_{\rm jet}$ to the one dimension space $p_T/E_{\rm jet}$, where all leptons that fall on a line $p_T = mE_{\rm jet}$ are mapped to the point m in the new space. The distribution of this one dimensional variable is displayed in Fig. B.4. The overall shape of the distribution is similar to the p_T plot in Fig. 5.20 the major difference being that the background is slightly shifted to lower values of $p_T/E_{\rm jet}$.

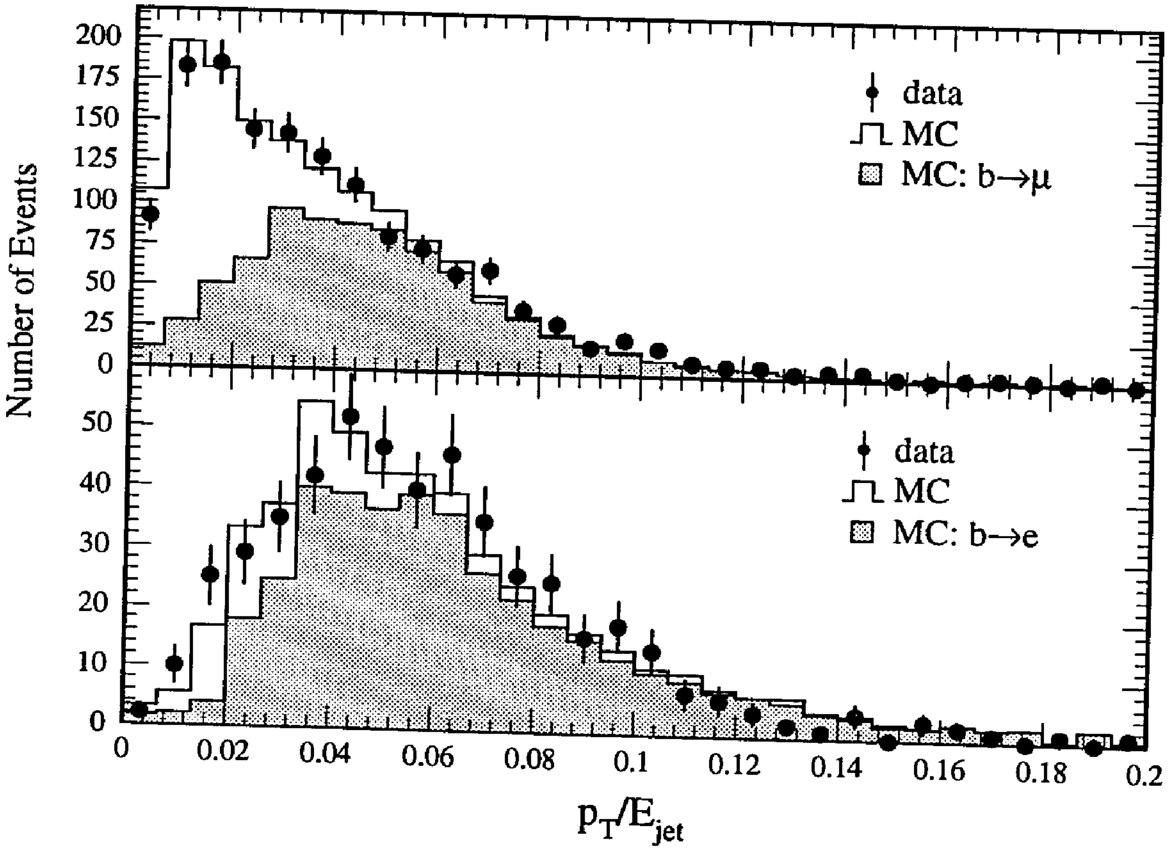

FIG. B.4: Comparison of 1991 data and Monte Carlo p_T/E_{jet} distributions for leptons from selected dilepton events.

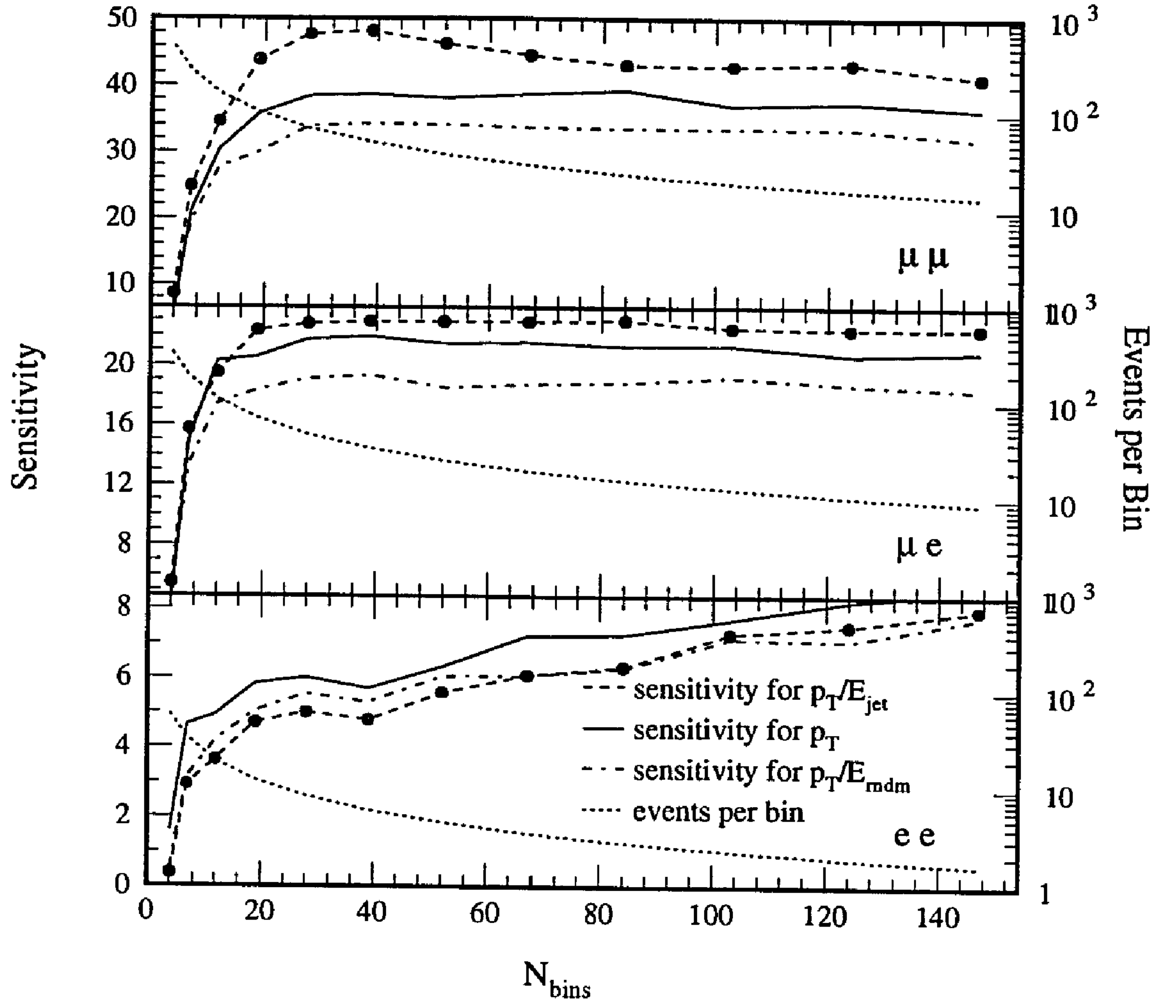

FIG. B.5: Comparison of the sensitivity function for the p_T/E_{jet}, p_T, and p_T/E_{rndm} binning schemes. The markers indicate the computed values of S at $j = 1, 2, 3, \ldots$, where $N_{\text{bins}} = j^2 + 3$.

Incorporating E_{jet} into the likelihood fit, the joint probability for the two leptons in the event is $P_k \rightarrow P_k(p_{T1}/E_{\text{jet}_1}, p_{T2}/E_{\text{jet}_2})$. Choosing a binning scheme analogous to what was used for the p_T-only case (see Section 5.3.3) leads to the selection of the cut-offs at 0.100 ± 0.008 for muons and 0.124 ± 0.016 for electrons. The sensitivity function and bin population for this binning scheme are shown in Fig. B.5. This figure also includes the sensitivity function from the fit using p_T only and the fit using p_T/E_{rndm}. The p_T/E_{rndm} distribution was generated using a random number

E_{rndm} that was calculated as in the previous section.

In the samples with muons the sensitivity is greater for p_T/E_{jet} than for p_T. In all of the samples p_T/E_{rndm} exhibited less sensitivity than p_T. Since E_{rndm} contains no information about the decay, combing it with p_T tends to dilute the sensitivity.

The maximum sensitivity in each lepton pair sample is reached when $j = 5$. The results of the likelihood fit using p_T/E_{jet}, p_T, and p_T/E_{rndm} with j= 5 divisions are listed in Table B.2. The different fits cannot be directly compared since the errors depend on the measured value of the mixing parameter. The relationship between the error and the measured value of $\mathcal{X}$ is approximately linear for values of $\mathcal{X}$ in the region 0.05-0.20 and depends on the lepton pair type. The relationship was determined empirically by using a subset of the Monte Carlo as the input data and randomly changing the sign of some of the leptons in the input. The cumulative result of many iterations of the above procedure is plotted in Fig. B.6. The general form of Fig. B.6 is reproduced by the counting method in the simplified case in which none of the backgrounds contribute to the mixing. The error in $\mathcal{X}$ is

Table B.2: Comparison of mixing results.

lepton pair	$\mathcal{X}$ fit binned in:		
	p_T/E_{jet}	p_T	p_T/E_{rndm}
$\mu\,\mu$	0.11519 ± 0.03787	0.07261 ± 0.03348	0.06132 ± 0.03374
μ e	0.13634 ± 0.03661	0.14244 ± 0.03770	0.14763 ± 0.04008
e e	0.18938 ± 0.07286	0.15897 ± 0.06833	0.14058 ± 0.06406
Total	0.13676 ± 0.02479	0.11821 ± 0.02386	0.11342 ± 0.02423

$$d\mathcal{X} = \frac{1}{4F\sqrt{N}}\frac{\sqrt{R(1-R)}}{(1-2\mathcal{X})},$$

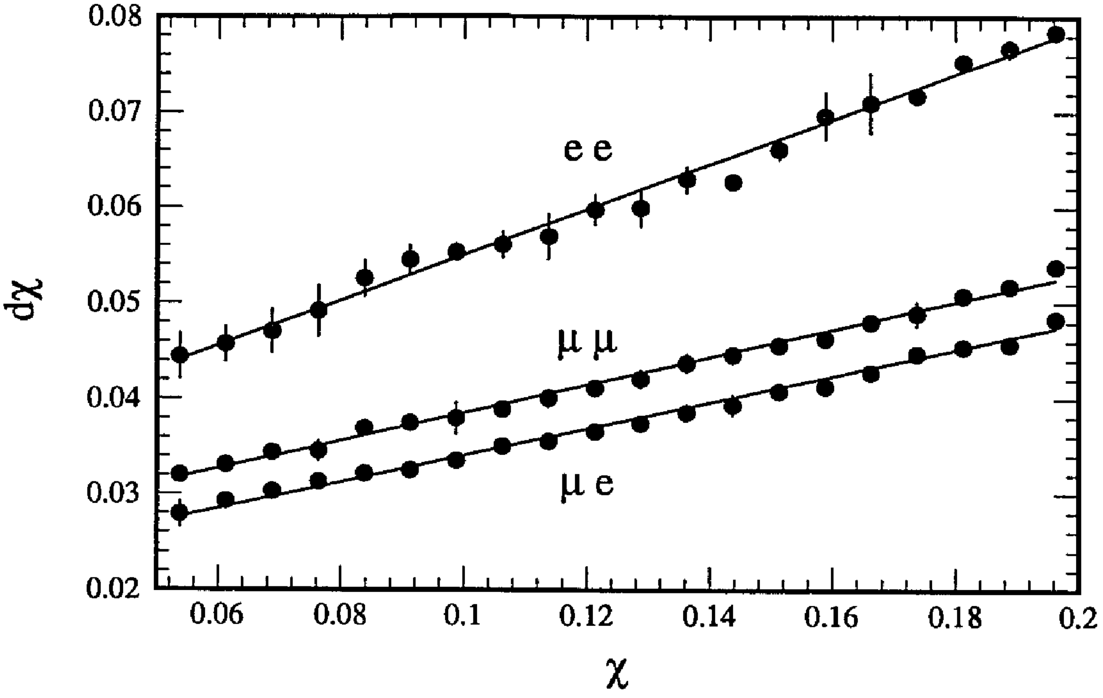

FIG. B.6: Dependence of the statistical error on the measured value of χ, determined from the Monte Carlo for each of the three dilepton samples.

where $R = 2F\chi(1 - \chi)$, N is the total number of events, and F is the fraction of events that exhibit mixing with mixing parameter χ. A plot of this function shows a linear relationship between χ and $d\chi$ similar to the plots in Fig. B.6.

Using the slopes of the fitted lines in Fig. B.6 the statistical errors in the p_T-only fit were rescaled to the value of χ measured in the $p_T/E_{\rm jet}$ and $p_T/E_{\rm rndm}$ fits and are compared to the results in the $p_T/E_{\rm jet}$ and $p_T/E_{\rm rndm}$ fits in Table B.3. The fractional

Table B.3: Percentage change in the scaled error on p_T compared to the error from either $p_T/E_{\rm jet}$ or $p_T/E_{\rm rndm}$, as observed in the data and Monte Carlo.

lepton pair	$p_T/E_{\rm jet}$		$p_T/E_{\rm rndm}$	
	data	MC	data	MC
$\mu\,\mu$	-4.6	-4.5	6.0	9.4
μ e	-0.7	-0.7	4.3	1.9
e e	-3.6	1.9	0.2	-5.4

change in the error is listed in the table as a percentage. Results using 1991 data and a subset of the Monte Carlo as input to the fit are included. The expected and observed behavior of the lepton pairs that contain muons agree quite well. A nearly 5% improvement in the $\mu\,\mu$ sample and a small improvement in the $\mu\,\mathrm{e}$ sample were achieved in the p_T/E_{jet} fit. No improvement was expected in the e e sample, and due to the low statistics for this category, fluctuations of the error obscured any clear effect. On the other hand, the fits that used E_{rndm} showed an increase in the errors. Overall, the expected improvement in the combined fit by binning in p_T/E_{jet} was less than 3%.

Appendix C

Higgs Mass

The current LEP results predict that the top mass is likely to be within reach of the Tevatron collider at Fermilab. A combined analysis of data from all four LEP experiments using the Standard Model [94] resulted in a top mass prediction of

$$m_t = 157^{+22}_{-25} \text{ GeV}.$$

The error does not include the effect of varying the Higgs mass, which was taken to be 300 GeV. The effective weak mixing angle for the top mass given above is

$$\sin^2\bar{\theta}_W = 0.2327 \pm 0.0008.$$

These results represent roughly half a million Z events per LEP experiment.

The Tevatron collider is in the process of upgrading its main injector accelerator complex. When completed it will increase the luminosity of the collider by a factor

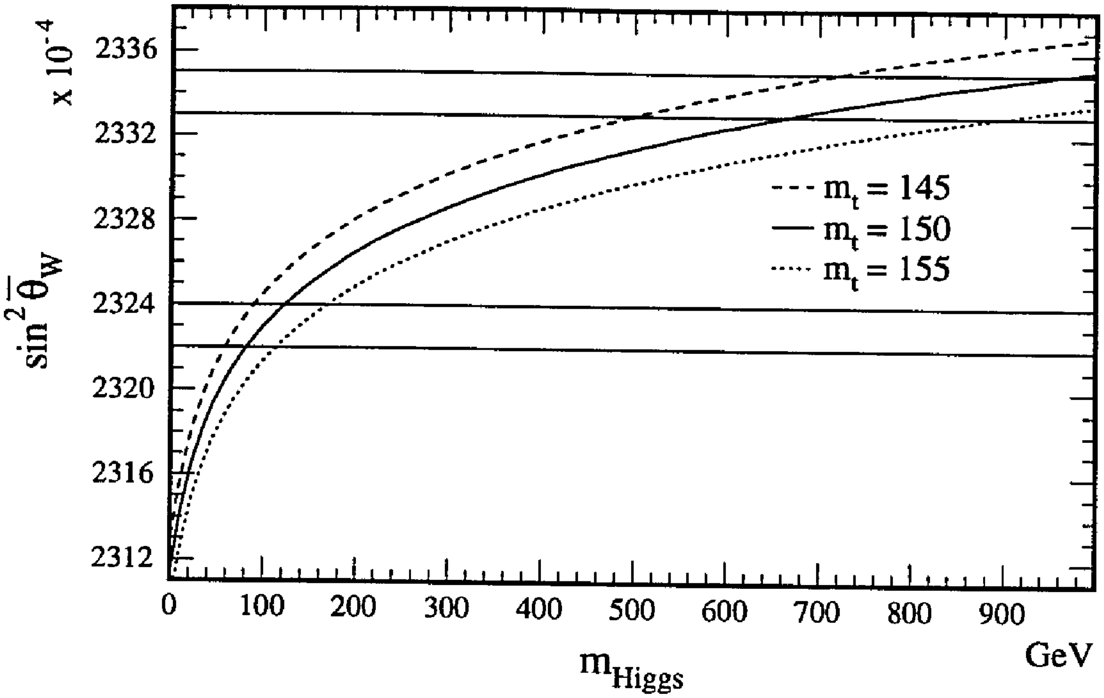

FIG. C.1: Effective weak mixing angle as a function of the Higgs mass for a fixed value of the top quark mass in the Standard Model.

of five. With this upgrade and one full year of running, it is estimated that the two collider detectors, CDF and D0, would be able to detect a top quark with a mass as high as 150 GeV and measure its mass with a precision of ± 5 GeV [95].

Making the optimistic assumption that the top quark will be observed at Fermilab raises the question of how well the Higgs mass could be predicted from LEP data. Figure C.1 shows the Standard Model relationship between $\sin^2\bar{\theta}_W$ and the Higgs mass for fixed values of the top mass. In the plot, m_Z and α_s were fixed to the L3 measured values (given in Chapter 6). The one standard deviation limit from the current LEP measurement of $\sin^2\bar{\theta}_W$ covers the range m_H= 50-1000 GeV. Significantly higher statistics are therefore required in order to place a meaningful bound on the Higgs mass. Already the lower bound, $m_H > 60$ GeV, has been made from direct searches for the Higgs at LEP [96]. Also note that $\sin^2\bar{\theta}_W$ is very sensitive to a low mass Higgs ($m_H < 200$ GeV) but not to a high mass Higgs.

At the level of 30 million Z events per LEP experiment, which is only an order of magnitude more data than what is being handled now, the error on $\sin^2\bar{\theta}_W$ could be brought down to $\simeq 0.0001$. This presupposes that systematic errors could be satisfactorily controlled. Contemplating errors smaller than 0.0001 would be presumptuous at this point since current theoretical uncertainties in the Standard Model calculations of $\sin^2\bar{\theta}_W$ are already of this size. The one standard deviation region covered by such an error for two different Higgs mass scenarios, light ($m_H = 100$ GeV) and heavy ($m_H = 800$ GeV), is given in Fig. C.1. In the light Higgs scenario the one standard deviation bound on the mass from $\sin^2\bar{\theta}_W$ is approximately ± 60 GeV, while it is more than ± 300 GeV in the heavy Higgs scenario. If the Higgs is relatively light than radiative corrections from LEP data could give an early indication of its mass; however, not much can be learned for a heavy Higgs.

While, it may not be possible to make a precise prediction of the Higgs mass from LEP data, it may be possible to distinguish between a heavy Higgs from a light one. This has important consequences for the direct search for the Higgs. It is difficult to observe Higgs decays at the SSC and LHC if the Higgs mass is less than twice the mass of the Z. If the LEP data could indicate which side of this boundary the Higgs mass falls, then it would provide a useful guide to the SSC and LHC experiments as to where to invest the most effort in the Higgs search.

References

[1] S.L. Glashow, Nucl. Phys. **22** (1961) 579.

[2] S.L. Glashow, Phys. Rev. **D2** (1970) 1285.

[3] S. Weinberg, Phys. Rev. Lett. **19** (1967) 1264.

[4] A. Salam, Phys. Rev. **127** (1962) 331.

[5] Gargamelle Collab., F.J. Hasert *et al.* , Phys. Lett. **46 B** (1973) 121.

[6] UA1 Collab., G. Arnison *et al.* , Phys. Lett. **126 B** (1983) 398.

[7] UA2 Collab., P. Bagnaia *et al.* , Phys. Lett. **129 B** (1983) 130.

[8] SLAC Linear Collider Conceptual Design Report, SLAC-PUB-229 (1980).

[9] C. Camilleri *et al.* , Preprint CERN/76-18, CERN, 1976.

[10] Herb, S. W., *et al.* , Phys. Rev. Lett. **39** (1977) 252.

[11] Ines, W. R. *et al.* , Phys. Rev. Lett. **39** (1977) 1240.

[12] Ueno, K., *et al.* , Phys. Rev. Lett. **42** (1979) 486.

[13] Andrews, D., *et al.* , (CLEO), Phys. Rev. Lett. **45** (1980) 219.

[14] Finocchiaro, G., *et al.* , (CUSB), Phys. Rev. Lett. **45** (1980) 222.

[15] Thorndike, E. H.,, (CLEO), review p241 **16** (1999) 0.

[16] MARK II Collab., M. E. Nelson, *et al.* , Phys. Rev. Lett. **50** (1983) 1542.

[17] MAC Collab., E. Fernandez, *et al.* , Phys. Rev. Lett. **50** (1983) 2054.

[18] DELCO Collab., D. E. Koop, *et al.* , Phys. Rev. Lett. **52** (1984) 970.

[19] TPC Collab., H. Aihara, *et al.* , LBL Rep. 17545 (1984).

[20] MARK-J Collab., B. Adeva, *et al.* , Phys. Rev. Lett. **51** (1983) 443.

[21] TASSO Collab., M. Althoff, *et al.* , Phys. Lett. **146B** (1984) 443.

[22] CELLO Collab., H. J. Behrend, *et al.* , Z. Phys. **C 19** (1983) 291.

[23] L. Rolandi, CERN-PPE/92-175 (1992), talk given at the XXVI ICHEP, Dallas (1992).

[24] E. Fortson, L. Lewis, Phys. Rep. **113** (1984) 289.

[25] C. Y. Prescott, *et al.* , Phys. Lett. **77B** (1978) 347.

[26] A. Argento, *et al.* , Phys. Lett. **140B** (1984) 142.

[27] M. Gell-Mann, Acta Phys. Austriaca , Suppl. **IX** (1972) 733;
H. Fritzsch and M. Gell-Mann, 16th International Conference on High Energy Physics, Batavia, 1972; editors J.D. Jackson and A. Roberts, National Accelerator Laboratory (1972);
H. Fritzsch, M. Gell-Mann and H. Leytwyler, Phys. Lett. **B 47** (1973) 365;
D.J. Gross and F. Wilczek, Phys. Rev. Lett. **30** (1973) 1343;
D.J. Gross and F. Wilczek, Phys. Rev. **D 8** (1973) 3633;
H.D. Politzer, Phys. Rev. Lett. **30** (1973) 1346;
G. 't Hooft, Nucl. Phys. **B 33** (1971) 173.

[28] E. R. Cohen, *et al.* , Rev. Mod. Phys. **59** (1987) 1121.

[29] G. Barden, *et al.* , Phys. Lett. **137 B** (1984) 135.

[30] L3 Collab., O. Adriani *et al.* , Preprint CERN-PPE/93-31, CERN, 1993, submitted to Physics Reports.

[31] G. Degrassi, S. Fanchiotti and A. Sirlin, Nucl. Phys. **B351** (1991) 49.

[32] W. Hollik, Fortschr. Phys. **38** (1990) 65.

[33] D. Kennedy and B.W. Lynn, Nucl. Phys. **B232** (1989) 1.

[34] A. Sirlin, Phys. Rev. **D22** (1980) 971.

[35] Particle Data Group, Phys. Rev. **45 D** (1992) II.1.

[36] X. Artru and G. Mennesier, Nucl. Phys. **B126** (1974) 93.

[37] X. Artru, Phys. Rep. **97** (1983) 147.

[38] R. Odorica, Nucl. Phys. **B172** (1980) 157.

[39] G.C. Fox and S. Wolfram, Nucl. Phys. **B168** (1980) 285.

[40] R.D. Field and S. Wolfram, Nucl. Phys. **B213** (1983) 65.

[41] T.D. Gottschalk, Nucl. Phys. **B214** (1983) 201.

[42] B. Anderson, *et al.* , Phys. Rep. **97** (1983) 33.

[43] B. Anderson, *et al.* , Z. Phys. **C1** (1979) 105.

[44] T. Sjöstrand, Comp. Phys. Comm. **39** (1986) 347;
T. Sjöstrand and M. Bengtsson, Comp. Phys. Comm. **43** (1987) 367.

[45] B. Anderson, G Gustafson, and B. Söderberg, Z. Phys. **C20** (1983) 317.

[46] Ya. I. Azimov *et al.* , Preprint LNPI-222, Leningrad, 1976.

[47] M. Suzuki, Phys. Lett. **71B** (1977) 139.

[48] J.D. Bjorken, Phys. Rev. **D17** (1978) 171.

[49] C. Peterson *et al.* , Phys. Rev. **D 27** (1983) 105.

[50] J. Chrin, Z. Phys. **C 36** (1987) 163.

[51] S. Bethke, Z. Phys. **C 29** (1985) 175.

[52] L3 Collab., B. Adeva *et al.* , Phys. Lett. **B 261** (1991) 177.

[53] Particle Data Group, Phys. Lett. **B 239** (1990) VII.113.

[54] UA1 Collab., C. Albajar *et al.* , Phys. Lett. **B 186** (1987) 247, erratum *ibid.* **B 197** (1987) 565.

[55] UA1 Collab., C. Albajar *et al.* , Phys. Lett. **B 262** (1991) 171.

[56] ARGUS Collab., H. Albrecht *et al.* , Phys. Lett. **B 192** (1987) 245.

[57] ARGUS Collab., H. Albrecht *et al.* , Z. Phys. **C 55** (1992) 357.

[58] CLEO Collab., M. Artuso *et al.* , Phys. Rev. Lett. **62** (1989) 2233.

[59] CDF Collab., F. Abe *et al.* , Phys. Rev. Lett. **67** (1991) 3351.

[60] LEP DESIGN REPORT, Vol. II The LEP Main Ring, CERN Report CERN-LEP/84-01 (1984) 1.

[61] LEP DESIGN REPORT, Vol. I The LEP Injector Chain, CERN Report CERN-LEP/TH/83-29 (1983) 1.

[62] L3 Collab., B. Adeva *et al.* , Nucl. Inst. Meth. **A 289** (1990) 35.

[63] Colliers Encycl. Vol 8 (1987) 677.

[64] G. Marchesini and B. Webber, Nucl. Phys. **B 310** (1988) 461;
G. Marchesini *et al.* , Comp. Phys. Comm. **67** (1992) 465.

[65] S. Jadach, B.F.L. Ward and Z. Was, Comp. Phys. Comm. **66** (1991) 276.

[66] M. Böhm, A. Denner and W. Hollik, Nucl. Phys. **B 304** (1988) 687.

[67] F.A. Berends, R. Kleiss and W. Hollik, Nucl. Phys. **B 304** (1988) 712.

[68] S. Jadach and B.F.L. Ward, Phys. Rev. **D 40** (1989) 3582.

[69] S. Jadach *et al.* , Phys. Lett. **B 268** (1991) 253;
S. Jadach *et al.* , Comp. Phys. Comm. **70** (1992) 305.

[70] The L3 detector simulation is based on GEANT Version 3.14.
See R. Brun *et al.* , "GEANT 3", CERN DD/EE/84-1 (Revised), September 1987.
The GHEISHA program (H. Fesefeldt, RWTH Aachen Report PITHA 85/02 (1985)) is used to simulate hadronic interactions.

[71] L3 Collab., B. Adeva *et al.* , Z. Phys. **C 51** (1991) 179.

[72] L3 Collab., B. Adeva *et al.* , Phys. Lett. **B 252** (1990) 703.

[73] Particle Data Group, Phys. Lett. **B 239** (1990) III.35.

[74] W.R. Nelson, H. Hirayama, and D.W.O. Rogers, "The EGS4 Code System," SLAC-265 (1985).

[75] G. Rahal-Callot, Vertex Chamber Resolutions, Internal Report 1015, L3, 1991.

[76] L3 Collab., O. Adriani *et al.* , Phys. Lett. **B 292** (1992) 454.

[77] Particle Data Group, Phys. Lett. **B 239** (1990) VII.113, We have averaged the PETRA and PEP measurements according to the procedure used by the Particle Data Group.

[78] D. Bardin et al., FORTRAN package ZFITTER, and preprint CERN–TH. 6443/92;
D. Bardin et al., Z. Phys. **C 44** (1989) 493;
D. Bardin et al., Nucl. Phys. **B 351** (1991) 1;
D. Bardin et al., Phys. Lett. **B 255** (1991) 290.

[79] G. Burgers, CERN Report CERN 88-06 (1988) 121.

[80] F.A. Berends *et al.* , CERN Report CERN 89-08, Vol. 1 (1989) 89.

[81] CDF Collab., F. Abe *et al.* , Phys. Rev. **D 43** (1991) 664.

[82] CELLO Collab., H. J. Behrend, *et al.* , Preprint DESY 89-125, DESY, 1989.

[83] JADE Collab., W. Bartel, *et al.* , Phys. Lett. **146B** (1984) 437.

[84] JADE Collab., E. Elsen, *et al.* , Preprint DESY 89-127, DESY, 1989.

[85] MARK-J Collab., B. Adeva, *et al.* , Phys. Rep. **109** (1984) 133.

[86] TASSO Collab., M. Althoff, *et al.* , Z. Phys. **C22** (1984) 219.

[87] TASSO Collab., E. Bernardi, *et al.* , Preprint DESY 89-125, DESY, 1989.

[88] TPC Collab., H. Aihara, *et al.* , Phys. Rev. **D31** (1985) 2719.

[89] TPC Collab., H. Aihara, *et al.* , Z. Phys. **C27** (1985) 39.

[90] MAC Collab., H.R. Band, *et al.* , Phys. Lett. **218B** (1989) 369.

[91] HRS Collab., C.R. Ng, *et al.* , Preprint ANL-HEP-PR-88-11, ANL, 1988.

[92] AMY Collab., H. Sagawa, *et al.* , Phys. Rev. Lett. **63** (1989) 2341.

[93] AMY Collab., H. Sagawa, *et al.* , Preprint KEK-90-61, KEK, 1990.

[94] S.C.C. Ting, CERN-PPE/93-34 (1993), talk given at the annual meeting of the DPF or the APS, Chicago (1992).

[95] H.E. Montgomery, "Some Results from Fermilab," lecture given at International School of Subnuclear Physics, 31st Course, Erice Sicily, 4-12 July (1993).

[96] T. Mori, talk given at the XXVI ICHEP, Dallas (1992).